

INFORMATION TO USERS

This manuscript has been reproduced from the microfilm master. UMI films the text directly from the original or copy submitted. Thus, some thesis and dissertation copies are in typewriter face, while others may be from any type of computer printer.

The quality of this reproduction is dependent upon the quality of the copy submitted. Broken or indistinct print, colored or poor quality illustrations and photographs, print bleedthrough, substandard margins, and improper alignment can adversely affect reproduction.

In the unlikely event that the author did not send UMI a complete manuscript and there are missing pages, these will be noted. Also, if unauthorized copyright material had to be removed, a note will indicate the deletion.

Oversize materials (e.g., maps, drawings, charts) are reproduced by sectioning the original, beginning at the upper left-hand corner and continuing from left to right in equal sections with small overlaps. Each original is also photographed in one exposure and is included in reduced form at the back of the book.

Photographs included in the original manuscript have been reproduced xerographically in this copy. Higher quality 6" x 9" black and white photographic prints are available for any photographs or illustrations appearing in this copy for an additional charge. Contact UMI directly to order.

UMI[®]

Bell & Howell Information and Learning
300 North Zeeb Road, Ann Arbor, MI 48106-1346 USA
800-521-0600

**REACTIVE PLASMA SPRAY FORMING
OF Al-TiAl₃ COMPOSITES
USING A TRIPLE PLASMA SYSTEM**

by

Majid Entezarian

Department of Mining and Metallurgical Engineering
McGill University, Montreal

June 1997

A Thesis submitted to the
Faculty of Graduate Studies and Research
in partial fulfilment of the
requirements of the degree of
Doctor of Philosophy

© Majid Entezarian, 1997



National Library
of Canada

Acquisitions and
Bibliographic Services

395 Wellington Street
Ottawa ON K1A 0N4
Canada

Bibliothèque nationale
du Canada

Acquisitions et
services bibliographiques

395, rue Wellington
Ottawa ON K1A 0N4
Canada

Your file *Votre référence*

Our file *Notre référence*

The author has granted a non-exclusive licence allowing the National Library of Canada to reproduce, loan, distribute or sell copies of this thesis in microform, paper or electronic formats.

The author retains ownership of the copyright in this thesis. Neither the thesis nor substantial extracts from it may be printed or otherwise reproduced without the author's permission.

L'auteur a accordé une licence non exclusive permettant à la Bibliothèque nationale du Canada de reproduire, prêter, distribuer ou vendre des copies de cette thèse sous la forme de microfiche/film, de reproduction sur papier ou sur format électronique.

L'auteur conserve la propriété du droit d'auteur qui protège cette thèse. Ni la thèse ni des extraits substantiels de celle-ci ne doivent être imprimés ou autrement reproduits sans son autorisation.

0-612-36975-7

To
Maryam
and
Parsa

ABSTRACT

Composite materials can be produced through a novel process known as reactive plasma spray forming. This technique was used to fabricate Al-TiAl₃ composites by injecting both Al and TiCl₄ vapor into a triple plasma system. The microstructures of the Al-TiAl₃ composites were compared with those of more conventional processing routes. The resulting microstructures were strongly dependant on processing method. The cast microstructure exhibited an acicular morphology of TiAl₃ in an Al matrix. Composites produced by powder metallurgy and vacuum plasma spray contained coarse equiaxed particles of the intermetallic phase whereas the microstructure of the reactive plasma sprayed material was very uniform and exhibited a very fine dispersion of TiAl₃ in the matrix.

It was demonstrated that the atomization process occurring prior to Al-TiCl₄ reaction has a strong effect on the product due to its control over the average particle size and consequently on the temperature of the plasma atomized particles. It was observed that coarse particles (<100 μm) react only on the surface. Particle temperatures higher than 1340°C produce a uniform microstructure while lower temperatures result in only surface reacted particles. The study showed that the alignment of the plasma torches, small wire diameters, proper power to Al feed rate ratio, and the use of an accelerating nozzle decrease the average particle size of the sprayed materials.

A non-uniform distribution of Ti was observed across the deposits produced through reactive plasma atomization and was attributed to non-uniform particle size, temperature, and velocity distributions across the atomization plume. Chlorine was detected in the product, and varied from 0.3 to 1.3 wt% depending on the experimental conditions. The chlorine was reduced to 0.1 wt% through vacuum sublimation after removal from the reaction chamber.

The reactively produced bulk materials were porous and required further consolidation through hot rolling. The hot rolled and annealed materials tested at room temperature retain 75% of their strength after annealing for 196 hours at 300°C. The TEM analysis revealed the presence of very fine (60 nm) intermetallic phases in the microstructure after annealing at 300°C. The stability of such fine precipitates suggests that Al-TiAl₃ composites would offer superior high temperature mechanical properties in comparison with conventional Al alloys.

ABSTRAIT

Les matériaux composites peuvent être produits grâce à un procédé connu sous le nom de "fabrication par projection réactive au plasma". Cette technique a été utilisée pour la fabrication de composites Al-TiAl₃ en injectant de l'aluminium et de la vapeur de TiCl₄ dans un système de triple torche au plasma. Les microstructures des composites Al-TiAl₃ ont été comparées à celles issues de procédés conventionnels. Les microstructures obtenues se sont avérées fortement dépendantes du procédé utilisé. La microstructure des matériaux coulés démontrait une morphologie aciculaire de TiAl₃ dans une matrice d'aluminium. Les composites produits par métallurgie des poudres et par projection par plasma contenaient de larges grains intermétalliques équiaux, alors que les composites issus de la projection réactive au plasma avaient une microstructure dans laquelle il y avait une dispersion très uniforme et fine de TiAl₃ dans la matrice.

Il a été démontré que l'étape d'atomisation qui a lieu avant la réaction Al-TiCl₄ avait une influence importante sur le produit final, grâce entre autre au contrôle qu'exerce cette étape sur la taille et la température des particules atomisées. Les grosses particules (> 100 μm) n'ont montré des signes de réaction qu'à la surface. Les particules avec une température plus élevée que 1340°C donnent des microstructures uniformes, alors que celles avec une température inférieure ne résultent qu'en des particules avec une réaction de surface. L'étude a révélée que l'alignement des torches, les fils de petits diamètres, un rapport adéquat de la puissance sur le débit massique d'aluminium, ainsi que l'utilisation d'une tuyère d'accélération, tendaient tous à diminuer la taille moyenne des matériaux atomisés.

Une distribution non-uniforme de Ti a été observée à travers les dépôts produits par déposition réactive par plasma. Celle-ci est reliée à la non-uniformité des tailles, de la température, et de la distribution de vitesse des particules à travers la zone d'atomisation. La présence de chlore a été détectée dans le produit, dans des proportions de 0.3 à 1.3 %pds dépendamment des conditions expérimentales. Le niveau de chlore a été réduit à 0.1 %pds grâce à l'utilisation d'une chambre de sublimation sous-vide après la déposition par plasma.

Les matériaux produits par déposition réactive était poreux et nécessitaient une étape de consolidation subséquente (déformation à chaud). Les matériaux déformés à chaud et ayant subi un recuit de 196 heures à 300°C ont conservé, lorsque testés à température ambiante, près de 75% de leur résistance à la traction initiale. Les analyses effectuées au MET ont révélé la présence de phases intermétalliques très fines (60 nm) dans la microstructure après recuit à 300°C. La stabilité de ces précipités tend à indiquer que les composites Al-TiAl₃ pourraient offrir, à haute température, des propriétés mécaniques supérieures lorsque comparés aux alliages d'aluminium conventionnels.

ACKNOWLEDGEMENTS

I would like to express my sincere gratitude and appreciation to Professor R.A.L.Drew for his inspiring supervision, and his continual interest and encouragement throughout the course of this work.

I also especially wish to thank Dr. P. Tsantrizos and my colleagues at PyroGenesis Inc. specifically Dr. K. Shanker and Dr. S. Grenier for all of their help and assistance through insightful discussions. I would like to thank Dr. S. Grenier also for French translation of the abstract.

I would also like to thank Dr. J.P. Immarigeon from NRC (IAR) for his instructive criticism, encouragement, and supervision.

I greatly appreciate the help, collaboration, and input of Dr. F. Allaire from Hydro-Quebec (LTEE) and T. Ledermann for experiments relating to plasma atomization, Xiaoxin Xia from Concordia University for TEM analysis, M. Riendeau for chemical analysis, and of Mr. Knoepfel for machine shop assistance.

I would like to thank my wife M. Mahmoudi for her endless encouragement, patience, and understanding throughout this work.

Finally, I am also indebted to PyroGenesis Inc. for their interest and partial financial support through IRAP and DND grant program, to Hydro-Quebec for their financial support, and to Iranian Ministry of Culture and Higher Education for their partial financial assistance.

Table of Contents

Chapter 1: Introduction	1
Chapter 2: Literature Review	5
2.1. INTRODUCTION	5
2.2. FUNDAMENTALS	5
2.2.1. GENERATION OF THERMAL PLASMA	7
2.2.2. CHARACTERIZATION OF THERMAL PLASMAS	8
2.2.2.1. Temperature Distribution in a Thermal Plasma	8
2.2.2.2. Velocity Distribution in Thermal Plasmas	9
2.3. THERMAL SPRAYING PROCESSING	10
2.3.1. Thermal Spray Processes	11
2.3.1.1. Combustion Flame Spraying	14
(a) Conventional Flame Spray	14
(b) High Velocity Oxy-Fuel Spraying (HVOF)	14
2.3.1.2. Arc Spraying	15
2.3.1.3. Plasma Spraying	15
(a) Vacuum Plasma Spray (VPS)	16
2.4. RECENT PROGRESS IN THERMAL SPRAY PROCESSES	16
2.5. PARTICLE-PLASMA INTERACTION AND PROCESS CONTROL	17
2.6. DEPOSITION DYNAMICS	18
2.7. MATERIALS SCIENCE OF THERMAL SPRAY DEPOSITS	19
2.8. OSPREY PROCESS	21

2.9. REACTIVE PLASMA SPRAYING22
2.10. AEROSPACE REQUIREMENTS26
2.10.1. Density26
2.10.2. Microstructure27
2.11. HIGH TEMPERATURE Al-ALLOYS27
2.11.1. Al-Zr-V Alloys28
2.11.2. Al-Fe-Si-V Alloys29
2.11.3. Thermal Stability in the Al-TiAl ₃ System29
2.11.4. Al-Ti System29
2.11.5 Mechanical Properties of Al-Ti alloys30
<i>Chapter 3: Objectives</i>	35
<i>Chapter 4: Experimental Procedures</i>	37
4.1. INTRODUCTION	37
4.2. PLASMA TORCH	38
4.3. TiCl ₄ INJECTION SYSTEM	39
4.4. REACTIVE PLASMA SPRAYING USING A SINGLE PLASMA SYSTEM ...	41
4.5. REACTIVE PLASMA SPRAYING USING A TRIPLE PLASMA SYSTEM ...	42
4.6. PRODUCTION OF AL-TiAl ₃ COMPOSITES THROUGH OTHER PROCESSES	43

4.7. PLASMA SPRAYING	43
4.7.1 Starting Materials	43
4.7.2. Experimental Design	43
4.8. CASTING	46
4.9. POWDER METALLURGY	46
4.10. THERMAL ANALYSIS	47
4.11. PLASMA ATOMIZATION	47
4.12. PARTICLE SIZE DISTRIBUTION	49
4.13. HOT ROLLING	50
4.14. CHEMICAL ANALYSES	50
4.15. ATOMIC ABSORPTION (AA)	50
4.16. MICROSTRUCTURAL SAMPLE PREPARATION	51
4.17. MICROSTRUCTURAL ANALYSIS	51
<i>Chapter 5: Plasma Atomization</i>	52
5.1. INTRODUCTION	52
5.2. LITERATURE REVIEW	54
5.2.1 Powder Production	54
5.2.1.1 Atomization	54

5.2.1.1.1 Gas Atomization	55
5.2.1.2 Droplet Formation Mechanisms	58
5.2.1.3 Kinetics of Droplet Solidification and Spherodization	61
5.2.2 Wire Atomization	64
5.2.3 Effect of Particle Size on Particle Velocity	65
5.2.4 The Effect of Wire Feeding Rate on Atomization Mechanism	66
5.3. RESULTS AND DISCUSSION	68
5.3.1 Metal Feeding	68
5.3.1.1 Feeding Molten Metal	69
5.3.2 Feeding Metal Wire	73
5.3.2.1 Low Ratio of Wire Feed Rate to Power	73
5.3.2.2 High Ratio of Wire Feed Rate to Power	75
5.3.2.3 Optimum Ratio of Wire Feed Rate to Power	75
5.3.3 Melting Rate	77
5.4. REDUCING THE AVERAGE POWDER SIZE	83
5.4.1 Effect of Wire Diameter on Average Particle Size	83
5.4.2 Torch Alignment	84
5.4.3 Torch Tip Distance from the Apex	84
5.4.4 Plasma Jet Accelerating Nozzle	85
5.5. DROPLET FORMATION DURING PLASMA ATOMIZATION	89
5.6. COMPARISON OF PLASMA ATOMIZATION (PA) WITH OTHER COMPETITIVE TECHNOLOGIES	92
5.6.1 Average Particle Size	92
5.6.2 Particle Size Distribution	93
5.6.3 Cooling Rate	93
5.7. CONCLUSIONS	95

Chapter 6: Al-TiAl₃ Composites	96
6.1. INTRODUCTION	96
6.2. PRODUCTION OF Al-TiAl ₃ COMPOSITES	97
6.2.1. Vacuum Plasma Spraying Using Elemental Powders	97
6.2.1.1. Spraying on Stainless Steel (SS)	98
6.2.1.2. Spraying on Ti Substrate	101
6.2.1.3. Qualitative Chemical Analysis of the Deposits	101
6.2.2. Casting of Al-TiAl ₃ Composites	107
6.2.3. Powder Metallurgy of Al-TiAl ₃ Composites	108
6.2.4. Reactive Hot Isostatic Pressing (RHIPping)	112
6.2.4.1. RHIPping Temperature	113
6.3. Reactive Plasma Spraying	118
6.3.1. Single Plasma Torch	123
6.3.1.1 Thermogravimetry Analysis	124
6.3.2. Triple Plasma System	128
6.3.2.1. Ti Distribution Across the Deposit	128
6.3.2.2. Microstructural Evolution	132
6.3.2.3. Velocity and Temperature Distributions	138
6.3.2.4. Porosity Distribution	139
6.4. PRODUCT DEVELOPMENT	141
6.4.1. Rolling	141
6.4.1.1. Surface Condition of Coupons	141
6.4.1.2. Effect of Reduction on Rolled Sheets	142
6.4.1.2. Effect of Rolling Temperature	142
6.4.1.3. Annealing	143
6.4.1.4. Effects of Rolling and Annealing on the Microstructure of the deposits	145

6.5. MECHANICAL PROPERTIES	151
6.5.1. Yield Strength	151
6.5.2. Tensile Strength	152
6.5.3. Elongation	153
6.5.4. Fractography	155
6.6. CHLORINE CONTENT	158
6.6.1. Chlorine Removal	160
<i>Chapter 7: Achievements and Conclusions</i>	162
7.1. TECHNICAL ACHIEVEMENTS	162
7.1.1 Reactive Plasma Atomization	162
7.1.2 Plasma Atomization	163
7.2. CONCLUSIONS	163
7.2.1 Reactive Plasma Atomization	163
7.2.2 Plasma Atomization	164
7.2.3 Casting, Powder Metallurgy, HIPping, and Plasma Spraying . . .	165
7.3. Contribution to Original Knowledge	167
<i>Chapter 8: References</i>	168
<i>Appendix 1:</i>	A1-1

List of Figures

Chapter 2: Literature Review

Figure 2.1 Simple schematic of a thermal plasma generating device.	7
Figure 2.2 Temperature distribution in a typical thermal plasma jet.	8
Figure 2.3 Velocity distribution in a typical thermal plasma jet.	9
Figure 2.4 Mean particle velocity as a function of particle size of WC-Co.	12
Figure 2.5 Temperature of WC-Co particles as a function of particle size in an argon plasma jet.	13
Figure 2.6 Schematic of the Osprey process.	21
Figure 2.7 The relative effects of various material properties on reducing structural weight in a Lockheed S-3A aircraft.	26
Figure 2.8 Al-rich section of Al-Ti phase diagram.	30
Figure 2.9 Specific stiffness for MA Al-Ti alloys compared to current and competitive elevated temperature alloys.	32
Figure 2.10 (a) Creep-rupture properties of MA Al alloys in the temperature range 315-535 °C (b) Variation in the ductility of MA Al alloys with temperature.	33

Chapter 4: Experimental Procedures

Figure 4.1 Schematic of the non-transfer D.C. plasma torch used for plasma atomization and reactive plasma spraying.	38
Figure 4.2 Schematic of the TiCl ₄ injection system.	39
Figure 4.3 Graphite nozzle used to inject TiCl ₄ into the plasma jet stream.	40
Figure 4.4 Schematic of reactive plasma spraying using a single plasma torch and Al powder as raw material.	41
Figure 4.5 Schematic of the reactive plasma spraying.	42
Figure 4.6 Scanning electron micrographs of the starting materials (a) Al powder, (b) Ti powder.	44
Figure 4.7 Plasma atomization reactor used for powder production study.	48

Figure 4.8 Schematic of the convergent/divergent nozzle used for plasma atomization. 49

Chapter 5: Plasma Atomization

Figure 5.1 Gas atomization designs (a) free fall and (b) confined.	56
Figure 5.2 Particle formation mechanism.	58
Figure 5.3. Average particle size as a function of the product of power and argon gas flow rate per gram of Al.	71
Figure 5.4. Average particle size of Al powder produced by plasma atomization as a function of kW/g, 2.38 mm Al wire dia. and no accelerating nozzle were used.	74
Figure 5.5. Various mechanisms of melting and atomization of wire in plasma atomization.	76
Figure 5.6. Temperature profiles during melting of a wire in triple plasma system.	78
Figure 5.7 Optimum feed rate as a function of heat diffusivity.	79
Figure 5.8. Melting rate of metal wires in triple plasma system (Wire dia. 1.5 mm, Plasma power = 100 kW).	81
Figure 5.9. Average particle size as a function of wire diameter.	83
Figure 5.10. Photograph of the wire feeding nozzle before correction of the torch misalignment.	85
Figure 5.11. Schematic of the optimum nozzle design for plasma atomization.	86
Figure 5.12. SEM of (a) IN 718 and (b) Ti-6-4 powders (+45-75 μm) produced by plasma atomization process.	87
Figure 5.13. The effects of nozzle and torch alignment on particle size distribution in plasma atomization process.	88
Figure 5.14. Droplet formation during plasma atomization; (a) necking, (b) spherodization in progress, and (c) end of droplet spherodization.	91
Figure 5.15. Comparison of average particle size distribution of atomization processes.	92
Figure 5.16 Secondary DAS and β grain size as a function of solidification rate.	94

Chapter 6: Al-TiAl₃ Composites

Figure 6. 1 (a) Backscatter image, and (b) EDS spectrum of the gray phase.	99
Figure 6. 2 EDS spectrum obtained from (a) needle like phase (b) reaction zone. . . .	100
Figure 6. 3. (a) BEI, and (b) the EDS spectrum of the interface of the Al-Ti powder sprayed on Ti substrate.	102
Figure 6. 4. Typical coating microstructure showing the unmelted Ti particles.	103
Figure 6. 5. DTA curves for (a) Al-5%Ti and (b) Al-10%Ti.	105
Figure 6. 6. DTA curve for Al-15%Ti	106
Figure 6. 7. Typical microstructure (5 wt.%Ti) obtained from casting in water-cooled copper mould.	107
Figure 6. 8. Typical microstructures of composites containing 10 % Ti sintered at (a) 600°C, (b) 700°C and (c) 1100°C for 30 minutes.	109
Figure 6. 9 The effect of sintering temperature on the TiAl ₃ particle size of a composite containing 10 wt.% Ti.	110
Figure 6. 10 Microstructure of a Ti particle reacted on the surface forming TiAl ₃ phase.	114
Figure 6. 11 A typical microstructure of the RHIPped samples consolidated at 700°C for 10 min.	115
Figure 6. 12 The growth of the intermetallic layer as a function of time and temperature.	115
Figure 6. 13 Thickness of the intermetallic layer as a function of RHIPping time. . . .	116
Figure 6. 14 Growth rate of the intermetallic layer as a function of temperature. . . .	116
Figure 6. 15 Final shape of the HIP can after HIPping.	117
Figure 6. 16 The standard of free energies of Al-chlorides and overall reaction as a function of temperature.	120
Figure 6. 17 Chemical equilibrium of Al-TiCl ₄ system as a function of temperature (the presence of species with a concentration lower than 10 ⁻² are not shown).	121
Figure 6. 18 Moles of the products in TiAl ₃ -TiCl ₄ reaction at equilibrium and various temperatures (the presence of species with a concentration lower than 10 ⁻² are not shown).	122
Figure 6. 19 Microstructure of the Al-TiAl ₃ composite produced through reactive plasma	

spraying.	123
Figure 6. 20 The results of TGA performed on reactively formed composites contaminated with chlorine. Weight changes versus (a) temperature and (b) time.	125
Figure 6. 21 Backscatter image of the reactively formed composite showing that reaction has occurred only on the surface of the powder particles.	127
Figure 6. 22 Particle status according to extent of their reaction with $TiCl_4$. P=20kW, Spray Distance=40cm, Al feed rate=20g/min, $TiCl_4$ = 15mL/min, Al feed carrier gas= 5L/min, $TiCl_4$ carrier gas= 4 L/min.	127
Figure 6. 23 Ti Concentration in the reactively sprayed deposit as a function of distance.	128
Figure 6. 24 Mass distribution as a function of distance.	129
Figure 6. 25 Particle size distribution for powders collected in the central and peripheral regions.	130
Figure 6. 26 Al-Ti phase diagram with the proposed thermal histories for Al powder particles.	132
Figure 6. 27 Microstructure of an Al particle which has undergone the thermal history Case 2.	133
Figure 6. 28 Proposed model for thermal history Case 2.	134
Figure 6. 29 (a) Microstructure, and (b) schematic model for thermal history, case 3.	135
Figure 6. 30 (a) microstructure, and (b) schematic model for thermal history, case 4.	137
Figure 6. 31 Lines of constant gas velocity (m/s) in gas atomization.	138
Figure 6. 32 . Porosity content as a function of radial distance.	140
Figure 6. 33. Rolling defects observed during rolling of Al-TiAl ₃ , (a) edge cracking, (b) center split, and (c) alligatoring.	142
Figure 6. 34 The effects of annealing time and temperature on the hardness of the Al-TiAl ₃ composite (10% Ti) rolled at 450°C with 10 % reduction.	144
Figure 6. 35 TEM micrograph showing the microstructure of the as-sprayed Al-TiAl ₃	

composite.	145
Figure 6. 36 Elongated subgrains are observed for (a) sample tested at 350°C; equiaxed substructure for samples tested at (b) 400 and (c) 450°C.	146
Figure 6. 37 (a) microstructure and (b) diffraction pattern of the dynamically recrystallized structure hot rolled at 400 °C.	147
Figure 6. 38 Very fine dispersion of TiAl ₃ in Al matrix formed during annealing at 300 °C for 196 hours.	148
Figure 6. 39 TEM microstructure of the Al-TiAl ₃ composite annealed at 450°C for 196 hours showing (a) grain growth and (b) low dislocation density.	150
Figure 6. 40 Yield strength of Al-10 wt.% Ti after annealing at various temperature.	151
Figure 6. 41 Tensile strength of the reactive plasma sprayed material.	152
Figure 6. 42 Elongation of the reactive plasma sprayed material compared with 2024-T4.	153
Figure 6. 43. (a) Fracture surface of the reactive plasma sprayed materials and (b) EDS spectrum showing the presence of Cl.	156
Figure 6. 44. Fracture surface of the material formed at a spray distance of 35 cm. . .	157
Figure 6. 45 Chloride content of the reactively sprayed materials as a function of TiCl ₄ . Flow rate. P=85kW, Ar= 110 L/min, T _{TiCl₄} = 220°C, Power/Al=1.9 kWh/(g/min), Al wire dia.= 0.24 cm, and S.D. =30 cm.	159
Figure 6. 46. Cl ₂ and Ti contents as a function of power to Al feed rate ratio. ,TiCl = 21mL/min, Ar=110 L/min, T _{TiCl₄} =220°C, Al wire dia.= 0.24 cm, and S.D.=30 cm.	159
Figure 6. 47 . Effect of wire size on Ti and Cl ₂ content of the deposit.	160
Figure 6. 48. Chlorine content of the reactively produced powder.	161

List of Tables

Chapter 2: Literature Review

Table 2.1:	Reactive plasma producing of ceramic materials	22
Table 2.2:	Experimental conditions and results for the preparation of the alloys by reactive plasma spraying	25
Table 2.3:	Diffusivity and solid solubility data for Al-alloys	28
Table 2.4:	Lattice parameters of metastable phases in mechanically alloyed TiAl ₃	29

Chapter 4: Experimental Procedures

Table 4.1:	Experimental set-up and their responses after 5 minutes of spraying	45
-------------------	---	----

Chapter 5: Plasma Atomization

Table 5.1:	Physical properties of some widely used metals	67
Table 5.2:	Experimental design and responses for liquid Al feed plasma atomization	71
Table 5.3:	Physical Properties and the Optimum Atomization Feed Rate	80
Table 5.4:	Average particle size and distribution for the atomization processes	93

Chapter 6: Al-TiAl₃ Composites

Table 6.1:	Experimental set-up and their responses after 5 minutes of spraying	98
Table 6.2:	Physical properties of Al and Ti	103
Table 6.3:	Room temperature mechanical properties of the reactively sprayed materials compared with competing materials	154

Nomenclature

c	constant
C_p	heat capacity (J/(kg.K))
d_l	ligament diameter (m)
d_m	mean particle size (m)
D_n	nominal drop diameter (m)
h_c	convective heat transfer coefficient (W/(m ² /K))
k	thermal conductivity (W/m.K)
m	mass (kg)
M/A	mass flow rate of metal to gas ratio
n	constant
p	pressure (Pa)
P	atomization pressure (Pa)
R	particle radius after transformation (m)
s	liquid sheet thickness (m)
T_e	electron temperature (K)
T_h	heavy particle temperature (K)
T_m	melting point (K)
t_{sol}	solidification time (s)
t_{sph}	spherodization solidification time (s)
v	velocity (m/s)
V	particle volume (m ³)
V_m	liquid velocity at the break up stage (m/s)

Greek Symbols

α	thermal diffusivity (m ² /s)
γ, δ	surface tension (N/m)
ΔH_m	latent heat of fusion of the metal (J/kg)
λ	wavelength (m)
μ	dynamic viscosity (Pa.s)
ν	kinematic viscosity (m ² /s)
ρ	density (kg/m ³)
τ	time elapsed to reach critical deformation (s)

CHAPTER 1

INTRODUCTION

A thermal plasma can easily be created by discharging a D.C. current into any fluid such as argon, nitrogen, helium, and water. Therefore, a power supply, two electrodes, and a plasma forming gas are required. Because of the electric discharge, an arc is established between the electrodes operating at very high temperatures. This type of thermal plasma is usually referred to as D.C. plasma. A spark plug can be considered as a very simple design of a plasma torch. Industrial plasma torches are much more complex since they should be in operation for a very long time, thus they require a very efficient electrode cooling system and durable electrode materials. A thermal plasma torch is a tool for converting electrical energy to thermal energy, and in which the plasma forming gas is a member of the electrical circuit. It is an excellent tool for gas heating, with an estimated efficiency of 75%, and cannot be easily obtained using other devices.

Another method of thermal plasma generation is by inducing electrical energy into a plasma forming gas at high frequencies called induction plasma. The equipment required for induction plasma generation is very similar to that of induction melting and uses a plasma forming gas instead of metal charge. The great advantage of the induction plasma is not having any electrode in contact with the high temperature plasma environment thus providing a diversified plasma forming gas selection. Induction plasmas are usually operated at lower jet velocity than D.C. plasmas and injected particles obtain a lower velocity in induction plasma. Therefore, a longer residence time is expected for the particles. This is an advantage when thermal plasma is used for chemical reactions. However, a low jet velocity is not very desirable for spray deposition since lower jet velocity usually results in a porous coating. In this study only D.C. plasmas were used and induction plasmas will not be discussed any further.

A thermal plasma jet is very similar to a combustion flame but operates at higher temperatures, approaching 15,000 K, whereas a combustion flame operates around a maximum of 3,000 K. In comparison with thermal plasma systems, a large volume of fossil fuel and air or oxygen is required for combustion, which raises significant environmental concerns. Thermal plasmas have found applications in: (i) spraying to form protective coatings, which will be discussed in details in Chapter two; (ii) waste destruction; (iii) gas heaters; (iv) spherodization will be covered in Chapter five; and (v) materials synthesis, which will be covered in more detail in Chapter six. Both flame and plasma spraying have been used for spray deposition. Flame spraying has limitations in production of dense refractory coatings such as: ZrO_2 or W whereas, plasma spraying can easily produce such high quality coatings.

Currently, thermal plasmas are emerging for waste destruction applications. The main advantage is low off-gas production, and effectiveness in destruction of very stable chemicals such as PCBs. Irregular powders can be injected into a thermal plasma and turn into spherical powders, which have several processing advantage over irregular powders.

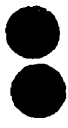
The literature is full of research information on using thermal plasmas for materials synthesis. Surprisingly, only one process has been commercialized known as the “Tioxide process” which is used for the production of TiO_2 through oxidation of TiCl_4 in an oxygen plasma. The subject of this study, i.e. “the reactive plasma spray forming of Al-TiAl₃ composites”, is ranked in this group of thermal plasma applications. The basic idea in this approach is to produce a compound of Al and Ti. However, the source of Ti is not Ti metal but TiCl_4 which is a precursor used in the production of Ti metal. As a stage in Ti extractive metallurgy, TiO_2 is chlorinated to form TiCl_4 which is then reduced by Na or Mg (Kroll’s process) to produce Ti metal. In this study TiCl_4 is reduced by Al which is easily available and is cheaper than Na or Mg. In addition, the product of this reduction process (i.e., Ti) is incorporated with Al, to produce Al-TiAl₃ composites.

Previous studies have shown that a very high temperature (above 2000 °C) is required to produce an Al-50 wt.% Ti alloy using TiCl_4 and Al. The very high temperature required for the reduction reaction justifies the use of a thermal plasma device. Due to the very short residence time of particles in a plasma jet, high particle temperatures are not usually attained. Very fine particles (1-5 μm) are required if high particle temperatures must be achieved. Injecting so fine particles into a viscous media such as a plasma jet is very difficult. Therefore, Al and TiCl_4 were injected into the apex of a triple plasma system and the products were collected on the surface of a water-cooled substrate.

Among the various methods available for feeding Al (i.e., as wire, powder, or molten), wire feeding was found the most reliable method since a precise feed rate was achieved. Wire feeding brought a completely new step into the overall process as the plasma atomization step. Al wire had to be melted and atomized into very fine particles prior to its reaction with TiCl_4 . The idea of plasma atomization is very new and no data are available in the literature. One of the achievements of this study was the development of the plasma atomization process to produce high quality powders with an average particle size of 50 μm . Chapter five is

dedicated to plasma atomization and the effects of various process parameters on particle size, size distribution, and morphology of the powder will be discussed. Plasma atomization is of commercial interest and has been qualified for patents in the USA and Canada.

Al-TiAl₃ composites, as they are referred to in this thesis, are Al-10 wt.%Ti compositions. They may be called Al-Ti alloys however, since they comprise about 30 vol.% of TiAl₃, their microstructures are very similar to those of particulate composites. The interest in Al-TiAl₃ composites is because of their high temperature mechanical properties. Al-TiAl₃ composites produced using mechanical alloying (MA) have been shown in literature to exhibit superior high temperature mechanical properties to Al alloys. Most Al alloys lose their mechanical strength at high temperatures, since their strength is achieved through fine precipitates, which redissolve in the matrix at these temperatures. Al-TiAl₃ composite can compete with some of Ti alloys already used in aerospace industry since they offer a higher specific stiffness than Ti alloys thus a significant weight reduction is achieved for structural components.



CHAPTER 2

Literature Review

2.1. INTRODUCTION

In this chapter a general background will be presented on subjects associated with plasma atomization and reactive plasma atomization, as well as Al-TiAl₃ composites. The overall background information is very broad for this research program thus it was decided to bring the literature review on gas atomization into Chapter five. This chapter covers topics including: plasma fundamentals, thermal spraying, spray forming, and reactive plasma spraying.

2.2. FUNDAMENTALS

Plasma may be defined as the fourth state of matter which consists of a mixture of electrons, heavy ions, photons, excited atoms, and neutral particles. Overall, this mixture should be electrically neutral in order to be considered a plasma. From a physical point of view,

materials in the plasma state share similar characteristics to a conductor, such as a metal. Luminosity is another characteristic of a plasma which results from the return of the excited species to their ground state followed by photon emission. From a chemical point of view, it is considered as a high temperature reactive medium with high reaction kinetics. The high energy content of plasma compared to that of other states of matter has been the centre of attention for its industrial application.

The temperature of particles in a plasma (molecules, atoms, ions, or electrons) as in any gaseous medium is defined by the average kinetic energy of the species, i.e.,

$$\frac{1}{2} mv^2 = \frac{3}{2} kT$$

therefore, the temperature of a species is a function of its mass and its velocity. It can be expected that the temperature of the electrons (T_e) and heavy ions (T_h) will be different [1]. However, this temperature difference can be equilibrated by collisions in the plasma. The extent of these collisions (as is true for gaseous medium) can be defined as a function of the energy acquired by the electrons from the electrical field (E) and the pressure (p) of the system thus

$$(T_e - T_h)/T_e = (E/p)^2$$

This relationship shows that the parameter E/p plays an important role in determining the kinetic equilibrium in a plasma. For a small value of E/p the electron temperature approaches the heavy particle temperature which is one of the criteria for local thermodynamic equilibrium (LTE) in a plasma. In general, plasmas are created over a wide range of pressures and it is more suited to classify them in terms of electron temperatures and electron densities. In this regard, cold plasmas are those plasmas which are operating in a pressure range of 10^{-4} and 1 kPa. These plasmas are characterized by an electron temperature around 10^4 K and heavy particle temperature close to ambient temperature. For example, fluorescent lamps are

classified in this group of plasmas. In contrast thermal plasmas, used in this study, approach a state of LTE where the electron temperatures on the order of 10^4 K with electron densities ranging from 10^{21} to 10^{26} m^{-3} . Thermal plasma will be the focus of this study.

2.2.1. GENERATION OF THERMAL PLASMA

Thermal plasma can be generated using: arc discharge, induction, laser, and nuclear reaction. D.C. plasma torches are devices for plasma generation using an arc discharge mechanism. These torches require two electrodes, power, water cooling, and a plasma forming gas. The arc discharge is the most common type of electrical discharge and has been used widely in industry to create a thermal plasma environment. The arc is established between two electrodes, an anode and a cathode by ionizing the plasma forming gas flowing between the anode and the cathode. As a result of this ionization, a conductive environment is created for charge transportation between the electrodes. As a result of the ionization of the plasma forming gas, high temperature is attained and a plasma state is formed. A very simple schematic of a thermal plasma torch is shown in **Figure 2.1**.

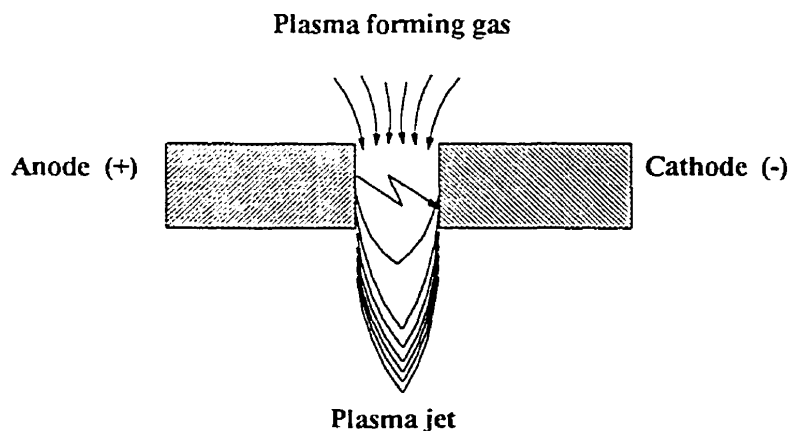


Figure 2.1 Simple schematic of a thermal plasma generating device.

2.2.2. CHARACTERIZATION OF THERMAL PLASMAS

Two important outputs of thermal plasmas are temperature and velocity. These two outputs are a function of plasma variables such as plasma gas, plasma gas flow rate, plasma power, and plasma torch design. Unlike a uniform temperature distribution in a metallurgical furnace or reactor, the temperature in a plasma jet changes sharply as a function of distance longitudinally and radially outside of the plasma torch.

2.2.2.1. Temperature Distribution in a Thermal Plasma

The temperature of a thermal plasma depends mainly on the degree of ionization which is, in turn, affected by the variables mentioned earlier. A typical temperature distribution in a plasma jet is shown in **Figure 2.2**. The temperature of the plasma jet decreases as a result of recombination and entrainment of the surrounding gases. The temperature drop in the transverse direction of the plasma jet is decreasing from approximately 10,000 K to about 1,000 K (over a distance of) few millimetres.

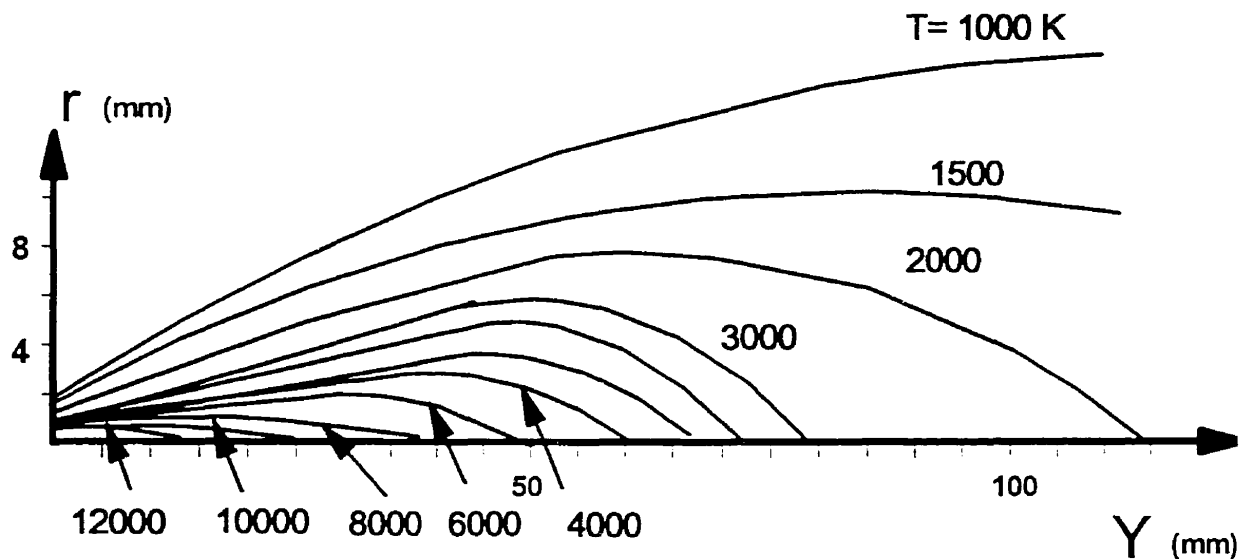


Figure 2.2 Temperature distribution in a typical thermal plasma jet.

2.2.2.2. Velocity Distribution in Thermal Plasmas

Currently, thermal plasmas are used as a tool for material processing. A knowledge of temperature and velocity distributions in such tools would be very useful for industrial and academic reasons. An example of velocity distribution in a typical thermal plasma is shown in Figure 2.3 [2]. It can be seen that the gas velocity decreases significantly in the radial direction (r) from 600 to 100 m/s over only 5 mm from the centre line of the torch exit. Similarly, the plasma jet velocity drops longitudinally (x) from 600 to 200 m/s in a 10 cm distance from the torch exit.

Plasma jet velocity determines the particle residence time in the plasma jet. The particle plasma jet velocity, in turn, defines the maximum particle temperature during plasma processing. For plasma spraying of refractory materials, a high energy is required for melting and a long residence time is preferred, while for plasma spraying of low melting (low energy required for melting) a short residence time is recommended to avoid vaporization. The most important characteristic of a thermal plasma jet is its non-uniformity. It is almost impossible for a radial injection system to provide the injected particles with the same path in the plasma jet. Therefore, particles obtain various velocities and temperatures during processing.

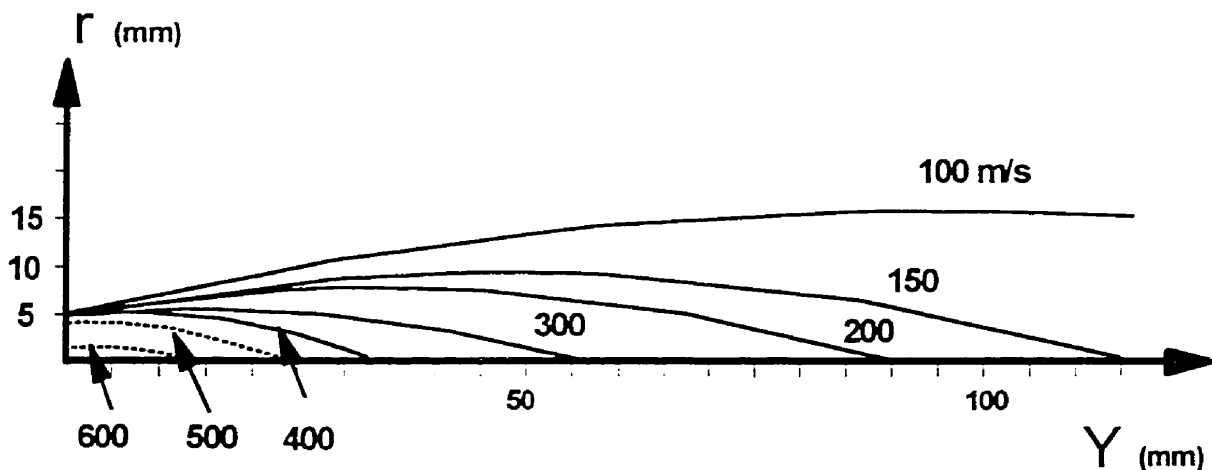


Figure 2.3 Velocity distribution in a typical thermal plasma jet.

The plasma spraying field has been the main user of thermal plasma torches. The coatings produced through thermal spray processes reflect the process capabilities. Reactive plasma spraying and plasma atomization are very similar to general thermal spraying which will be reviewed here.

2.3. THERMAL SPRAYING PROCESSING

Thermal spray processing is an established means of forming coatings of thicknesses greater than about 50 μm . A wide range of materials can be thermal sprayed for a variety of applications, ranging from gas turbine technology to the electronics industry. Thermal sprayed coatings have been produced for at least 40 years, but the last decade has seen a revolution in the capability of the technology to produce truly high performance coatings of a great range of materials on many different substrates[3].

Plasma spraying was originally developed to provide protective coatings onto surfaces of other materials. These protective coatings can be classified for chemical, mechanical and electrical applications. Most attempts have focused on structural applications providing high corrosion, oxidation and wear resistance. Plasma spray deposition offers unique features for the production of thin sections of materials which cannot be easily produced by other manufacturing processes. Although the use of advanced thermal spray coating methods has largely gained recognition within the aircraft industry, recently, many more applications of the technique have demonstrated its versatility. These include protection from wear, high temperatures, chemical attack, and environmental corrosion protection in infrastructure maintenance engineering. Of greatest importance, and making thermal spray processing uniquely important to the engineering community, are: (i) wide spray pattern resulting from a wide spray beam; (ii) high throughput versus other competitive techniques; (iii) significantly improved process control; (iv) lower cost-per-mass of applied material together with overall competitive economics.

2.3.1. Thermal Spray Processes

The principle behind thermal spray is to melt feed material (wire or powder), to accelerate the melt, to impact on a substrate where rapid solidification and deposit build-up occur. The raw material, in the form of a powder, is melted and propelled in the effluent of a jet. A large body of literature exists on the wide diversity of materials used as thermal spray feedstock [4][5]. Many different types of ferrous alloys are thermal sprayed, including stainless steel and cast iron. Light metal alloys are thermal sprayed; for example, titanium and aluminum alloys. Copper alloys, including a wide range of bronzes are sprayed, as are reactive metals including niobium and zirconium. In recent years, and very important both industrially and scientifically intermetallic alloy powders have been plasma sprayed in environmental chambers, for example, on niobium as oxidation-resistant protective coatings and as free-standing forms. Wide ranges of cermets are available plasma sprayed which produce very high strength deposits. Novel ceramics, glasses, and various high performance materials have been recently available. These materials will be the basis for new plasma spray applications in the future.[6]

In addition, a heat source and a means of accelerating the material are required [7]. The high temperature for melting is achieved chemically (through combustion) or electrically (an electric arc), which also play the role of accelerating the molten particles to the target substrate, where the material solidifies, forming a deposit. The deposit is built-up by successive impingement of these individual flattened particles or splats. Thermal spray processes are distinguished on the basis of the feedstock characteristics, (wire or powder) and the heat source employed for melting. Two important characteristics of powders in a plasma jets are powder velocity and temperature. Both of these parameters in a thermal plasma jet depend on: (i) plasma forming gas composition, (ii) plasma forming gas flowrate, (iii) torch design, (iv) distance from torch exit, (v) and plasma power. In addition, the characteristics of the powder are important. In this regard, powder size, shape, density, and its thermal

its thermal properties are important. It is not within the scope of this study to discuss the role of these factors on the particle temperature and velocity. However, it is believed that the effect of particle size on particle temperature and velocity is an important factor determining the composition and microstructure of the reactively produced deposits.

Effect of Particle Size on Particle Velocity

The velocity of the powder particles is directly proportional to the plasma jet velocity. The effect of particle size on particle velocity is shown in **Figure 2.4** [8]. Smaller particles obtain higher velocity than coarser particles in the plasma jet. It can be seen from **Figure 2.4** that 28 μm decrease in average particle size results in a 50 m/s higher particle velocity. Smaller particles accelerate and decelerate faster than coarser particles.

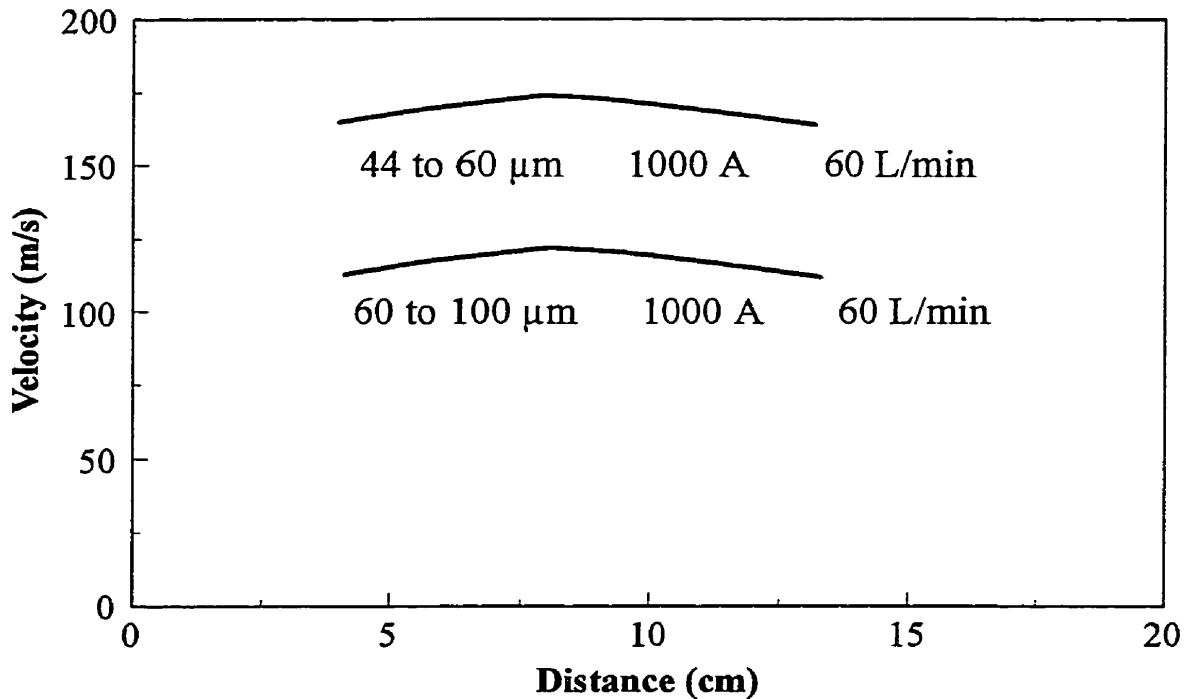


Figure 2.4 Mean particle velocity as a function of particle size of WC-Co.

Effect of Particle Size on Particle Temperature

Proper heating (melting) of powder in plasma jet is a key factor determining the coating quality. Particle overheating results in evaporation and material loss while unmelted particles act as inclusion in the coating microstructure. The effect of particle size on particle temperature as a function of distance in the plasma jet is shown in **Figure 2.5** for WC-Co[2-8].

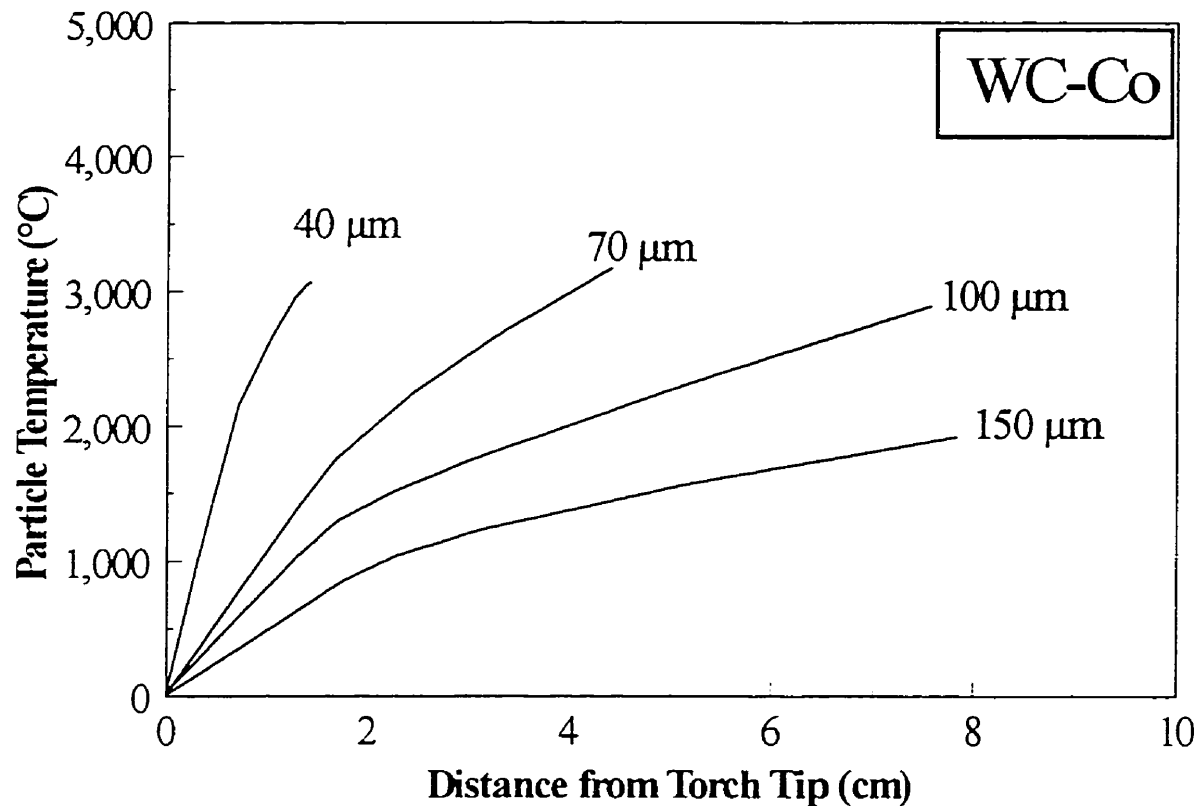


Figure 2.5 Temperature of WC-Co particles as a function of particle size in an argon plasma jet.

2.3.1.1. Combustion Flame Spraying

2.3.1.1(a) Conventional Flame Spray

In combustion flame spraying, compressed air or oxygen is mixed with a fuel, (e.g., acetylene, propylene, propane, hydrogen), to both melt and accelerate the molten particles. Traditional flame spraying yields low performance coatings and it is not employed where high density, well-bonded coatings are required. The reasons for these deficiencies are related to the relatively low flame velocity of about 50 m/s and the low temperature achieved, within the combustion flame, which is below 3000 °C. Combustion flame spraying uses either powder, wire or rod as the feedstock material and has found widespread usage around the world for its relative simplicity and cost effectiveness.

2.3.1.1(b) High Velocity Oxy-Fuel Spraying (HVOF)

A novel variation on combustion spraying has had a dramatic influence on the field of thermal spray. This technique is based on special torch designs in which a compressed flame undergoes free-expansion upon exiting the torch nozzle, thereby experiencing dramatic gas acceleration to perhaps over Mach 4[9]. By properly injecting the feedstock powder concentrically with the flame, the particles are subjected to velocities so high that they will achieve supersonic values. Therefore, upon impact onto the substrate, the particles spread out very thinly and bond well to the substrate and to all other splats in their vicinity yielding a well adhered and dense coating comparable to plasma sprayed coatings. It should be noted, however, that the powder particles are limited in the temperature achieved due to the relatively low temperature of the combustion flame. It is, therefore, not currently possible to process refractory ceramics using, this technique. However, of particular importance is the fact that HVOF hard facings (e.g., WC/Co) have hardnesses and wear resistances superior to such materials plasma sprayed in air.

2.3.1.2. Arc Spraying

Two-Wire Electric Arc Spraying

This process involves two current-carrying electrically conductive wires fed into a common arc point where melting occurs[10]. The molten material is continuously atomized by compressed air forming a spray of molten metal with a very high material throughput, as high as 40 kg/hr. This is the highest rate in standard industrial level thermal spray guns which yields highly cost effective spraying of corrosion resistant zinc and aluminum in the marine industry and for infrastructure applications. Modern developments have led to electric arc guns which can operate in inert atmospheres, using argon or nitrogen atomization and spraying reactive metals, such as zirconium and titanium for corrosion protection in the chemical industry.

2.3.1.3. Plasma Spraying

A plasma spray gun operates on direct current, which sustains a stable non-transferred, electric arc between a thoriated tungsten cathode and an annular water-cooled copper anode[11]. A plasma gas is introduced into the gun and the electric arc from the cathode to the anode completes the circuit forming a plasma jet, as shown in **Figure 2.1**. The temperature of the plasma just outside the nozzle exit is effectively in excess of 15,000K for a typical D.C. torch operating at 40 kW. The plasma temperature drops rapidly from the exit of the anode, and therefore the powder to be processed is introduced into the hottest part of the flame. The powder particles, approximately 40 micrometers in diameter are accelerated and melted in the flame on their high speed (100-300 m/sec) path to the substrate, where they impact and undergo rapid solidification (10^6 K/sec). Plasma spray is used to form deposits of greater than 50 micrometers of a wide range of industrial materials including nickel and ferrous alloys, refractory ceramics, such as aluminum oxide and zirconia-based ceramics.

2.3.1.3(a) Vacuum Plasma Spray (VPS)

Vacuum plasma spraying also known as low pressure plasma spraying process was developed by Muehlberger in the early 1970's and gained widespread commercial use to replace EB-PVD (electron beam physical vapor deposition) for the production of high quality metallic (MCrAlY) coatings in the mid-1980's[12]. For high performance applications, in order to approach theoretical bulk density and extremely high adhesion strength, plasma spray is carried out in a reduced pressure (between 50 and 200 mbar) inert gas chamber. The plasma jet velocity is increased within the reduced pressure chamber which increases the particle velocity and upon impact onto the substrate a very dense coating is formed. The advantages of VPS over other thermal spray processes are: (a) capability of substrate preheating to about 1000 °C with minimum surface oxidation; (b) higher particle velocity on impact which results in a denser coating; and (d) possibility of transferred arc cleaning of the substrate prior to spraying. A further major advantage of the VPS process is the ability to process oxygen sensitive material such as reactive metals, and intermetallic compounds[13][14]. For example, considerable work has been carried out on the VPS processing of nickel aluminides and molybdenum disilicide, which have potential uses in the aerospace industry. Some studies have been published on the VPS processing of composites based on Ni₃Al and MoSi₂. High density deposits are obtained and some promising toughness increases are found[15]. There is significant potential for VPS in the processing of intermetallics as both protective coatings and as free-standing forms. The disadvantages of this process are: (a) it is a batch process; (b) its complexity; and (c) higher cost than conventional atmospheric process.

2.4. RECENT PROGRESS IN THERMAL SPRAY PROCESSES

Traditional plasma spray guns are gas vortex stabilized and operate in the 40 to 80 kW power range. By using water stabilization it is possible to operate at considerably higher power levels, in the range of 160 kW and beyond, allowing a material throughput of some 30 times

that of gas stabilized torches [16]. With this enhanced material handling capability it becomes practical to consider spray forming of structural shapes and high production thick thermal barrier coatings such as those required in abradable seal applications.

At the other end of the thermal spray spectrum is the limitation in obtaining thin films. A major limitation of traditional thermal spray technology has been the thinness of a deposit could be formed. Fine-sized feedstock particles ($>5 \mu\text{m}$) would be required for the production of thin films. To force fine particles into such a flame would require increasing the carrier gas pressure, leading to increased flame turbulence, and thus to a disturbed particle trajectory. These problems could be largely solved by using axial injection of the material feedstock. New axial-feed plasma gun designs can avoid many of the limitations imposed by non-axial plasma devices. The operation of one such axial gun is based on "electromagnetic coalescence" (EMC), allowing four off-centered coalescing 1 kW pilot plasmas to transfer energy to a downwind central anode. The feedstock material in the form of fine powder or sol gel fluid is injected axially using essentially any carrier gas such as oxygen, hydrocarbon, or a diamond-forming reactive gas enabling for example thermal plasma CVD reactions. The nozzle is designed to preclude internal contact of the feed material with the internal diameter of the anode[17].

2.5. PARTICLE-PLASMA INTERACTION AND PROCESS CONTROL

Over the last decade a number of research programs have been examining particle-plasma interactions, employing sophisticated diagnostic tools[18][19]. These include laser-strobe vision for particle trajectory and injection studies, enthalpy probe for plasma temperature measurements, laser-Doppler velocimetry for determination of particle velocity, and optical pyrometry for particle temperature analysis.

The interaction between a solid particle and the plasma jet is very important, because this interaction should result in proper melting of the feedstock powder. The particle on its introduction into the flame or jet must collect sufficient kinetic energy in order to accelerate towards a substrate, and to absorb sufficient enthalpy from the flame to melt. In modelling, the plasma effluent experiences no turbulence and the particle on entering the plasma jet causes a change in the jet. However, the jet is generally non-laminar and the carrier gas which transports the particle does disturb the jet, creating significant jet distortions. In reality, thermal plasmas are very different from the ideal assumptions, making model building so difficult.

2.6. DEPOSITION DYNAMICS

Thermally sprayed deposits are comprised of cohesively bonded splats which result from a high rate of impact and rapid solidification of molten particles, ranging in size from 10-100 μm [20]. The physical properties and behavior of such a deposit will be expected to depend on the cohesive strengths among the splats, the size and morphology of the porosity, the occurrence of cracks and defects and, finally, on the ultrafine-grained microstructure within the splats themselves.

The microstructures of thermally sprayed deposits are ultimately based on the solidification of many individual molten droplets. A splat results when a droplet of molten material, tens of micrometers in diameter melted in the flame strikes a surface, flattens out, and solidifies. There are numerous considerations relative to the dynamics of deposit evolution during thermal spraying. The physical aspects of splat formation deals with the spreading of the molten droplet and its interactions with the substrate. These characteristics are affected by the temperature of the splat, the splat viscosity, surface tension, as well as substrate temperature and roughness. Splat morphology depends on particle velocity, temperature, diameter and substrate surface profile. Further considerations involve the physical properties

of the splat, which deal with cooling rate, solidification criteria, nucleation and growth of crystals, and phase formation. The above aspects of splat formation and solidification are complex, and interrelated.

Physical aspects of splat formation through heat transfer and mechanical models have been described in considerable detail[21]. Two major splat morphologies have been reported as "pancake type" and "flower type". It has also been shown that splat morphology is affected by the velocity of the impinging droplet. Increased velocity leads to enhanced flattening, and spreading of the droplet. It was further shown that the splat shape factors influenced by spray angle which have a strong effect on deposit characteristics, such as porosity, deposition efficiency, and microhardness.

The cooling and solidification rates for thermally sprayed deposits depend on the solidification of individual splats. Cooling rates as high as 10^7 K/s have been reported for deposits sprayed by air plasma spraying[22],[23]. Moreau et al. have shown cooling rate of 10^8 K/s plasma spray deposition of molybdenum and niobium particles on conducting substrates using a two-color pyrometer[24][25]. This indicates that the splats undergo ultra-rapid quenching during thermal spraying.

The high solidification rates and the G_i/R (degree of constitutional supercooling) values suggest a plane front growth as the likely mode of solidification. Further, it has been shown that texture is likely in these columnar solidified deposits because under high solidification rates, it is expected that the fastest crystal growth direction will prevail. X-ray diffraction results from the reverse-side of atmospheric and vacuum plasma sprayed nickel, Ni-5%Al, and molybdenum alloy deposits showed strong $\langle 100 \rangle$ type texture [26].

2.7. MATERIALS SCIENCE OF THERMAL SPRAY DEPOSITS

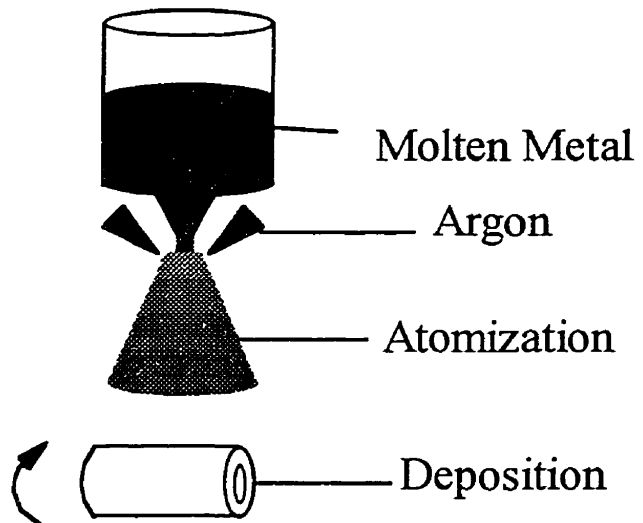
The model for microstructure development during thermal spray deposition suggests, heterogeneous nucleation of a solid phase followed by columnar growth. The high cooling rates (rapid solidification rates) suggest massive or partitionless solidification via supercooling. This associated with large undercooling is expected to result in considerable solute trapping and the formation of metastable phases. Metastable phases are a frequent occurrence in thermally sprayed materials. Solid solubility extension has been reported in numerous plasma sprayed systems, namely: Krishnanand and Cahn in Al-Cu, Bhat *et al.* in Fe-C [27], and Sampath and Wayne in Mo-C [28]. Metastable and amorphous phases are observed commonly in plasma sprayed ceramics; namely: gamma alumina, amorphous cordierite, amorphous, hydroxyapatite, tetragonal zirconia, etc. In addition to formation of metastable phases, thermal sprayed deposits typically show nanometer to sub-micron grain size distributions associated with rapid solidification[29]. All of the above features have interesting implications for physical, and mechanical properties of the deposits.

Thermal spray condenses four processing steps, namely rapid melting, deposition, forming and rapid solidification, into a single step. Rapid melting reduces the time that the molten material is subjected to an undesirable environment resulting in less inclusions in the final product. In the deposition step, the molten particle is transferred to the substrate, without contacting any other material, over a very short time period. This is mainly because the particles introduced into the plasma jet travel at high velocity (i.e. close to the velocity of the plasma gas). The latter also provides a high impact energy to the particles, forming a dense coating upon impact with the substrate. Subsequently, this eliminates any post mechanical processing. Since forming occurs in a molten or semi molten state, deformation is facilitated to a large degree. Finally, through the rapid solidification step, a very fine microstructure, a high degree of chemical homogeneity and a high mechanical strength are obtained. This is a direct result of the high solidification rates associated with the process (10^6 °C/sec)[30],[31].

In addition, metastable phases with unique properties can result from rapid solidification; providing an overall improvement in bulk properties. The dispersion potential of strengthened materials benefit from the extension of the range of solid solubility and chemical homogeneity inherent to the process. It should be noted that there is a variety of non-solid fed thermal spray methods which can produce coatings and near-net-shapes. The most developed process in this category is known as Osprey process.

2.8. OSPREY PROCESS

Most of the spray deposition processes are used to provide the base material with a protective coatings. However, some spray deposition processes such as Osprey process have been developed for the production of bulk structures. In this process, molten material is directly atomized and spray formed onto a mandrel moving in a trajectory designed to produce the desired final part shape, as show in **Figure 2.6**. While the throughput of this method is high, the melt particle velocity is not high, leading to a structure of poor density, which generally needs further post-deposition processing.



Using this process, very fine microstructure can be achieved with the corresponding increase in component strength. In addition, complex materials such as metal matrix composites can be produced via the introduction of particles directly into the spray. Therefore, the process offers the potential of high quality, at a reduced cost, due to a reduction in post processing of the final components[32].

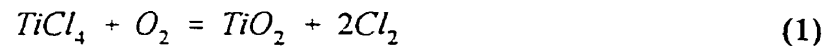
2.9. REACTIVE PLASMA SPRAYING

In conventional plasma spraying, no reaction occurs in the plasma jet. The plasma energy is used to melt and deposit materials on the surface of a substrate. By contrast in reactive plasma spraying the plasma energy is used for melting, reaction, and deposition. The starting materials can be fed in the form of gas, liquid or solid to the plasma leading to the synthesis of new materials. This, in general, can be divided in two main categories and are liquid-gas and gas-gas reactions. In the gas-gas reaction, the reaction usually takes place in the flame and the products are collected either on the substrate as a deposited layer or as a loose powder. The concept of gas-gas reaction has been generally used to produce ultrafine nitride, carbide and oxide ceramics, and also to synthesize composite materials. Table 2.1 summarizes some of these activities.

Table 2.1. Reactive plasma producing of ceramic materials.

Compound	Starting Materials	Plasma Type	References
Si_3N_4	$\text{SiCl}_4 + \text{NH}_3 + \text{H}_2$	RF/Arc	Vogt[33] and Yoshida[34]
AlN	$\text{Al} + \text{NH}_3$	RF	Canteloup[35]
TiN	$\text{Ti/TiCl}_4 + \text{N}_2$	RF	Yoshida[36]
SiC	CH_3SiCl_3	Arc	Salinger[37]
	$\text{SiH}_4 + \text{CH}_4$	RF	Vogt[2.33]
TiC	$\text{TiCl}_4 + \text{CH}_4 + \text{H}_2$	Arc	Kong[38]
Al_2O_3	$\text{Al/AlCl}_3 + \text{O}_2$	RF/Arc	Barry[39]
SiO_2	$\text{SiCl}_4 + \text{O}_2$	RF	Audsley[40]

The only commercial process using reactive thermal plasma synthesis is the “Tioxide process” [41]. Titanium dioxide pigment is the product of this process and has applications as opacifier in paints, plastics and paper. The titanium dioxide pigment opacifier should be in a size range of 0.25 μm , have a narrow particle size distribution, and free from metallic impurities. The process is based on the oxidation of TiCl_4 ,

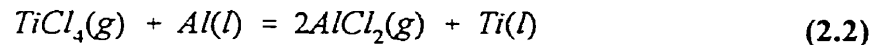


and is an exothermic reaction. Oxygen is the plasma forming gas which reaches a very high temperature and reacts with TiCl_4 (injected at the torch exit) to form TiO_2 . This oxidation reaction occurs at very high temperatures ($<1000^\circ\text{C}$) thus very fine oxides are formed with a high reaction rate. The main advantage of this process is to benefit from the gas-gas reaction between O_2 and TiCl_4 . TiO_2 nucleates at high temperatures and quenches rapidly resulting in a very fine size range particles. Similar approach has also been adopted for the production of ZrO_2 where ZrCl_4 has been used instead of TiCl_4 [42].

There is very little literature [43], [44] available on the synthesis of metallic materials using reactive plasmas. Roneshim et al [2.43] studied the formation of intermetallic phases such as V_3Si , VSi_2 , NbSi_2 , NbGe_2 , Cr_3Si and Mo_3Si in a D.C. argon plasma. The results of these sets of experiments are summarized in Table 2.2. Tsunekawa *et al.* [2.44] used elemental powders of Al and Fe to synthesize iron aluminide by reactive low pressure plasma spraying. He has also produced a TiAl matrix containing Ti_2AlN particles by injecting elemental Al and Ti powders to a D.C. plasma containing N_2 in the plasma gas [45]. Castro injected Si_2H_6 , CH_4 , and Mo powder into the plasma flame in order to form MoSi_2 and strengthen it with SiC [46]. A lamellar microstructure of silicide phase, identified as Mo_3Si_5 , in a Mo matrix has been reported. It is seen in most of the reactive plasma spray processes involving a liquid-gas reaction that an incomplete reaction (only a surface reaction) takes place. Upon deposition the reacted shell spreads out and forms a lamellar microstructure.

Lu and Pfender used a triple plasma torch system to synthesis AlN by injecting a very fine Al powder (1 to 2 μm) into Ar (6 L/min)-N₂ (7 L/min) plasma jets operating at 18 kW each [47]. It is reported that Al peaks have been identified in the products meaning that full conversion of Al to AlN did not occur. It has been mentioned that the main goal of using a triple plasma configuration is the capability of the process to feed very fine powders thus complete evaporation of particles are achieved. No data have been reported for the Al feed rate however, the power per liter of the plasma forming gas was estimated to be 1.4 kW/L.

Nagamori developed a computer model for mathematical simulation study of the TiCl₄-Al reaction [48]. The main reaction has been expressed as



where metallic Ti produced forms an alloy with excess Al metal. In this model, the effects of temperature, pressure, dilution with argon gas, and TiCl₄/Al ratio have been studied on the alloy composition and Ti recovery. Complete reactions between TiCl₄ (g) and Al (l) and a very long reaction time have been assumed for the model. One of these computer models is given in Appendix 1. Using this model, it was concluded that at 4340 K one mole of TiCl₄ reacts with four moles of Al to produce an Al alloy containing 50 wt.% Ti at one atmosphere gas pressure. This corresponds to a 98.6% recovery of Ti from TiCl₄.

Furthermore, using this computer model, it is concluded that the Ti recovery is increased by increasing the Al/TiCl₄ ratio. However, it is not a strong function of temperature or pressure. High Al/TiCl₄ ratio produces an alloy with low Ti concentration while a high Ti recovery is obtained. Lower pressure also favours slightly higher Ti recovery and a higher Ti concentration but its effect is not very significant.

Table 2.2. Experimental conditions and results for the preparation of the alloys by reactive plasma spraying. [2.43]

Powder Mixture	Injection rate, l/min	Power input		plasmagas		Product	
		Torch	Transfer	gas	l/min		
V, Si	Ar	25	100 A 25 V	150 A 55 V	Ar	14	40% VSi ₂ , 60% Si
V, Si	H ₂	10	700 A 45 V		Ar	19	Product pyrophoric
V, Si	Ar	10	900 A 25 V		H ₂	2	Metallic product in C-tube: VSi ₂
Nb, Si	Ar	20	900 A 25 V		Ar	20	50% V ₃ Si, 50% V
Nb, Ge	Ar	25	900 A 25 V		Ar	16	40% NbSi ₂ , 60% Si Metallic product in C-tube: 90% Nb ₅ Si ₃ , 10% Nb
Nb, Ge	H ₂	10	700 A 45 V		Ar	19	100% Ge
Nb ₃ Ge	Ar	10	800 A 25 V		Ar	19	40% NbGe ₂ , 5% Nb ₅ Ge ₃ , 55% Ge
Nb ₃ Ge	Ar	10	800 A 25 V		H ₂	1.4	Multiphase product containing Nb, Ge, GeO ₂ , NbGe ₂ , and unidentified phases
Nb ₃ Ge	Ar	10	800 A 25 V		Ar	2.4	
Nb ₃ Ge	Ar	10	800 A 25 V		Ar	27	50% Nb, 10% Ge, 30% Nb ₃ Ge (with $a=5.156\text{Å}$) 5% Nb ₅ Ge ₃ , 5% NbGe ₂
Cr, Si	Ar	20	100 A 25 V		Ar	14	Multiphase product
Cr, Si	Ar	15	900 A 25 V	150 A 55 V	Ar	16	90% Cr ₃ Si
Cr ₃ Si	Ar	10	800 A 25 V		Ar	24	90% Cr ₃ Si, 5% CrSi ₂ , 5% Cr
Mo, Si	Ar	10	100 A 25 V		H ₂	2.4	
Mo, Si	Ar	10	100 A 25 V		Ar	14	95% Mo, 5% Si
Mo ₃ Si	H ₂	6	700 A 45 V	155 A 55 V	Ar	19	90% Mo ₃ Si ($a = 4.915\text{Å}$), 10% Mo
Mo ₃ Si	H ₂	6	700 A 45 V	155 A 55 V	H ₂	2	
Mo ₃ Si	Ar	10	800 A 25 V		Ar	24	35% Mo ₃ Si, 35% Mo ₃ Si ₃ , 30% Mo
Mo ₃ Si	Ar	10	800 A 25 V		H ₂	2.4	

2.10. AEROSPACE REQUIRMENTS

2.10.1. Density

Numerous research activities are currently involved in the development of advanced materials for aerospace applications. Studies on various types of aerospace vehicles have verified that a reduction in density is the most important material property for achieving a better performance[49]. Density is often three to five times more effective in reducing structural weight than are proportional changes in strength, fracture-toughness, modulus of elasticity, or fatigue properties, as shown in **Figure 2.7**. Among the elements listed in Table 2.3, Ti offers the highest weight saving as an alloying element in Al for high temperature applications.

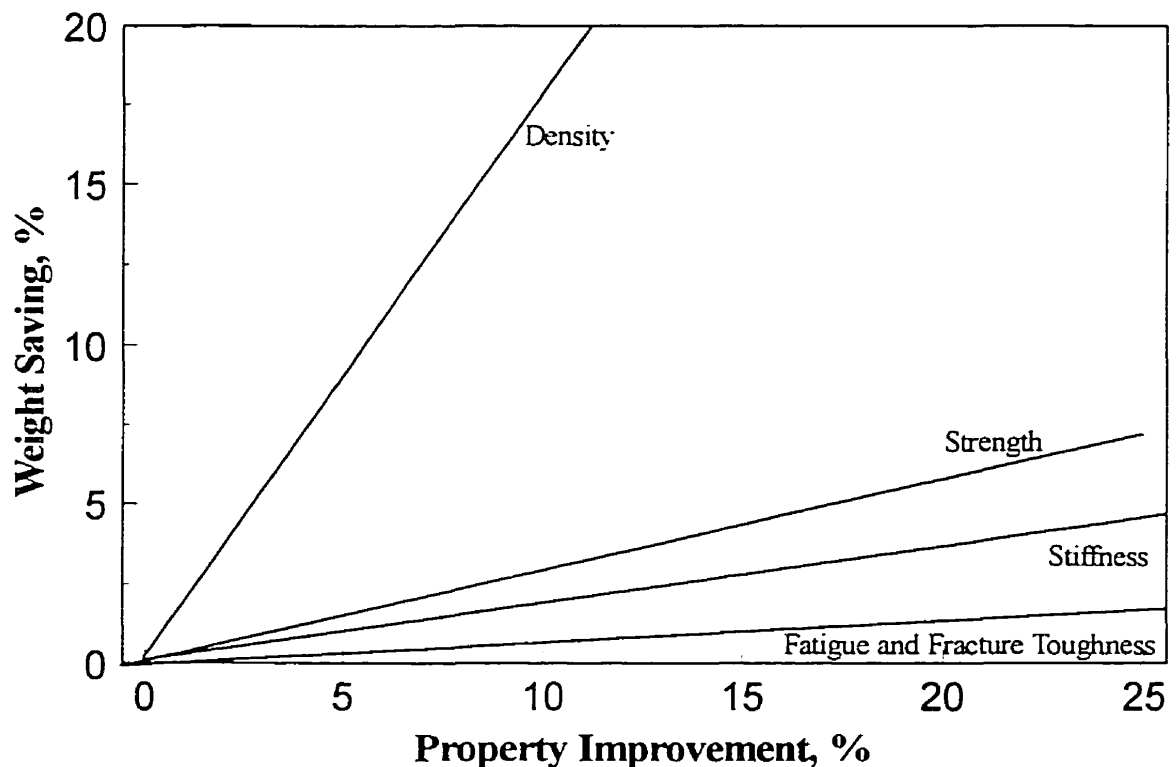


Figure 2.7 The relative effects of various material properties on reducing structural weight in a Lockheed S-3A aircraft.

2.10.2. Microstructure

Microstructural conditions necessary to attain maximum strength include a high volume fraction of intermetallics, a fine intermetallic particle size, a uniform particle distribution, and a thermally stable particle. Fabricated products should exhibit the highest yield and tensile strengths. Conventional metallurgical processes are not capable of producing such products.

The air-atomized powder of Al-Fe-Ni-Co found to have the smallest, most uniform particles exhibited the highest strengths when compared with the argon splat and air splat material [50].

In the same study, it has been shown that alloys containing up to 25 vol.% second phase show an increased strength-toughness relationship, while the reverse is observed for alloys containing more than 25 vol.% second phase.

For elevated temperature applications, the alloy microstructure must exhibit a prolonged thermal stability, and the dispersed phase in the microstructure must be thermodynamically stable. Moreover, in order to maintain the alloy strength and, in addition to have acceptable fracture properties, the dispersed phase should resist coarsening when the alloy is exposed to elevated temperatures. The driving force for coarsening is a reduction in overall interfacial energy of the system, and the mechanism for coarsening may be volume diffusion controlled, grain-boundary or substructures diffusion controlled, or interface controlled. An ideal high temperature Al alloy, therefore, would have the following characteristics [51]:

- (a) low diffusivity of solute in the Al matrix,
- (b) thermodynamically stable dispersed phase, and
- (c) low interfacial energy between the matrix and the dispersed phase.

2.11. HIGH TEMPERATURE Al-ALLOYS

2.11.1. Al-Zr-V Alloys

Table 2.3 lists the volume diffusivities at 427°C for a number of alloying elements in Al. The lowest diffusivity belongs to Zr. It forms a metastable $L1_2$ phase, Al_3Zr , which precipitates at high temperatures. This phase is quite stable at normal solution treating temperatures and is an effective grain refiner for Al-alloys. The solid solubility limit of Zr in Al is very small. Therefore, an effective high temperature alloy cannot be made by conventional ingot metallurgy. With arc melting on a water cooled Cu cathode using a W electrode, the solidification rate is fast enough to dissolve enough Zr to give 1 vol.% cubic Al_3Zr on ageing. Zedalis [52] showed that the mismatch between cubic Al_3Zr and Al alloy matrix is reduced on partially substituting V for Zr, reaching zero at approximately the $Al_3(Zr_{0.2}V_{0.8})$ composition[53].

Table 2.3 : Diffusivity and solid solubility data for Al-alloys.

Alloy System	Maximum Solid Solubility, C_B , at. %	Diffusivity at 427°C at.% cm ² /sec
Al-Ti	0.8	3.86×10^{-15}
Al-V	0.2	3.94×10^{-15}
Al-Cr	0.42	2.3×10^{-14}
Al-Mn	0.92	2.12×10^{-10}
Al-Fe	0.026	1.12×10^{-15}
Al-Co	0.45	2.15×10^{-11}
Al-Ni	0.023	8.4×10^{-15}
Al-Cu	2.45	1.6×10^{-10}
Al-Zr	0.07	6.6×10^{-17}
Al-Nb	0.065	1.9×10^{-14}
Al-Mo	0.07	6.03×10^{-15}

2.11.2. Al-Fe-Si-V Alloys

The leading high temperature commercial Al alloys developed so far are the Al-Fe-V-Si alloys by Allied-Signal Inc. [54],[55]. and are made using planar flow casting. For example, alloys FVS-0812 (with 8 %wt Fe, 1 %wt V and 2 %wt Si) and FVS-1212 (with 12 %wt Fe, 1 wt% V and 2 wt% Si) display exceptionally high strengths at 315°C and usable strengths upto 425°C. These alloys contain high-volume fractions of silicides that also increase the elastic modulus. The dispersed silicides are so fine that they greatly contribute to high strength over a wide temperature range.

2.11.3. Thermal Stability in the Al-TiAl₃ System

St. John et al. [56] studied the stability of an unidirectionally solidified Al-2 wt% Ti alloy by annealing it for 24 hrs. at 435, 535, 635 and 660°C. They concluded that TiAl₃ particles are stable up to a temperature of about 500°C and above this temperature, the particles tend to spheroidize. They also reported a diffusion coefficient of $2 \times 10^{-11} \text{ cm}^2 \text{ sec}^{-1}$ for Ti in Al at 635°C. Srinivasan et al. [57] followed another approach by mechanical alloying (MA) of Al and Ti powders to prepare their specimens. It was concluded that TiAl₃ occurs with the L1₂ structure. This structure is then transformed into an intermediate metastable DO₂₃ phase during annealing, before transforming into the stable DO₂₂ phase. The lattice parameters of these metastable phases and their mismatches with Al are reported in Table 2.4.

Table 2.4: Lattice parameters of metastable phases in mechanically alloyed TiAl₃ [58].

Lattice Parameters (nm)					% Mismatch of a ₀ to Aluminum		
L1 ₂	DO ₂₃		DO ₂₂		L1 ₂	DO ₂₃	DO ₂₂
a ₀	a ₀	c ₀	a ₀	c ₀			
0.397	0.389	1.682	0.385	0.861	2.0	3.9	5.4

The Al rich section of Al-Ti phase diagram ranging from 0.003 to 0.015 % has been interesting for casting of Al alloys.[59] Ti is widely used as grain refiner for Al alloys. There is no doubt that $TiAl_3$ is an active nucleus for Al because it is found at the centers of Al grains and there is well-established orientation relationship between the lattices of the two phases.[60]

Ti in solution in the liquid metal at a concentration above about 0.15 at. % would be expected to be precipitated as $TiAl_3$ in the peritectic reaction shown in Figure 2.8.[61] In this peritectic reaction, the liquid phase plus $TiAl_3$ form an Al solid solution, in which the maximum Ti solubility is about 0.7 at. %.[62]

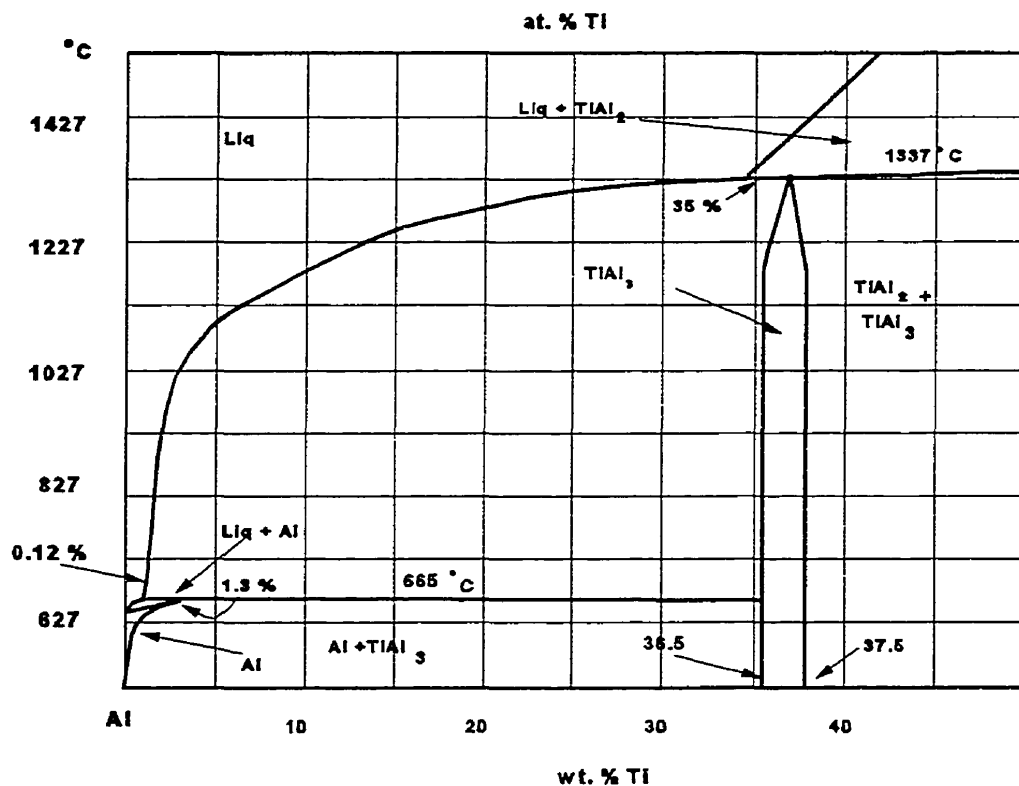


Figure 2.8 Al-rich section of Al-Ti phase diagram.

2.11.4. Al-Ti System

Recent research has shown that rapid solidification and mechanically alloyed Al-Ti Alloys have good ambient and elevated temperature properties [63],[64],[65]. The aluminide, TiAl_3 , can be formed either during solidification, as a result of a peritectic transformation or during precipitation from a Al-Ti solid solution as shown in Figure 2.8. A peritectic phase transformation occurs at 665°C and 1.15 wt%, i.e., $\text{L} + \text{Al}_3\text{Ti} \rightarrow \alpha(\text{Al})$. [66] The exact wt.% Ti contained in the first solid to form during the peritectic decomposition is reported to be between 1.15-1.3%. [67] At the transformation temperature, Ti solubility in the liquid is 0.12 wt.%. TiAl_3 has a body centered tetragonal structure, space group $I4/mmm$, with 8 atoms/unit cell and lattice parameters of $a = 0.3851 \text{ nm}$ and $c = 0.86 \text{ nm}$ with a density of 3370 kg/m^3 . [68] Precipitation of TiAl_3 from a supersaturated solid solution has been reported to result in an intermediate metastable semicoherent phase, TiAl_3' . This phase is believed to be similar to the cubic $\text{Al}_3\text{Zr}'$ phase [2-67]; and may belong to the space group $P_6 3/mmc$. [69]

2.11.5 Mechanical Properties of Al-Ti alloys

The MA Al-Ti alloys have been extensively investigated. [70], [71], [72], [73], [74], [75]. The modulus values were reported to be about 86 to 103 GPa. This shows a significant advantage in specific stiffness at ambient temperature compared to either the competing Al-Fe-X (X= V, Si) type Al materials or Ti-6242 alloy. Figure 2.9. shows this comparison vs temperature. The MA Ti-Al has higher specific stiffness than other materials up to 371°C . This is attributed to the presence of a significant amount of TiAl_3 which increases stiffness and to the minimal increase in density resultant from the Ti additions. The comparison of specific strength of MA Al-Ti alloy with other materials results in a lower strength than the Ti-6242 alloy but lie within conventional Al-alloys.

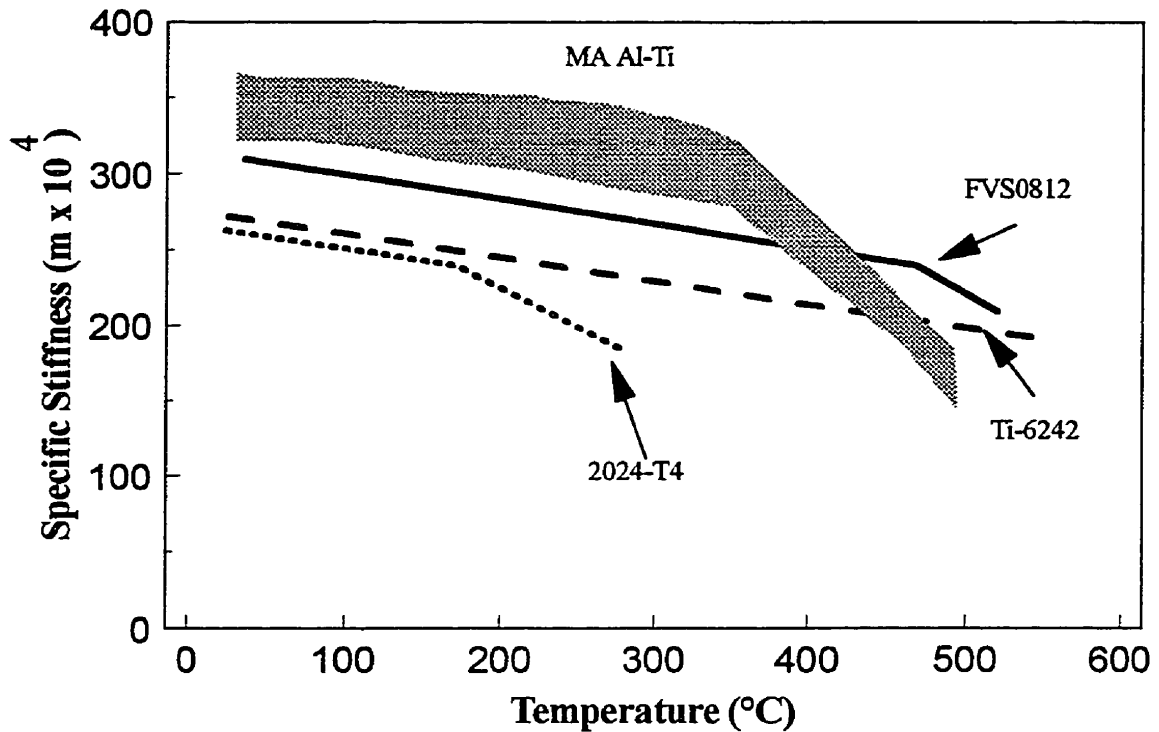
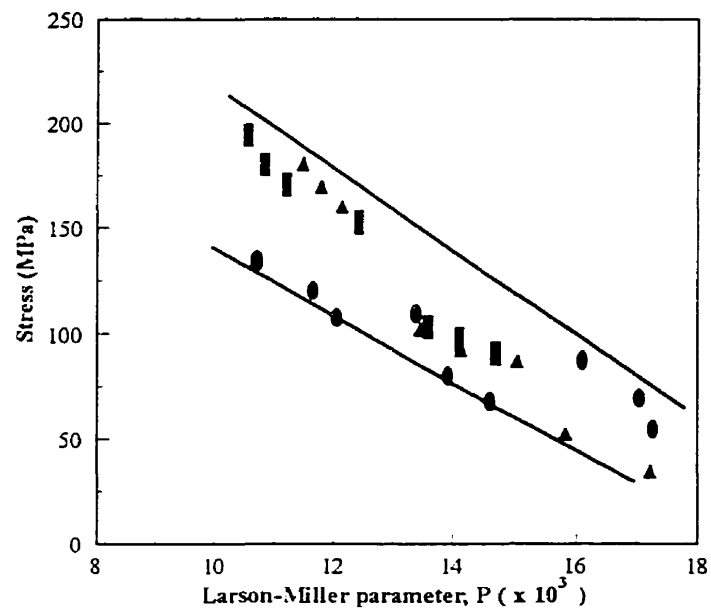
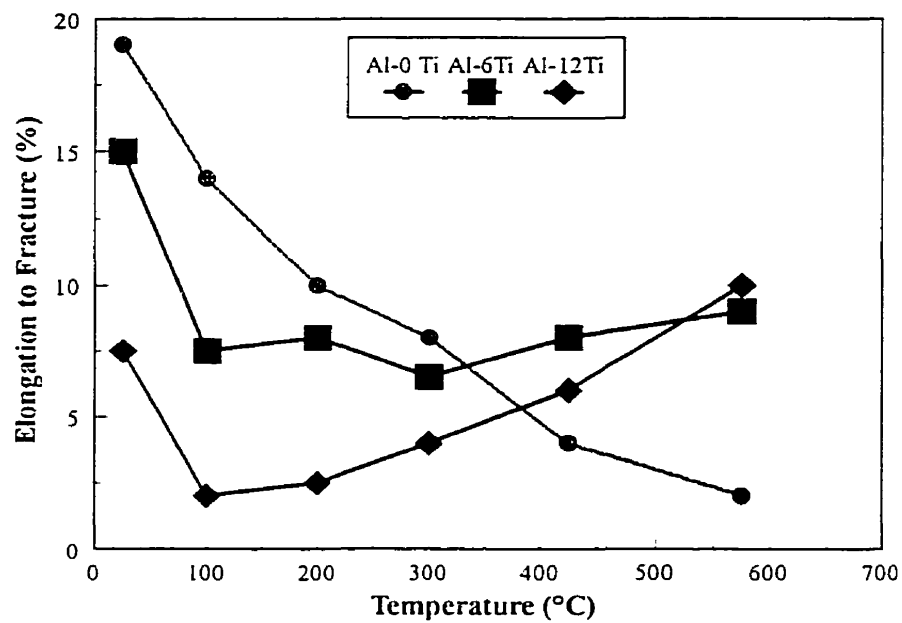


Figure 2.9 Specific stiffness for MA Al-Ti alloys compared to current and competitive elevated temperature alloys. [2-70]

Mirchandani et al. [2-71] evaluated the creep-rupture properties of MA Al-(0-12Ti) alloys. The results are summarized in **Figure 2.10 (a)** and show that alloys containing Ti exhibit higher rupture strengths in the low temperature-high stress regime whereas at high temperature, they exhibit lower rupture strengths. It can be concluded that the $TiAl_3$ dispersoids exert a stronger influence in controlling the rupture stress at lower temperatures. They have also found that elongation to fracture at room temperature decreases by increasing Ti content. The elongation to fracture behavior of MA Al-alloys containing 0-12 wt.% Ti as a function of temperature is illustrated in **Figure 2.10 (b)**. MA Al exhibits a monotonic decrease in ductility with increasing temperature before 200°C followed by increasing in elongation to fracture.



(a)



(b)

Figure 2.10 (a) Creep-rupture properties of MA Al alloys in the temperature range 315-535 $^{\circ}\text{C}$ (b) Variation in the ductility of MA Al alloys with temperature.

This is the intrinsic characteristics of FCC metal with high stacking fault energies i.e. crystal structures with high stacking fault energy exhibit a decrease in ductility with increasing temperature[76]. However, these data contradict data reported in other literature,[77] where the elongation to fracture increases with increasing temperature, i.e. this is more conventional behavior, since plastic flow processes become easy with increasing temperature. On the other hand, alloys containing Ti initially exhibit a decrease in ductility up to some intermediate temperature, followed by an increase in ductility. That has been attributed to the presence of $TiAl_3$ particles and the constraint they can provide. It is also postulated that the $TiAl_3$ particle can develop a multi-axial stress state locally within Al grains in their vicinity altering the slip behavior on planes of maximum shear stress (i.e. planes inclined at 45° to the tensile axis). Hence, slip occurs in a larger number of Al grains providing higher ductility.

CHAPTER 3

OBJECTIVES

The objectives of this study were to:

- 1- Synthesize Al-TiAl₃ composites through reactive plasma spraying using TiCl₄, Al powder, and single plasma torch, in order to confirm previous findings reported in the literature.
- 2- Produce Al-TiAl₃ composites through other metallurgical processes such as casting, powder metallurgy, HIPping, as well as vacuum plasma spraying for comparison with reactively produced materials.
- 3- Synthesize of Al-TiAl₃ composites through reactive plasma spraying using TiCl₄, Al wire or molten Al, using a triple plasma system for comparison with products obtained using a single plasma torch.
- 4- Characterize the powders produced by plasma atomization in terms of average particle size, size distribution, and production rate; also, optimize the process parameters such as wire feed rate, plasma power, and reactor geometry in order to obtain a suitable product for reactive plasma atomization.

- 5- Characterize reactive plasma atomization deposits in terms of microstructural uniformity and distribution of porosity through the deposit. Furthermore, to develop the properties of the deposits through a post treatment process such as HIPping or rolling.

CHAPTER 4

EXPERIMENTAL

PROCEDURES

4.1. Introduction

Two major experimental procedures were undertaken during this study: reactive plasma spraying, and plasma atomization using a triple plasma configuration. Although single plasma atomization was used, emphasis was placed on the triple plasma system.

Reactive plasma spraying was used to react Al with TiCl_4 in a high temperature plasma environment to produce Al-TiAl₃ composites. Plasma atomization was studied in order to produce very fine molten particles for the reaction since their sizes have an important impact on the reaction yield.

This chapter also describes experimental procedures used to measure the Ti, and Cl content of the product, particle size distribution, porosity level, microstructural features, and mechanical properties.

4.2. Plasma Torch

A non-transferred reverse-polarity (R-P) plasma torch was used throughout this study. The conceptual schematic of this torch is shown in **Figure 4.1**.^{*} The electrodes of this torch are tubular with 8 mm I.D.. The plasma forming gas introduced between the electrodes is swirled tangentially using a vortex generator. The R-P plasma torch is a high temperature and enthalpy heater. The torch converts electricity into heat via the Joule heating of a small flow of gas that has been energized to the plasma state. The arc column in the plasma state is stabilized within the core of a rotating gas. The Joule-heated arc column of the plasma torch

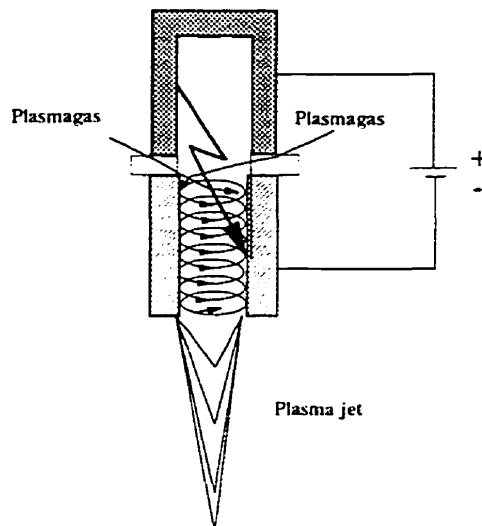


Figure 4.1 Schematic of the non-transfer D.C. plasma torch used for plasma atomization and reactive plasma spraying.

readily heats up the rotating gas that surrounds the column to high temperatures ranging from 2000 to 5000°C.

^{*} RPT1 torch made by PERMA, a division of PyroGenesis Inc.

4.3. $TiCl_4$ Injection System

$TiCl_4$ is liquid at room temperature and boils at $140^\circ C$ at atmospheric pressure. [78] $TiCl_4$ was vaporized in a hot-box kept at a constant temperature of $350^\circ C$. This facilitates its introduction into the plasma jet region and prevents quenching of the plasma to some extent. In addition, better mixing with the plasma jet is achieved. The $TiCl_4$ vapor temperature after exiting the hot-box and before entering the plasma jet was measured as $200^\circ C$. $TiCl_4$ liquid was transported using peristaltic pumps while its vapor was carried with an Ar carrier gas. The Ar carrier gas was also passed through the hot-box and heated to $200^\circ C$. The schematic set-up of the $TiCl_4$ injection system is show in **Figure 4.2**.

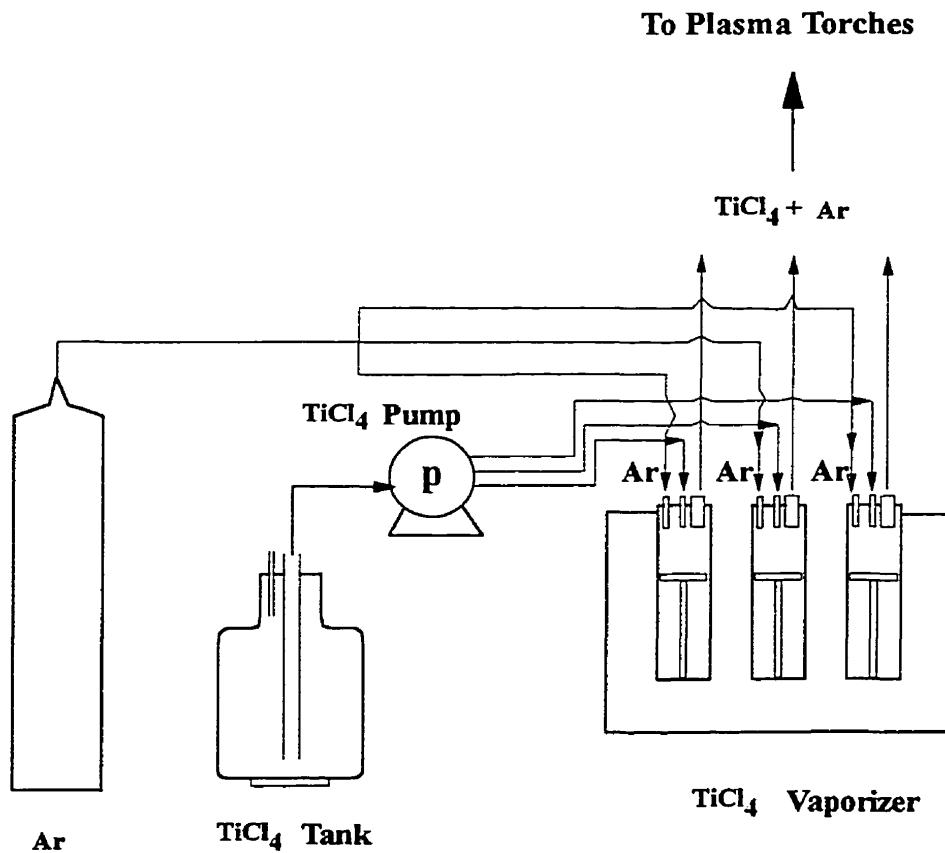


Figure 4.2 Schematic of the $TiCl_4$ injection system.

The mixture of Ar and TiCl_4 was injected into the graphite nozzles and plasma jets using molybdenum tubes, as shown in **Figure 4.3**.

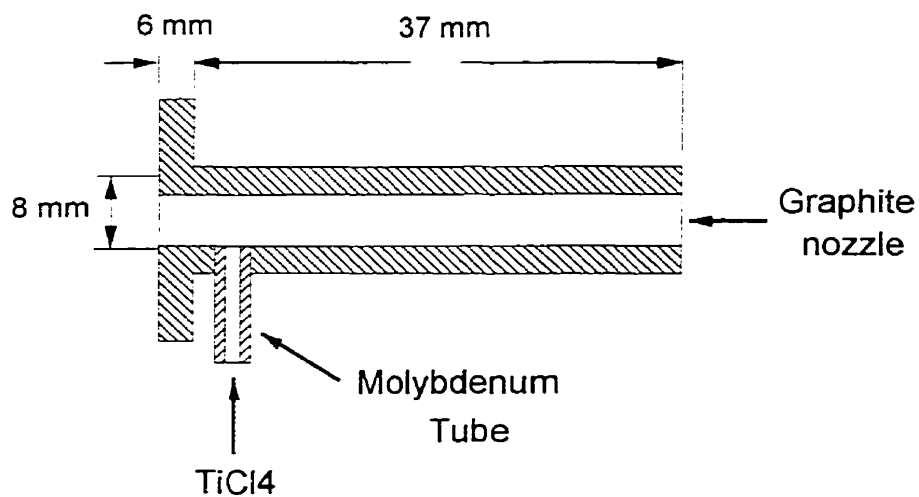


Figure 4.3 Graphite nozzle used to inject TiCl_4 into the plasma jet stream.

4.4. Reactive Plasma Spraying Using a Single Plasma System

The Al-TiAl₃ composite was produced using a D.C. plasma torch, a cylindrical reactor, and a graphite substrate. **Figure 4.4** shows the experimental set-up. The reactants, Al powder and TiCl₄ vapor, were fed through two concentric tubes into the plasma region at the rate of 10 g/min and 20 ml/min, respectively.

The Al powder was injected to the plasma region using a Miller powder feeder Model 1251. The liquid TiCl₄ was the source of Ti. The liquid TiCl₄ was pumped using a peristaltic pump through stainless steel tubing to an evaporator set at 200°C. The injection rate of the TiCl₄ was controlled by the pump. The plasma forming gas was pure argon, and the products were collected as deposits from the graphite substrate and graphite sleeve around the plasma torch.

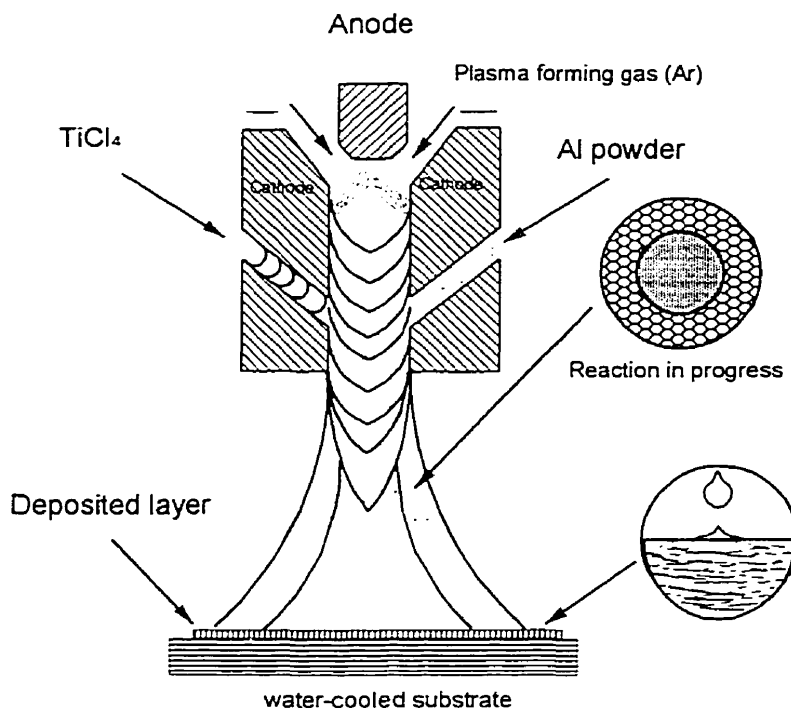


Figure 4.4 Schematic of reactive plasma spraying using a single plasma torch and Al powder as raw material.

4.5. Reactive Plasma Spraying Using a Triple Plasma System

TiCl₄ was the source of Ti, whereas Al wires with two different gauges of 1/16" and 3/32" diameters were used as the Al source. The raw materials were injected into the focal point where multiple plasma jets converged, as shown in **Figure 4.5**. Liquid TiCl₄ was first evaporated and then injected into the plasma region. Experiments were performed with a constant torch power of 33 kW and 110 SLM of argon per torch. The reaction products were collected on the surface of a water-cooled substrate and neutralized with water before collection. For each experiment, a precise sequence of steps was followed: (a) obtain a vacuum level of 0.1 mbar inside the reactor, (b) purge several times with argon,

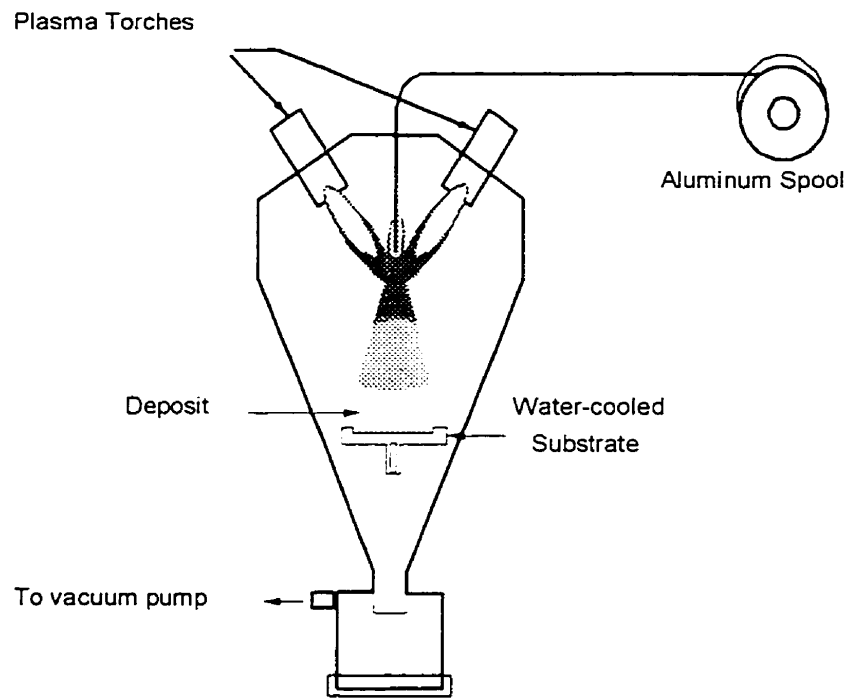


Figure 4.5 Schematic of the reactive plasma spraying.

(c) ignite all three plasma torches, (d) feed Al and TiCl₄, (e) spray-form the Al-Ti alloys, and (f) neutralize and recover the sample. The effect of Al/ TiCl₄ molar ratio was varied to verify the Nagamori model predictions[79]. The products were evaluated based on: (a) Ti and Cl content, (b) distribution of Ti, and (c) porosity.

4.6. Production of Al-TiAl₃ Composites through other Processes

Al-TiAl₃ composites are not commercially available. One of the objectives of this study was to synthesize this material through a variety of metallurgical processes in order to provide reference material for comparison with the reactively synthesized composites. The understanding of the Al-Ti system, using other processes, could also provide a better understanding of the reactive system. Therefore, apart from plasma spraying, casting and powder metallurgy techniques were investigated as possible methods for producing Al-TiAl₃ composites.

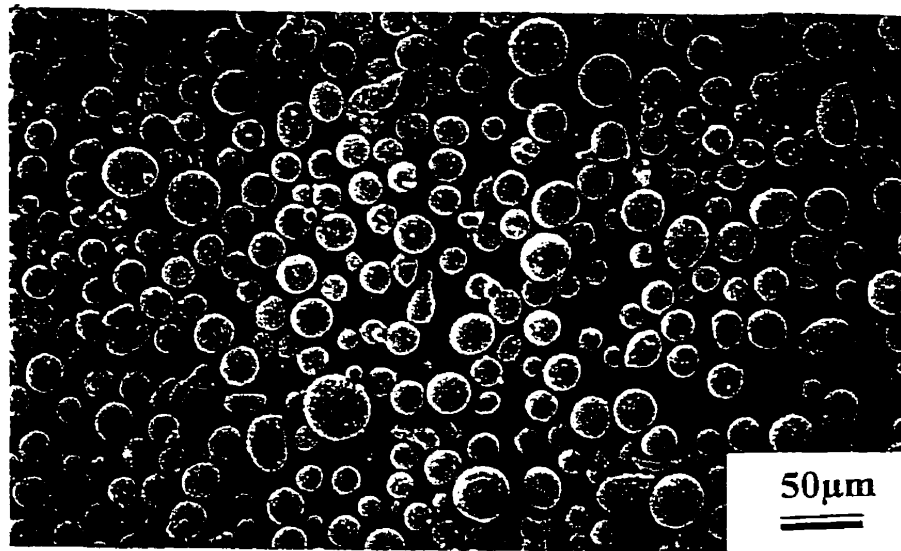
4.7. Plasma Spraying

4.7.1 Starting Materials

A premixture of elemental powders of Al, with an average particle size of 40 μm, and Ti, and an average particle size of 60 μm, was supplied as a spray material for the low pressure reactive plasma spraying of Al-Ti composites with an argon and hydrogen mixed plasma forming gas. Two premixtures of Al and Ti were prepared containing 5 and 15 wt% of Ti. The micrographs of the starting materials are presented in **Figure 4.6**.

4.7.2. Experimental Design

A fractional factorial design of experiments was used to evaluate the effects of the plasma reactor variables on the final microstructure[80].



(a)



(b)

Figure 4.6 Scanning electron micrographs of the starting materials (a) Al powder, (b) Ti powder.

The set-up of the experiments and their responses based on thickness of the coatings are listed in Table 4.1. The plasma forming gas was kept constant at a mixture of 100 LPM argon and 10 LPM hydrogen during all experiments. The powder feed rate was chosen to be 2.5 g/min. Torch current was kept at 200 Amps. Both stainless steel (4x4 cm) and Ti substrates (5x5cm) were used for this series of experiments.

Table 4.1 Experimental set-up and their responses after 5 minutes of spraying.

Run order	A Chamber pressure (mbar)	B Spray distance (cm)	C Substrate material	D Ti content (%)	R ₁ Thickness (μm)
1	60	40	SS	15	75
2	40	55	SS	15	50
3	40	40	Ti	15	10
4	40	40	SS	5	90
5	60	55	SS	5	460
6	60	40	Ti	5	97
7	60	55	Ti	15	100
8	40	55	Ti	5	0

The other factors that affect the process were kept constant and are listed below:

Plasma forming gas: argon/hydrogen = 100/10 (LPM)

Powder feed rate: 2.5 g/min (2 rpm, 15 LPM of argon as carrier gas)

Current: 190-200 Amps

Voltage: 70-80 Volts

Spray distance: 40-55 cm

Powder injection time: 5 min

Substrate: stainless steel or Ti plates

4.8. Casting

Pure Al* was melted in an induction furnace. After melting (30 min), the melt was superheated to 800°C. The Ti powder, as reported earlier in this section, was then added to the melt to provide the desired composition. The melts were then heated to above the liquidus temperatures according to the Al-Ti phase diagram (800-1250°C), were well stirred by the induced magnetic flow and cast into a water cooled copper mould.

4.9. Powder Metallurgy

Three compositions of Al at 5, 10 and 15 wt.% Ti were prepared. The powder mixtures comprising of 200 g of Al and Ti powders, were ball milled in isopropyl alcohol for 30 minutes in a plastic container of 4 L capacity to prevent oxidation of the elemental powder and also to breakup their surface oxide layer. The ratio of liquid to powder was 2 to 1 by weight. Si₃N₄ media having a diameter of 4mm was used for milling. The proportion of media to that of powder was 2 to 1 by weight. The slurry was then passed through a 212 µm sieve to separate it from the media and dried in an air oven heated to 120°C. Green samples were formed by die-pressing approximately 7g of the powder mixture at a pressure of about 5MPa, forming pellets of 10 mm in diameter and 20 mm in height. The pellets were then isostatically pressed at 300 MPa.

The green samples were sintered at three temperatures (600, 700 and 1000°C) in a vacuum furnace operating at 10⁻² mbar for 30 minutes. The samples were then furnace cooled to room temperature.

The powder of the composite material and the spray deposited layer were then characterized

* Grade 1060, 99.9 % Alcan

using optical microscopy, scanning electron microscopy (SEM), X-Ray diffraction (XRD), thermogravimetry analysis (TGA), and energy dispersive spectroscopy (EDS).

4.10. Thermal Analysis

The effect of temperature on thermal dissociation of residual chlorine compounds detected in the composite material was studied using TGA*. The samples 1 cm³ in volume were heated to 1000°C in helium and weight changes were simultaneously registered as a function of time and temperature. The heating rate used was 10°C/min. An isothermal soak was also given to the sample at 120°C for 20 minutes to remove absorbed moisture.

The reaction between Al and Ti powders was studied using differential thermal analysis (DTA). The main objective of the DTA was to determine the substrate temperature for vacuum plasma spraying using elemental powders of Al and Ti. Five grams premixtures of Al containing 5, 10 and 15 wt.% Ti were prepared and heated to 1500°C in helium. The flow rate of the helium was 100 ml/min and the heating rate used was 10°C/min.

4.11. Plasma Atomization

The experimental set-up used in this study, was very similar to that explained in section five of this chapter, and consisted of a water cooled chamber, a metal feeding mechanism, and three plasma generating systems. Three different chambers were used. The first chamber was smaller (60 cm I.D. x 75 cm high) and was used for preliminary studies. The second chamber was larger (150 cm I.D. x 200 cm high) and was used for the production of powders. The third chamber, the largest (140 cm I.D. x 435 cm high), was used to study particle size distribution during the atomization process. The metal feeding mechanism consisted of either

*951 Thermogravimetry analyzer, Dupont Instruments.

a resistive heating furnace, used to melt the metal and feed the molten stream into the chamber through a nozzle using a graphite plug for flow control, or a wire feeder. The plasma jets were generated by three non-transferred D.C. guns capable of operating in the power range of 20 to 40 kW. The three jets converged into an apex where the metal was introduced. A schematic representation of the plasma atomization equipment is shown in **Figure 4.7**.

For the plasma atomization experiments, each plasma torch was operated at 30 kW, with argon as the plasma forming gas (flow rates of 100 L/min). Graphite and tungsten nozzles were used in front of the plasma torches to accelerate the plasma jet and to retard the entrainment of surrounding gases into the plasma jet. The entrainment of the cold gases cools and reduces the speed of the plasma jet, thus limiting its thermal processing and atomization capabilities. Both straight and convergent/divergent nozzle designs were tested for this purpose. **Figure 4.8** shows the convergent/divergent nozzle.

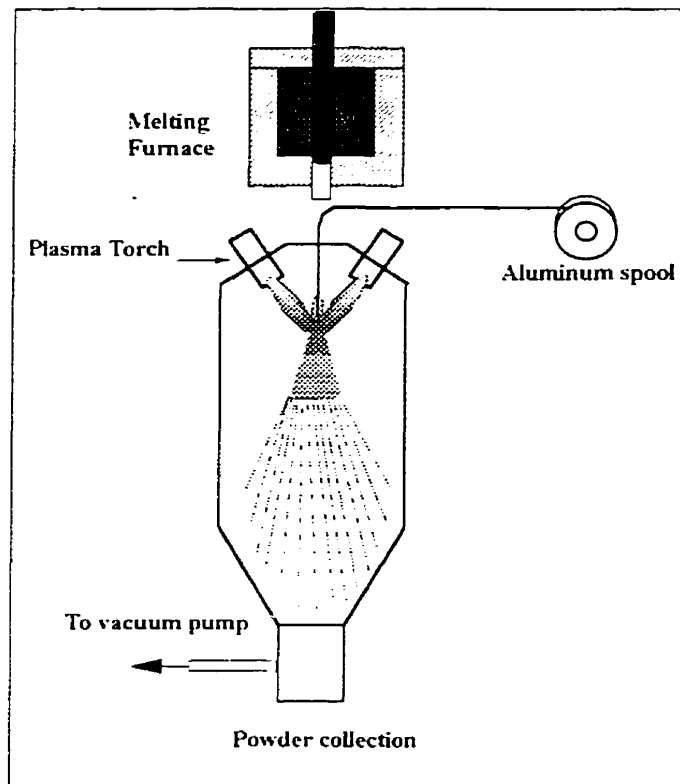


Figure 4.7 Plasma atomization reactor used for powder production study.

The experimental program was divided into two steps: (a) a feasibility and optimization study in a small reactor; and (b) a scaled-up study in a larger reactor. The initial feasibility and optimization study for the production of powders took place in a reactor with an

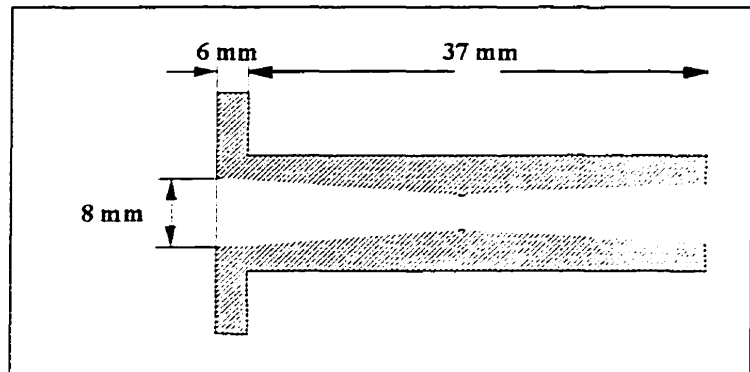


Figure 4.8 Schematic of the convergent/divergent nozzle used for plasma atomization.

inside diameter of 1.5 m and a height of 2 m. The production of large quantities of powder required a larger reactor with an inside diameter of 1.4 m and a height of 4.35 m.

The raw materials investigated included molten metal and metal wires. All of the molten metal feed experiments were performed with Al. Al was melted and super-heated in a resistance furnace and poured into the atomization region by unplugging the graphite nozzle. The feed rate of the molten Al was controlled by varying the feed nozzle diameter. Two different wire sizes (1/16" and 3/32") were used in order to understand the effect of wire size on the average particle size and distribution of the atomized products. The plasma atomization process was tested for the production of Ti, Ni, Cu, Cu-Ni, and Al powders.

4.12. Particle Size Distribution

In order to study the particle size distribution in the central and peripheral regions of the atomization plume, a set of cylindrical containers were located below the atomizer. Fifteen containers of two different diameters of (38.1 and 44.5 mm) were used to cover the majority of the area beneath the atomizer. The plasma atomizer was run for five minutes with argon as the plasma forming gas at a total power of 90 kW. The powder collected in each container was tested for mass and particle size distribution. Powder particles collected from individual

containers were subjected to sieve particle size analysis.

4.13. Hot Rolling

The as-sprayed deposits contained 5 to 10 vol.% porosity. Hot rolling was used for consolidation of these samples. Samples for rolling were ground to a rectangular shape with a cross-section of 1cm x 0.5 cm. A rolling machine was arranged close to a furnace and the rolling temperature and reduction varied in order to optimize the rolling conditions of the Al-TiAl₃ composites.

4.14. Chemical Analyses

The chemical composition of the deposits was determined using atomic absorption spectroscopy and metallography. Image analysis was used only to determine the Ti content of the products.

4.15. Atomic Absorption (AA)

Three standard solutions with known Ti concentration of 5, 10, 25% were prepared and injected into the AA instrument.* A calibration curve was constructed for the Ti concentration as a function of the readings obtained from these tests. One-tenth of a gram of the unknown samples was dissolved in a mixture of acids diluted to volume of 50 mL and measured. The readings from the instrument for these measurements were compared with the calibration curve and Ti contents were obtained. Each samples was tested three times and the average value was reported as the Ti content.

* Perkin Elmer

4.16. Microstructural Sample Preparation

Each sample was cut and mounted for microstructural examination. It was then ground using successively finer silicon carbide grit discs down to 600 grit and polished with 6 μm , 1 μm , and an alumina suspension down to 0.05 μm . The polished specimens were then carbon coated for Energy Dispersive Spectroscopy EDS analysis. Backscatter and secondary images were taken using an Amray 1610 scanning electron microscope (SEM). The semi-qualitative chemical analysis was obtained using a Link EDS system attached to this microscope.

4.17. Microstructural Analysis

The TiAl_3 phase content of the deposits were measured using an optical microscope and a computer image analysis software.* The TiAl_3 phase appeared as a bright phase in a grey matrix of Al. Using the image analyzer, the volume fraction of the TiAl_3 phase was calculated from the ratio of the measured area to the total surface area of the designated field as:

$$\text{TiAl}_3 \text{ Vol. \%} = \frac{\text{TiAl}_3 \text{ Area}}{\text{Total Sample Surface Area}} \times 100 \quad (4.1)$$

and the Ti wt.% of the composite was measured using the Al-Ti phase diagram and respective densities (2.7 g/cm^3 for Al and 3.4 g/cm^3 for TiAl_3) of the two phases.

* Image-Pro Plus from Media Cybernetics

CHAPTER 5

PLASMA

ATOMIZATION

5.1 INTRODUCTION

In the reactive plasma spraying of materials using a triple plasma system, there are at least seven chemical and physical events which take place. Some of these are: (a) melting and superheating, or boiling of precursors; (b) atomization of the molten materials into very fine particles; (c) chemical reactions; (d) formation of new compounds; (e) acceleration of the reaction products toward a substrate; (f) impingement and flattening of the molten or semi-molten products onto the surface of the substrate; and (g) solidification through splat quenching.

Almost all of these events are either directly or indirectly affected by the atomization process. It was realized early in the study that the atomization played a key role in the reactive plasma process and, thus, required further analysis. In addition, it was mentioned in § 2.9 that the Ti

content of the Al-TiAl₃ composites is a function of the molten Al particle temperature at the time of its reaction with the TiCl₄. The size and temperature of the Al particles are controlled by the plasma atomization process which takes place prior to reaction. Therefore, an understanding of plasma atomization was deemed necessary in order to control the process for the production of molten particles with the desired physical and chemical characteristics.

The desired characteristics for molten Al particles for a reaction with TiCl₄ are:

- (a) very fine particle size of <100 μm;
- (b) narrow particle size distribution; and
- (c) a liquid temperature higher than melting point of TiAl₃.

Without an understanding of the plasma atomization process, it is almost impossible to produce suitable conditions where the molten Al droplets would be processed to attain the above characteristics.

Plasma atomization is similar to gas atomization, however, there are two distinct differences between these two processes. In gas atomization, the feed metal is in the liquid state, whereas in plasma atomization (as used for reactive plasma atomization), it is in the solid state. In plasma atomization, extremely hot plasma jets are used to break up the feed materials which results in a superheated melt and a slower solidification rate. In contrast, in gas atomization, superheating of the melt during atomization is not possible unless the gas temperature is higher than the melt temperature.

In the following paragraphs, various powder production techniques are reviewed with a emphasis on atomization since it most resembles the plasma atomization processes.

5.2 LITERATURE REVIEW

5.2.1 Powder Production

Metal powders are produced commercially by one of four processes. These are: chemical, electrolytic, mechanical, and atomization[81],[82]. Among these processes, atomization has become the dominant mode of powder fabrication. This can be explained by: (a) the high powder production rate, as metal feed rates up to 400 kg/min are used[83]; (b) the possibility of controlling the size, size distribution, shape, and surface morphology of the powder particles; and (c) a high degree of alloying flexibility. In addition, atomization is frequently a captive process, constituting the only viable fabrication process for highly alloyed specialty powders.

5.2.1.1 Atomization

Atomization is the breakup of a liquid into fine droplets. Thus, any material in the molten state can be atomized. The breakup of a liquid stream into discrete particles can be caused by impingement with water or gas, often termed two-fluid atomization. Despite the method of fabrication, the major event in the production of metal or alloy in a finely divided form is the generation of new surfaces. If a cubic meter of the material is broken into spherical particles measuring $1\mu\text{m}$ in diameter, the total number of particles is approximately 2×10^{18} , with a total surface area of $6 \times 10^6 \text{ m}^2$. If the surface energy is taken as 1500 J/m^2 , then the energy required to form this amount of surface is 9 MJ! As a second example, a 1 gram sample of iron will generate 2.4×10^{11} spherical monosize particles with a diameter of $1\mu\text{m}$, and the total surface energy associated with the iron powder is about 1J.

The bulk of atomized powder is made by the two-fluid method. In this method, the liquid metal stream is atomized by the impact of a stream of another fluid which emerges from a nozzle. The atomizing fluid may be either gas or liquid (usually water). Where the atomizing

stream is gaseous, the process is called external pneumatic atomization or simply gas atomization.

More than 60% by weight of all the powders produced in North America are manufactured by atomization. It is estimated that worldwide, atomization capacity is approaching 10^6 metric tons per year[84].

5.2.1.1.1 Gas Atomization

In most versions of gas atomization, the liquid metal flows by gravity from a tundish, below the tundish orifice, the liquid metal stream is impinged by a gas jet or several jets. The primary stage of atomization occurs at the apex of the jet intersection. Here, the molten metal is disintegrated, accelerated, and eventually cooled and solidified, to form very small powder particles. Two typical gas atomization processes are shown in **Figure 5.1**.

Air is often used in gas atomization, although it promotes oxidation of the powder particles. When the oxidation of powder is a concern, inert gases such as argon and helium are used. Powders produced by gas atomization are spherical, unlike the water atomized powders that are irregularly shaped. General opinion has it that highly irregular powders have the best compaction behaviour therefore, water atomized powders are desirable. However, this has to be balanced with the caution that the gas atomized powders are usually less oxidized. In production, the metal flow rates for gas atomization are about 1-70 kg/min, however, a 120 kg/min metal flow rate has also been reported. The size of the molten metal stream measures 2 to 15 mm in diameter. In conventional commercial gas atomization, gas pressures are between 0.5 and 9 MPa; with corresponding gas flow rates between 0.02 and 0.24 m³/s. The gas velocities depend on the nozzle design and range from 20 m/s to supersonic velocities[85].

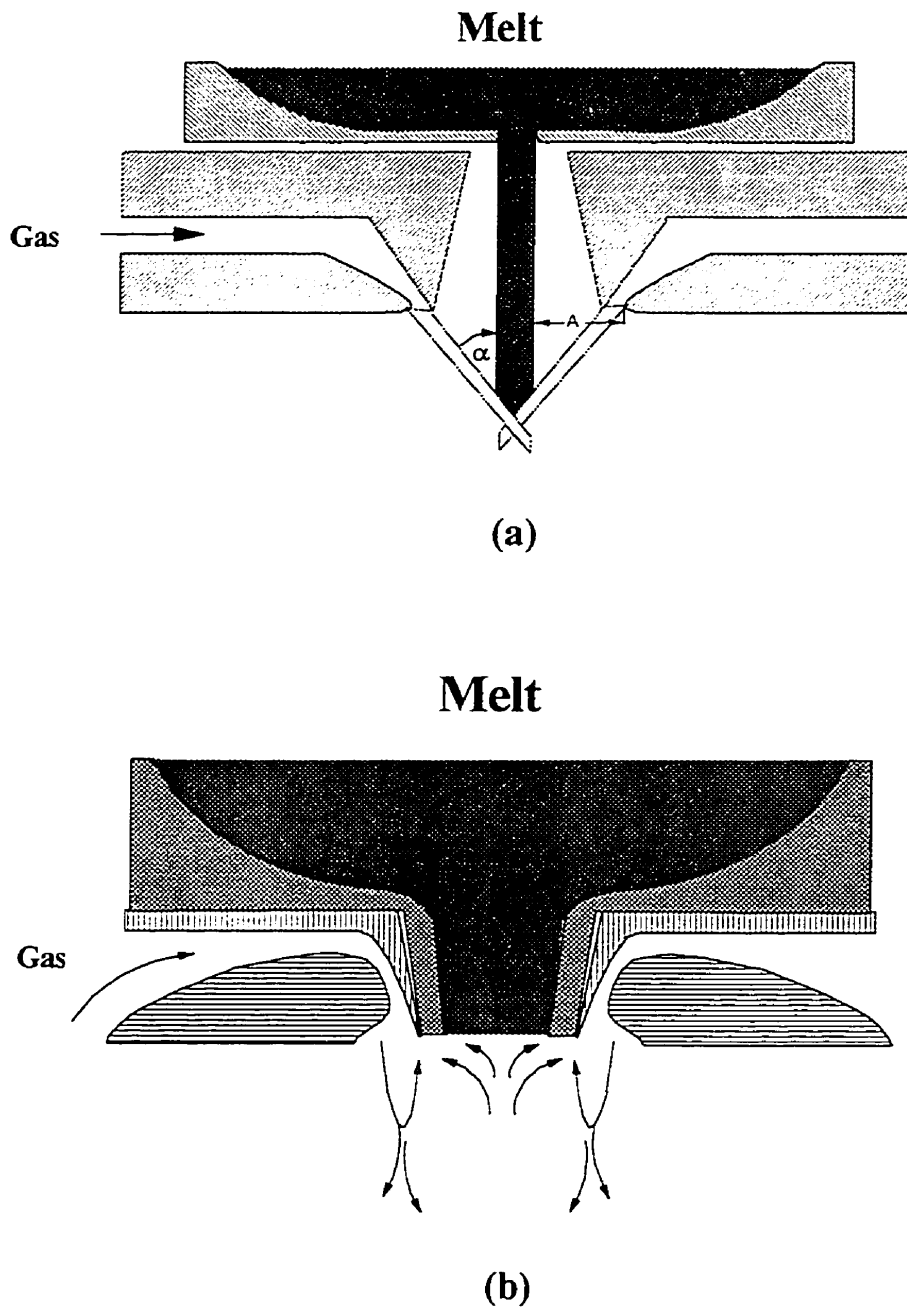


Figure 5.1 Gas atomization designs (a) free fall and (b) confined.

The literature contains a large quantity of data on atomization. Most of these data are gathered in empirical equations. This is most probably due to the dependence of the powder size and distribution on the atomization process, and more specifically on the nozzle design. Thompson[86] reported that for Al powder the average powder particle size decreased when the liquid metal flow rate, melt superheat, and the jet pressure increased. Joyce[87] reported that a minimum of 110 K melt superheat is required for successful atomization. It also was reported that by increasing the apex angle the average particle size is decreased. Rao [88] found that by increasing the jet distance, more irregular particle shapes are produced.

Small and Bruce [89] observed that the width of the particle size distribution depends on the atomizing fluid used and the shape of the powder particles is independent of the atomizing pressure level. In addition, it was concluded that the shape is also independent of superheat. They also developed the following equation:

$$d_m = \ln(P/c)^n \quad (5.1)$$

where:

d_m = mean particle diameter, P = atomizing pressure, and n, c = constants.

Lubanska[90] modelled the gas atomization of liquid iron using a multiple jet configuration. It was predicted that the average particle size varies inversely with the jet fluid velocity. Goldaev *et al.*[91] used a jet engine to atomize liquid metals at a supersonic velocity and claimed improvement in particle size as compared with subsonic velocity.

Klar and Shafer[92] reported that the confined nozzle is more efficient than the free-fall nozzle but it is more difficult to use. Their results on copper show that as the gas flow is increased, the particle size and size distribution are reduced. It was also found that the jet angle controls the patternization. If the jet angle increased, a more even spread of droplets is obtained.

5.2.1.2 Droplet Formation Mechanisms

Droplet formation during atomization is a complicated set of events. Most of the reported data on particle shape, size, and size distribution is empirical in character, and refers to specific atomizing systems. Therefore, the information can act only as a general guide.

The proposed particle formation mechanism for gas atomization starting with a liquid stream involves: (a) initiation of a sinuous wave that rapidly increases in amplitude; (b) detachment of the wave from the bulk of the liquid to produce a ligament whose dimensions depend on the wavelength at disintegration; and (c) break up of the ligament into spherical droplets, as shown in **Figure 5.2**. Rayleigh[93] presented an analysis of the break up of a stream of liquid

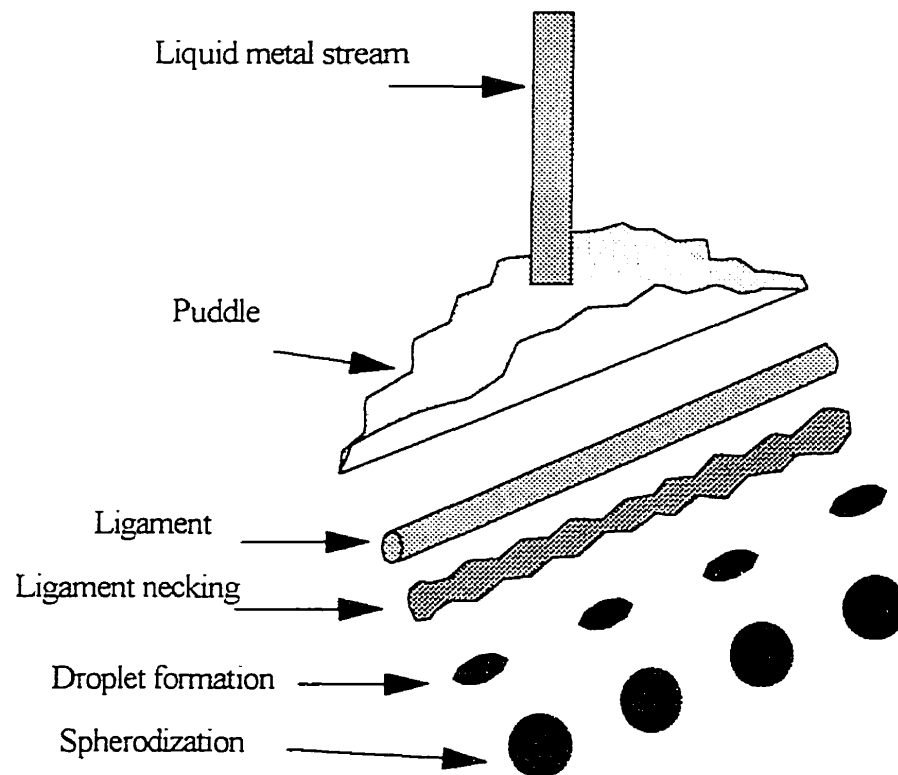


Figure 5.2 Particle formation mechanism.

into droplets. He considered that the continuous stream first breaks into ligaments which then break into droplets. He showed that the droplet diameter is equal to 1.88 times the ligament diameter. Dombrowski and Hooper[94] reported that the ligament diameter depends on the initial liquid sheet thickness (s) and its wavelength (λ) as:

$$d_L = 3(\lambda s)^{1/2} \quad (5.2)$$

Squire[95] also found that:

$$\lambda = \frac{3\pi\gamma}{\rho V_m^2} \quad (5.3)$$

where λ , V_m , and γ are the sheet wavelength, liquid velocity (at the break up stage), and surface tension of the liquid, respectively. By combining equations 5.2 and 5.3, the ligament diameter can be obtained as:

$$d = \frac{\text{constant}}{V_m} (\gamma s)^{1/2} \quad (5.4)$$

Naida[96] studied the stability of a liquid metal drop in an accelerating field and derived the following equation:

$$\tau_{def} = 1.65 \frac{D_n}{v_g - v_p} \left(\frac{\rho}{\rho_g} \right)^{1/2} \quad (5.5)$$

where:

τ_{def} = time elapsed to reach critical deformation (s)

ρ and ρ_g = densities of the liquid metal and gas, respectively (kgm^{-3})

D_n = nominal drop diameter (m)

v_p and v_g = drop and gas velocities, respectively (m/s).

In this model, the particle disintegrates if the critical deformation time τ_{def} , is less than the time needed for the liquid metal droplet to reach a velocity at which it is dynamically stable.

Another mechanism called "twinning" was proposed by Silaev[97]. In this mechanism, the droplet splits into two parts because of the interactions between the external drag, surface tension, and internal viscous effects. Putimtsev[98] confirmed the twinning mechanism by obtaining a photograph of the actual process. He showed that ligament formation is the first stage of atomization. The second stage of atomization can occur through an explosive shock mechanism at a high gas pressure or twinning mechanism at a low gas pressure.

Hinze[99] identified three different mechanisms of splitting: (a) *lenticular* occurs when the particle flattens, then opens into a bag, and finally bursts into smaller particles; (b) *cigar-shaped* occurs by particle elongation in one direction followed by splitting; and (c) *bulgy* occurs in certain flow fields when local deformations protrude into the atomizing fluid and shear off to form new particles.

Lubanska[90] studied the atomization of iron, steel, and tin in a multiple jet system using nitrogen as the atomizing gas. He derived an equation for particle mass median as:

$$\frac{d_m}{d_t} = K_1 \left[\left(\frac{v_m}{v_g We} \right) \left(1 + \frac{M}{A} \right) \right]^{\frac{1}{2}} \quad (5.6)$$

where: d_m = mass median diameter of the atomized powder (m)

d_t = liquid metal stream diameter (m),

ν = kinematic viscosity (m^2/s),

We = Weber number corresponding to $v_g \rho d_t / \sigma$,

M/A = mass flow rate of metal to gas ratio,

K_1 , = constant between 40 and 50, and V = gas velocity at the apex (m/s).

5.2.1.3 Kinetics of Droplet Solidification and Spheroidization

The final shape of a liquid metal droplet in gas atomization is influenced by the relative magnitudes of the time required for solidification and the time required for surface tension forces to spheroidize the droplet. Without other effects (e.g., oxide films and modification of surface tension by surface active additions), the spheroidization time of the liquid droplet is small compared with its solidification time, then the powder particles spheroidize. In the model developed by Nichiporenko and Naida[100] for the solidification time in gas atomization, it was assumed that the molten droplets did not undercool, that the relative velocity between the gas phase and the particle was constant and that only convective heat transfer was important. This model was modified by See and Johnson [101] to include the time necessary for the particle to lose its latent heat of fusion; with this modification, the total solidification time t_{sol} (in seconds) is given by:

$$t_{sol} = \frac{d_m \rho}{6h_c} \left[(C_p)_m \ln\left(\frac{T_i - T_g}{T_m - T_g}\right) + \left(\frac{\Delta H_m}{T_m - T_g}\right) \right] \quad (5.7)$$

- where: d_m = mass median particle diameter(m),
 h_c = convective heat transfer coefficient of the gas (W/(m² K)),
 ρ_m = density of the liquid metal (kg/m³),
 $(C_p)_m$ = heat capacity of the liquid metal (J/(kg K)),
 T_i = initial temperature of the particle (K),
 T_g = gas temperature (K),
 T_m = melting point of the metal; liquidus temperature for alloys (K), and
 ΔH_m = latent heat of fusion of the metal (J/kg).

The value of h_c is given by:

$$h_c = \frac{k_g}{d_m} (2.0 + 0.6Re^{0.5}Pr^{0.33}) \quad (5.8)$$

where: k_g = thermal conductivity of the gas (W/m K), Re = Reynolds number of the particle, and Pr = Prandtl number for the gas.

Under the influence of surface tension forces alone, the time for spheroidization t_{sph} is given by [100]:

$$t_{sph} = \frac{3}{4} \left(\frac{\pi^2 \mu_m}{V \sigma_m} \right) (R^4 - r^4) \quad (5.9)$$

where: μ_m = dynamic viscosity of the liquid metal (Pa.s), V = particle volume (m^3),
 σ_m = surface tension of the liquid metal (N/m),
 r = cylinder radius before transformation to spherical droplets (m), and
 R = particle radius after transformation to spherical droplets (m).

A detailed model and more general model which can be used to estimate the time for spheroidization of a droplet has been given by Rao[88] and Rao and Tallmadge[102], respectively. Their predicted spheroidization times are not significantly different than those described above.

In the above discussion, the focal point was on the break up of a *molten stream*, as it is the standard terminology for atomization. *Solid shapes* can also be used as the feedstock for the atomization process. In atomization processes involving solid feedstock, the time between the melting and the atomization process is reduced by the application of a high heat transfer mechanism such as an electric arc discharge or high velocity and extremely hot combustion

or plasma jets.

The use of an electric arc for atomization has been patented by Nuclear Metals, under the trade mark of Rotating Electrode Process (REP) for the production of reactive metal powders. In this process, the electric arc is struck between a consumable rotating rod and a stationary refractory metal electrode. Due to the high energy associated with the electric arc discharge, the rotating electrode (feedstock) experiences surface melting. Small droplets form on the surface of the electrode and detach from the rod due to the centrifugal force. The detached droplets then freeze in flight, forming spherical powder particles.

The other process uses two consumable electrodes. An electric arc is struck between the two electrodes which are continuously fed at an angle into a gas jet. As a result, molten droplets form at the tip of the electrodes and are simultaneously blown away and atomized by the gas jet flowing between the electrodes. The atomized particles accelerate and travel in the direction of the gas jet until impinging onto a substrate and flattening forming a coating. This process has been used extensively for coating and has not found any commercial application in powder production.

High velocity jets have also been used for melting, atomizing and coating. Wire-feed flame sprays used with either low velocity or high velocity combustion flames have been used for this purpose. The rapid convective heat transfer resulting from the hot and high velocity jets rapidly melts the tip of the wire, therefore, molten droplets are formed and are detached, atomized, accelerated and splat-formed on the surface of the substrate forming coatings. There is no commercial powder production process using this technique. However, it is widely used for the application of coatings.

5.2.2 Wire Atomization

A large number of papers are available which examine the behaviour of particle-plasma and HVOF¹ jets. Most of these data deal with powder-feed devices. Very little data exists on wire-fed systems. Particle velocimetry data was presented by Kowalsky et al. for the single wire arc process, but no information was reported on droplet sizes[103]. Much more data are available on liquid metal droplet formation studied for various spray-casting or spray-forming processes. The ratio of metal to gas mass flowrate is typically much greater in the liquid-fed spray forming process than solid-fed (such as wire) spray processes. Despite these differences, expecting some similarity in the droplet-forming mechanisms of the two processes is reasonable. Gas velocities in the Ospray process are much lower than those typically encountered in thermal spray processes, resulting in much larger-sized particles. For example, Bewlay and Cantor reported particle sizes in the hundreds of microns range for an atomized lead-tin alloy[104]. Higher jet velocities are present in the de Laval spray forming nozzle, producing atomizing conditions similar to those of the HVOF processes[105].

Pilch and Erdman[106] show that droplet breakup in an atomizing gas flow depends on the initial Weber number of the system. The size of the largest droplets (d_{\max}) can be predicted using the critical Weber number (We_{crit}) by the following equation:

$$d_{\max} = \frac{\sigma_p We_{crit}}{\rho_g (v_g - v_p)^2} \quad (5.10)$$

where ρ_g and v_g are the density and velocity of the gas, and v_p and σ_p are the velocity and the surface tension of the droplet, respectively. It can be seen that the maximum particle size is decreased by decreasing the surface tension of the metal and critical We_c number, by increasing the gas density and increasing the difference between the gas and the particle velocities.

¹High Velocity Oxygen Fuel

5.2.3 Effect of Particle Size on Particle Velocity

A simple calculation involving the size dependence on particle velocity predicts a stronger effect than the previous equation. For a spherical particle of diameter, d_p , and density, ρ_p , moving at a velocity, v_p in a gas stream of velocity, v_g , and density ρ_g , Newton's second law can be expressed as:

$$\frac{\rho_p \pi d_p^3}{6} \frac{dv_p}{dt} = \frac{\pi d_p^2}{4} c \rho_g \frac{(v_g - v_p)^2}{2} \quad (5.11)$$

where the drag coefficient (c) is a constant. If one assumes that $v_g \gg v_p$ and the chain rule is used to replace dv/dt with vdv/dx ,

$$\frac{\rho_p \pi d_p^3}{6} \frac{vdv_p}{dx} = \frac{\pi d_p^2}{4} c \rho_g \frac{v_g^2}{2} \quad (5.12)$$

then an integrable differential equation is obtained:

$$\frac{\rho_p \pi d_p^3}{6} v dv_p = \frac{\pi d_p^2}{4} c \rho_g \frac{v_g^2}{2} dx \quad (5.13)$$

using the condition that $v_p = 0$ at $x=0$, then v_p can be calculated as:

$$v_p = \sqrt{\frac{3c\Delta x \rho_g v_g^2}{2\rho_p d_p}} \quad (5.14)$$

where Δx is the distance travelled by the particle. If particles of various sizes are exposed to the same aerodynamic driving force, $\rho_g v_g^2$, then Equation (5.14) predicts that the velocity of the particle will vary inversely as the square root of its size. Thus, a 50 μm particle should travel twice as fast as a 200 μm particle. If the changes in drag coefficient with particle size are taken into account, the predicted velocity is an even stronger function of particle size than Equation (5.14).

5.2.4 The Effect of Wire Feeding Rate on Atomization Mechanism

Wire melting and droplet formation during the plasma atomization process play an important role in determining the microstructure of the reactively sprayed deposit. In other words, the plasma atomization is the heart of reactive plasma atomization. Finely atomized sprays will yield higher temperature than a coarse spray. The higher particle temperature besides the higher reaction surface increases the yield of the reaction. Furthermore, finely atomized sprays will yield higher velocities and, as a rule, can be expected to produce smoother, denser coatings. Oxide content, bond strength, wear resistance, and many other coating properties will also be affected by the atomized particle size and velocity. Wire melting rate is also the key factor in the economy of the reactive plasma atomization process. The following presents data from a series of experiments aimed at improving our understanding of wire melting and droplet breakup and identifies some factors affecting them.

The ratio of wire feeding rate to the plasma power determines the atomization mechanism in the PA process. The low wire feeding rate to power ratio results in early melting of wire before reaching the apex where the highest kinetic energy is available for atomization. As a result, large droplets form at the tip of the wire and gradually grow until the gravitational force is large enough to overcome the surface tension which holds the droplets to the wire (if the venturi effect and turbulent flow in this region are ignored). Therefore, the density and surface tension of the metal at its melting point controls the drop size at the time of detachment. Consequently, this affects the final average size of the particles resulting from the atomization of the drop. Therefore, if m is the mass of the drop attached to a vertical wire of diameter d , the equilibration of gravitational force and surface tension forces can be written as:

$$mg = \gamma \pi d \quad (5.15)$$

where γ is the surface tension of the molten drop and g is the gravitational acceleration. If the

size of the drop exceeds a critical value, separation of the droplet occurs. Assuming a spherical shape droplet and that only gravitational and the surface tension forces act on the drop (i.e., the effect of vibration and turbulent flow are ignored), Equation 5.15 can be rewritten as:

$$D = \sqrt[3]{\frac{6\gamma d}{\rho g}} \quad (5.16)$$

where D is the drop diameter and ρ is the density of the molten drop at its melting point. The physical properties of several metals of industrial interest and their critical drop size are listed in Table 5.1.

Table 5.1 Physical properties of some widely used metals

Metal	Physical Property			
	Density (g/cm ³)	Melting Point (°C)	Surface Tension (N/m)[107]	Drop size (m)
Al	2.38	660	0.91	7.03 x 10 ⁻³
Ti	4.13	1660	1.65	7.13 x 10 ⁻³
Ni	7.90	1453	1.78	5.89 x 10 ⁻³
Cu	8.00	1083	1.3	5.28 x 10 ⁻³

It can be seen that large particles are produced through this mechanism. As it was mentioned, this is an ideal case where only the effect of gravitational and surface tension forces are considered. In the PA process, three atomization mechanisms were observed as a function of wire feeding rate to power ratio.

5.3 RESULTS AND DISCUSSION

5.3.1 Metal Feeding

In reactive plasma spraying, the yield of reaction between reactants depends on temperature. Several factors determine the particle temperature in the plasma environment. These are: plasma power, plasma gas composition, particle residence time in the plasma jet, particle size and shape, particle trajectory in the plasma jet, and physical and chemical properties of the particle. Among these, particle size and particle size distribution control particle temperature and reaction. The ideal case for reactive plasma spraying or even plasma spraying is to inject mono-size powder with uniform shape into the plasma region and expect them to follow the same trajectory. Overall, four methods of metal injection into the plasma stream can be considered:

- (a) *Injection of metal vapour* into the reactive plasma environment. This might be the most desirable way of metal introduction since a high surface area and a high temperature are guaranteed for the reaction. However, this method is very energy intensive and requires a very high level of vacuum during vaporization and transportation of the metal vapour.
- (b) *Molten metal* can also be injected to the plasma system. This method guarantees the supply of high temperature metal into the reaction zone, however, it does not produce a uniform molten droplets for the reaction. Therefore, particles react differently and upon deposition produce a non-uniform microstructure.
- (c) *Metal powder* can be the metal source for the reaction that occurs in the plasma. This is the best method of supplying a uniform particle size metal droplet since powders can be classified according to their size before injection. However, a mono-size powder of metals (if available) is very expensive. In addition, since the metal is

injected in the solid form, high temperatures cannot be obtained. The thermal energy of the plasma is used to melt the powder particles and so reduces the overall efficiency of the process. Therefore, to obtain a high particle temperature, very fine metal powder should be injected into the plasma. Therefore, this creates a technical problem associated with feeding very fine particles into a plasma stream.

- (d) *Solid shapes of metals* can be fed into the plasma jet. The solid shapes of metals such as: wire or rod are injected into the hot plasma jet where they melt by the thermal energy of the plasma, and are atomized by the high velocity plasma jet. A distribution of molten droplet size is produced which is intrinsic to most of atomization processes. The great advantage of this method is in the feed control, which unlike molten metal feeding, provides less control and precision of feeding. However, it uses the plasma energy for the melting process, and hence limits the maximum temperature attainable by particles.

All of these cases except case (a) were investigated in this study. In this chapter only case (b) and (d) are discussed since they dealt with atomization.

5.3.1.1 Feeding Molten Metal

The feeding of molten Al into the triple plasma system was investigated by melting Al in a bottom pouring resistance furnace which delivered the molten Al into the apex of the impinging plasma jets through a graphite nozzle. The powder produced was collected in the medium size reactor (2 m height and 1.5 m diameter). Part of the spray was produced as a deposited cake at the bottom of the reactor since the travel time for these particles was not long enough for complete solidification. Therefore, they deformed on impact and produced a deposit.

The main objective for feeding molten Al was to study the average particle size of the atomized powder and investigate the possibility of producing fine powder ($\sim 50 \mu\text{m}$) with a narrow particle size distribution. The advantages of molten metal feeding into the system are: (a) the elimination of melting and thus a higher particle temperature resulting in a high reaction yield, and (b) increased production rate ($\sim 200 \text{ g/min}$) as compared with wire feeding (30 g/min). The effects of three important process parameters which were plasma current (or power), argon gas flow rate, and Al melt temperature were investigated according to the experimental design shown in Table 5.2.

Table 5.2. Experimental design and responses for liquid Al feed plasma atomization

Experiment #	Current (A)	Argon flow rate (L/min)	Al melt temperature ($^{\circ}\text{C}$)	Average particle size (μm)	Al feed rate (g/min)
1	250	110	800	218	171
2	200	130	750	345	106
2	200	130	750	249	163
3	250	110	800	351	127
3	250	110	800	274	198
4	300	130	850	262	117
5	300	130	750	294	110
6	200	90	750	242	90
7	200	130	850	242	169
8	200	90	850	260	106
9	300	90	850	245	52
10	250	110	800	339	62
11	250	110	800	407	67

The analysis of the data also are shown in Table 5.2 reveals no reproducibility of the results. In other words, no trends can be seen between the investigated variables. The main objective

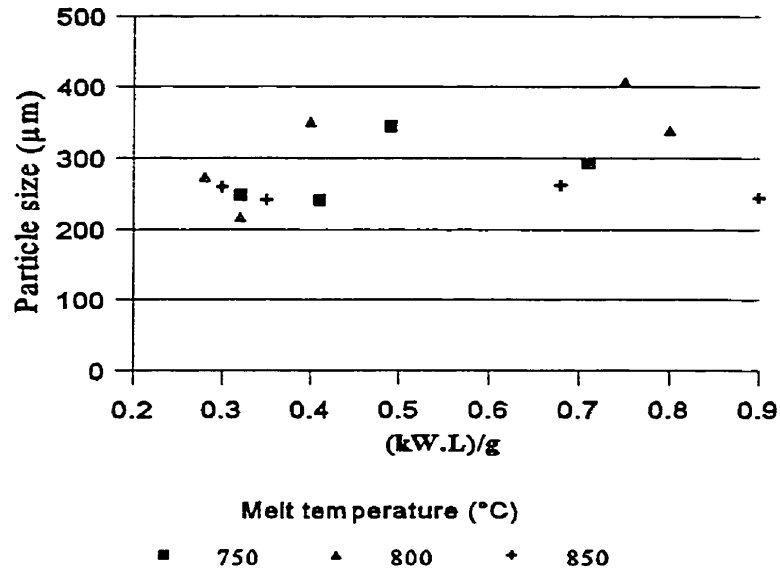


Figure 5.3. Average particle size as a function of the product of power and argon gas flow rate per gram of Al.

of using such experimental design was to understand the dependency of the variables on each other and the importance of each variable on the average particle size. These results also dictate that other variables are more important than those considered in Table 5.2. Increase in gas flow rate and power of the plasma is expected to produce a finer particle size since both increase the momentum of the impinging jet on the molten stream. The combined effect of these two parameters revealed no trend in the results, as shown in **Figure 5.3**. Alignment of the three plasma torches, non-uniform plasma jets, difficulty in maintaining a constant flow rate of molten metal feed, and erosion of the graphite nozzles were identified as the major sources of error in this set of experiments. Later in plasma atomization study using metal wires it was found that the alignment of the three plasma jets is very important. Slight deviation of torch center line from the apex reduces the overall energy available for atomization.

The uniformity of the plasma jet depends on: plasma power, plasmagas flowrate, and geometry of the accelerating nozzle. Plasma power is the product of ampere and voltage of the torch. The plasma power can be adjusted by the current only and the operating voltage

of a torch varies by the arc attachments and the arc length inside the electrode and are out of the operator's control. Therefore, by establishing a constant current for all torches, a constant power cannot be expected. Theoretically, if all of three torches are the same design and electrodes are changed regularly and simultaneously, obtaining uniform jets is possible. However, maintaining such conditions is very difficult and very costly.

Another reason for discrepancy in the results originated from the use of accelerating nozzles. Since they are installed manually, a uniform alignment through all of the experiment was not maintained. In addition, enlargement of the nozzle I.D. was observed as a function of time and due to the eccentricity of the nozzle I.D. in respect to that of cathode I.D., a non-uniform erosion was observed from one nozzle to another.

A constant level of molten metal was maintained (at the beginning of the experiments) and the same nozzle size was used through all of the experiments, however, a uniform flow rate of molten metal was not obtained. The main reason for this was the displacement of the metal feeding nozzle from one experiment to another. The jet velocity and pressure change abruptly due to the turbulent nature of the system at the regions near the impingement of the three plasma jets. It is postulated that there exist a variation of pressure at the tip of the molten metal feeding nozzle. Due to the displacement of this nozzle from one experiment to another and pressure variation, non-uniform molten metal feedrate was observed. The importance of metal feeding nozzle alignment with the apex was realized with atomization experiments using wire. The other fact is the change of plasma jet characteristics (i.e., velocity, pressure, and dimensions) by variation of plasmagas flowrate and the plasma power. Both parameters were altered in the experimental design, as shown in Table 5.2, which may affect the aerodynamics at the nozzle tip and consequently the molten metal feed rate. Overall, it can be concluded that powder with an average particle size between 200 and 400 μm and production rates as high as 177 g/min can be achieved using molten metal feed approach.

5.3.2 Feeding Metal Wire

Initial setup

Metal wires were fed into the triple plasma spray system and the average particle size of the product powder was measured as a function of power per gram of Al, as shown in **Figure 5.4**. In these experiments, Al wire (2.38 mm diameter) was atomized; no plasma jet acceleration nozzle was used; and powder was collected in the small atomization reactor. These data are based on about 30% of the total powder product since the rest of powder (70%) could not be collected since it formed a deposit at the bottom of the reactor. These results show that at low kW/g of Al, larger particle sizes are produced. In addition, for a given kW/g, finer average particle size powders are produced with high power. This can be explained by an increase in plasma jet velocity resulting from an increase in power. It was mentioned earlier that in gas atomization, higher gas velocity reduces the average particle size of the powder. It also can be seen that at higher kW/g, the average particle size increases again showing that there is an optimum value for kW/g. It is believed that the ratio of kW/g plays an important role in defining the melting location of the wire.

5.3.2.1 Low Ratio of Wire Feed Rate to Power

under these conditions, a mechanism similar to drop formation explained above at a low ratio of wire feed rate to plasma power is observed. This is shown schematically in **Figure 5.5(c)**. However, about two orders of magnitude finer particles were produced than those given in Table 5.1. The reason being that following the detachment of a molten droplet from the wire, it travels through the high velocity and hot regions created by the triple plasma jet system. A probable drop formation mechanism is that molten metal on the wire surface is formed and is pushed toward the tip by the drag force of the gas. However, this is opposed by the surface tension force acting on the wire. This force attempts to retain the droplet attached to the wire.

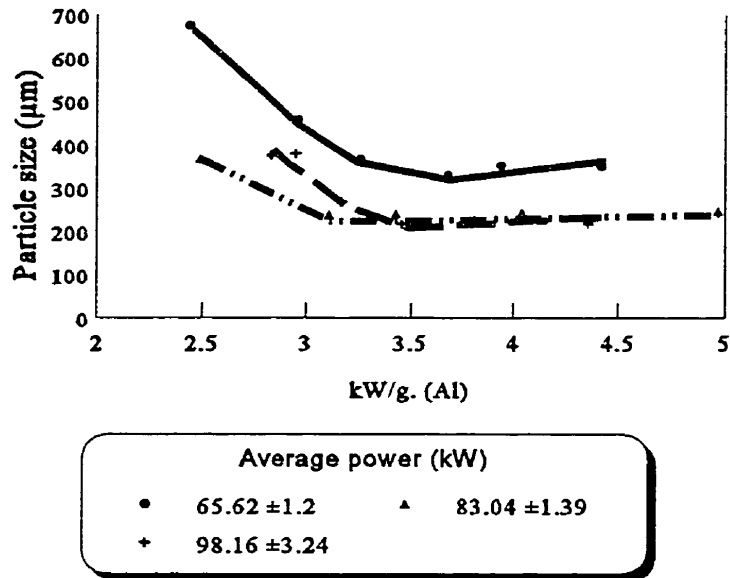


Figure 5.4. Average particle size of Al powder produced by plasma atomization as a function of kW/g, 2.38 mm Al wire dia. and no accelerating nozzle were used.

As more metal accumulates, the area over which the drag force applies is increased. As it is pushed toward the tip, the perimeter of the droplet attachment point decreases. When the drag force overcomes the surface tension, the droplet detaches from the wire and another starts to form. After the molten droplet leaves the wire tip, it is broken apart by the gas stream and bursts into a cloud containing thousands of finely atomized particles. This suggests that molten metal would be removed periodically in discrete droplets. The molten droplet, travelling in this region is subjected to turbulent aerodynamic forces, loses its structural integrity and breaks-up into finer particles. This stage can be considered as a secondary atomization process. The particle trajectory in this region greatly determines its breakup into fine particles. The ideal case is when the molten drop travels through the apex where the highest atomization efficiency is expected. However, this is not always the case, often the turbulent flow around the molten droplets causes them to become unstable, thus an arbitrary path through the impinging jets is taken. Therefore, drops are not treated evenly through the atomization region and particles with various sizes are produced. This variation in size determines the particle temperature and velocity in the hot combined jets of plasmas. Consequently, the resultant particle velocity and temperature govern the reaction yield

the quality of the spray-formed deposit which will be discussed in the reactive plasma spraying chapter.

5.3.2.2 High Ratio of Wire Feed Rate to Power

In the PA process, the production rate is controlled by the melting rate of the feed wire. If the wire is fed faster than the melting capability of the system, only surface melting of wire occurs. The core of the feed wire is passed through the hot region and remains unmelted. An example of this case is shown schematically in **Figure 5.5(b)**. A combined particle formation mechanism is the most probable approach. This is a combination of drop formation explained above and another mechanism based on shear forces. Upon the passage of the wire through the high temperature region, the wire tip reaches high temperatures and softens. The shear forces applied by the high velocity jets either peels off a thin layer of the metal on the surface or deforms the wire tip to fracture separating it from the feed wire. Powders produced with high ratios of wire feed rates to power are coarse and elongated.

5.3.2.3 Optimum Ratio of Wire Feed Rate to Power

At an optimum ratio of wire feed rate to power, the wire melts and is atomized at the apex of the system where the highest temperature and velocity of the plasma jets act on the wire. This case is shown schematically in **Figure 5.5(a)**. Upon formation of a very small quantity of molten metal, it is detached from the wire by the high velocity jets and further atomized to finer particles. In other word, no chance is given for the drop to grow in size before detachments. To obtain a simultaneous melting and atomization at the apex in the triple plasma system, an energy balance is required between the energy supplied to the wire and the energy consumed by the wire for melting.

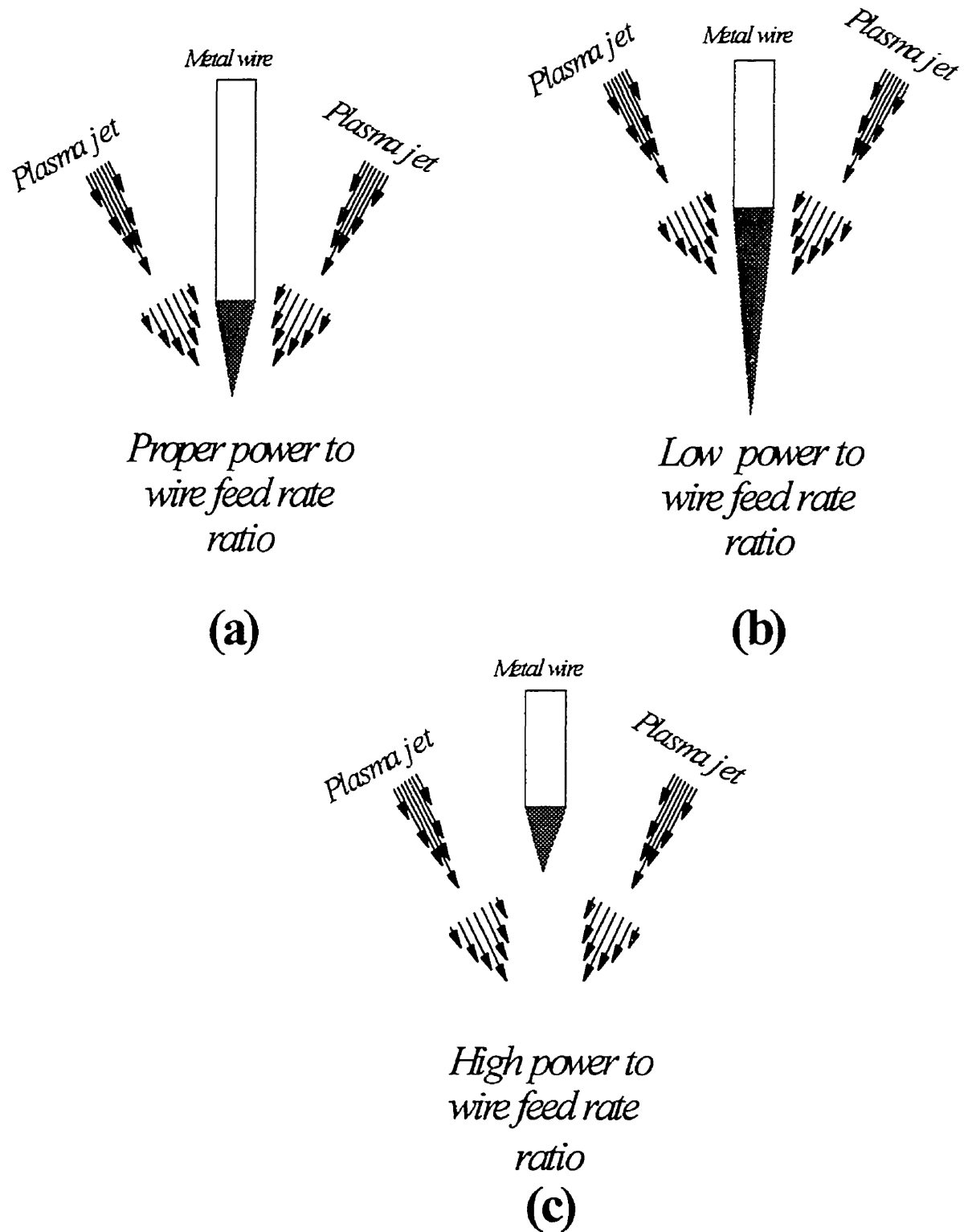


Figure 5.5. Various mechanisms of melting and atomization of wire in plasma atomization.

5.3.3 Melting Rate

Wire feeding into a very hot plasma jet, as in the plasma atomization processes, can be considered as heat flow in a semi-infinite system. The thermal energy of the very high temperature and high velocity plasma jets is convectively transferred to the surface of the feed wire which consequently is transferred through the wire by conductive heat transfer. Here, it is assumed that the convective heat transfer to the surface of the wire by the plasma jets is extremely rapid and the overall heat transfer to the wire is controlled by conductive heat transfer.

The general heat conduction equation for one-dimensional heat flow,

$$\frac{\partial T}{\partial t} = \alpha \frac{\partial^2 T}{\partial x^2} \quad (5.17)$$

shows that T depends on x and t . The solution of this equation results in:

$$\frac{T - T_i}{T_o - T_i} = \operatorname{erfc}\left(\frac{x}{2\sqrt{\alpha t}}\right) \quad (5.18)$$

where, T_i , T_o , T and are initial and along the wire temperature, hot end temperature at $x=0$, and temperature at distance x and t **Figure 5.6**.

For the plasma atomization processes, it can be assumed that the tip of wire is always at the melting temperature (T_m) of the feed metal since the molten metal drop is sheared off by high velocity jets upon formation. For unit surface area of a drop-wire interface, the rate of melting (\dot{x}) can be formulated as:

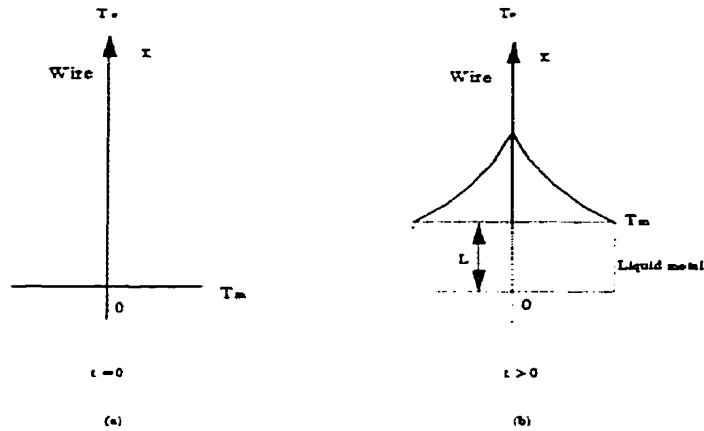


Figure 5.6. Temperature profiles during melting of a wire in triple plasma system.

$$-k_m \frac{\partial T}{\partial x} = \frac{\partial q}{\partial x} \tag{5.19}$$

using the definition of the error function,

$$\frac{\partial T}{\partial x} \Big|_{x=0} = \frac{T_m - T_0}{\sqrt{\pi \alpha t}} \tag{5.20}$$

and substitution in Eq. (5.19),

$$q = \frac{2(T_m - T_0)}{\sqrt{\pi}} \sqrt{k C_p \rho} \sqrt{t} \tag{5.21}$$

Therefore, the rate of heat extraction by wire through the system is determined by: melting temperature, thermal conductivity, heat capacity, and the density of the metal. The melting rate for a metal wire therefore, depends on the energy required for melting that wire and its

energy extraction power from the system. *Heat diffusivity* ($kC_p\rho$) of a material should not be confused with *thermal diffusivity*. Heat diffusivity is a measure of the ability of the material to absorb heat. In Eq. 5.21, the rate of heat absorption by wire is increased by increasing T_m since a larger temperature gradient is obtained, and increasing the heat diffusivity of the wire. The optimum wire feed rates of various materials are plotted versus heat diffusivity in **Figure 5.7**.

The melting rate of a metallic wire in a triple plasma system depends on various parameters including:

-the *physical properties* of the feed metal such as: thermal conductivity, heat capacity, and the energy required for melting. Higher thermal conductivity and thermal diffusivity and lower energy required for melting increase the melting rate of the feed wire. Heat diffusivity is believed to represent the melting behaviour of the wires in the triple plasma system since it combines the physical and thermal properties of the material. Thermal diffusivity (α) can also be used to represent the melting behaviour of metallic wires in triple plasma system.

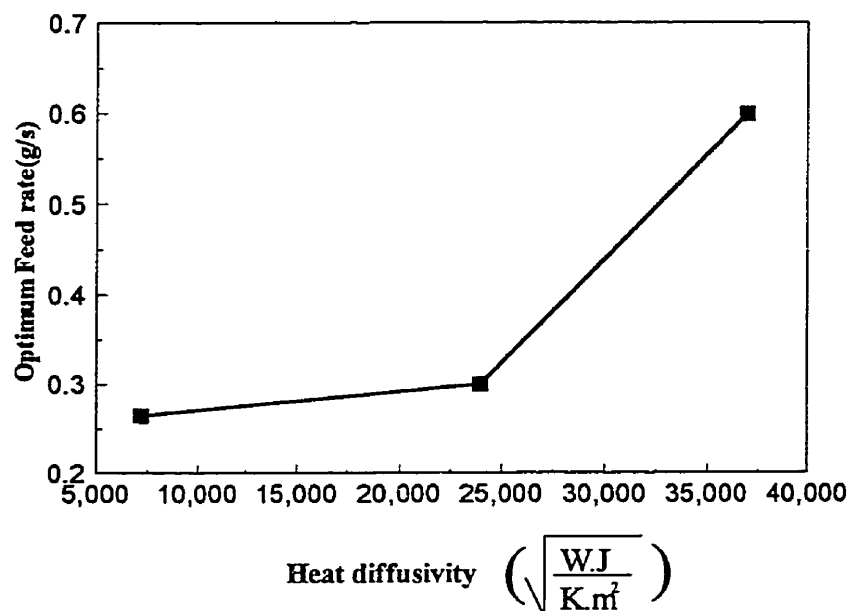


Figure 5.7 Optimum feed rate as a function of heat diffusivity..

Thermal diffusivity is:

$$\alpha = \frac{k}{\rho C_p} \tag{5.22}$$

where: k , ρ , and C_p are thermal conductivity, density and specific heat, respectively.

The physical interpretation of α is that it provides a measure of heat transport (k) relative to energy storage (ρC_p). However, α is not the only factor determining the melting rate and the energy required for melting should also be taken into account. The results of optimum feed rates for atomized metal and their physical properties are listed in Table 5.3. and shown schematically in Figure 5.8.

Table 5.3. Physical Properties and the Optimum Atomization Feed Rate of Atomized Metals

Material	T _m K	k W/m.K *[108]	ρ kg/m ³	C _p (J/kg.K)	Heat Diff. (m ² /s) x 10 ⁶	Feed rate	Latent heat of fusion J/g[109]	Energy req. For melting J/g
						g/s		
Ti	1953	23	4500	510	10.02	0.27	400	1244.05
Cu	1358	368.5	8933	385	107.15	0.60	213.18	621.28
Al	933	225.5	2702	902	92.52	0.43	397	969.77

* Mean value of thermal conductivity

-The *surface chemistry* of the wire changes the heat transfer mechanism from the high temperature plasma jets to the wire. For example, Al wire always has a thin layer of Al₂O₃ on

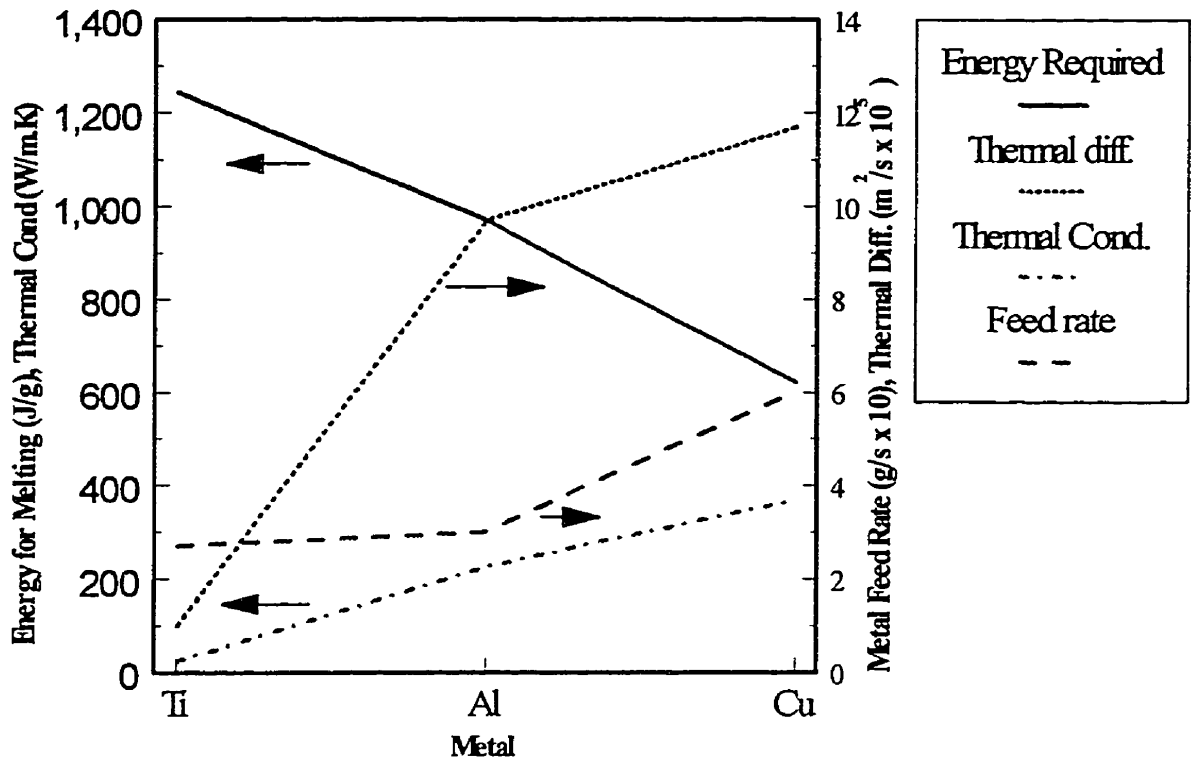


Figure 5.8. Melting rate of metal wires in triple plasma system (Wire dia. 1.5 mm, Plasma power = 100 kW).

its surface which requires 2135 (J/g) for melting and is 2.2 times more energy than that of non-oxidized Al. In addition, due to the low thermal conductivity of Al_2O_3 , 16.5 (W/m.K) which is 14.4 times lower than Al, it acts as a thermal barrier coating on the surface of the Al wire and slows the heat transfer through the wire. *Plasma jets thermal properties* also can affect the melting rate of the wire in the triple plasma system. The important thermal properties of the plasma jets, in this regard, are: temperature, jet velocity, power, density, and viscosity of the plasma jet. For the simplicity of this study a constant plasma power and chemistry (pure argon), and a fixed nozzle geometry were used during the atomization experiments. The evaluation of these parameters on melting rate of feed wire is a complex task since they are dependent variables. For example, by increasing the plasma power; the temperature distribution pattern in plasma jet changes which alters the plasma jet velocity and viscosity. Plasma chemistry also changes the plasma temperature, density, temperature, and velocity.

influence the melting rate of a wire. The dependence of melting rate on the energy required for melting is rather obvious and it can be expected that metals which require higher energy for melting, melt slower since the energy input is kept constant for the feed rates reported in Table 5.3.

If the effects of these two variables (i.e., energy required for melting(E , J/g)) and k , W/m.K) on optimum wire melting rate (F , g/s) of a 1.5 mm diameter wire are studied, linear empirical relationships are obtained as shown below:

$$F = 9 \times 10^{-4} k + 0.205 \quad (5.23)$$

$$F = -5.4 \times 10^{-4} E + 0.905 \quad (5.24)$$

From the above discussion, the melting of a new metal or an alloy can be estimated in a triple plasma system. It is also interesting to understand the relationships between the melting rate and plasma power, plasma forming gas composition and wire diameter. The effect of these parameters on wire melting rate were not studied in depth due to limitation in the power supply, availability of wire in various diameters.

The understanding of melting rate of various wires in the triple plasma system was necessary to determine the amount of TiCl_4 or any other reactants required for reactive plasma spray forming. Another important factor in reactive plasma atomization is the size of the metal particles produced by plasma atomization before their reaction with reactive gases such as TiCl_4 and Al. Therefore, understanding the average particle size of the powder produced through plasma atomization was essential.

5.4 Reducing the Average Powder Size

It was shown in Figure 5.4 that powders with an average particle size of 200–250 μm can be produced. This size range is large for reactive plasma spraying since the total surface area available for reaction is low and high particle temperature cannot be achieved. Three approaches were taken to reduce the average particle size of the product powder. These were: (a) using a liquid metal feed, (b) decreasing the wire diameter, (c) aligning of the jets, and (d) using a plasma jet accelerating nozzle. Processing with liquid metal was discussed earlier in this chapter and proved to be difficult to control. In addition, the average particle size was between 200 and 400 μm which is large for both reactive plasma spraying and simple powder production.

5.4.1 Effect of Wire Diameter on Average Particle Size

The idea of decreasing average particle size by reducing the wire diameter can be derived from Eq. (5.16). This equation is true for static conditions when a liquid is hanging from a rod or wire. The validity of this equation has not been proven in the literature for the case of turbulent or dynamic conditions, which is representative of triple plasma atomization. Therefore, two wire sizes of Al were subjected to triple plasma atomization with 100 kW plasma power and the average particle size of the powder produced was compared as shown in Figure 5.9.

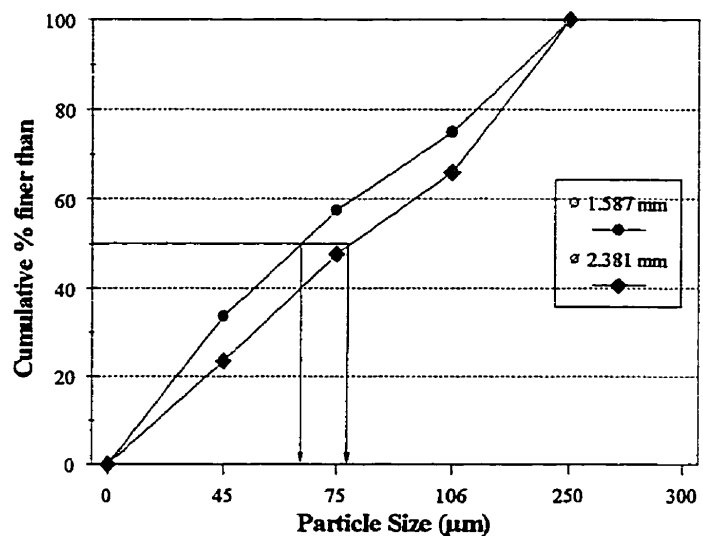


Figure 5.9. Average particle size as a function of wire diameter.

The average particle size was reduced from 80 to 65 μm when the wire diameter changed from 2.4 to 1.6 mm. Equation (5.16) predicts a 12% difference in the powder size while the plasma atomization results show 19% difference. The difference can easily be attributed to the turbulent nature of the impinging jets in the plasma atomization system. Equation (5.16) only considers gravitational and surface tension forces while in plasma atomization aerodynamic forces play an important role which cannot be easily quantified. However, this equation can be used to predict reasonably closely the average particle size as a function of wire size for the plasma atomization design used in this study.

5.4.2 Torch Alignment

Nozzle design is the heart of any atomization process and the challenge is to design a nozzle which maximizes the impingement of the gas and the liquid. Plasma atomization is no exception, and the best results were obtained when the alignment of three torches was improved. In gas atomization, the adjustment and alignment of the liquid stream with impinging gas are easier than plasma atomization since both the gas jet and the liquid channel can be configured into one piece. **Figure 5.10** shows the misalignment of the torches before correction. It can be seen that one torch is not aligned with the other two.

5.4.3 Torch Tip Distance from the Apex

In the original design, the torch tip distance from the apex was 12.5 cm. The plasma jet velocity sharply diminishes after exiting the torch, as shown in **Figure 2.2**. Therefore, the shorter the distance of the torch tip from the apex, the higher will be the jet velocity at the apex or in other words, at the time of atomization. This distance was reduced to 5 cm by moving the three torches closer together.

The individual effects of torch alignment and torch tip distance from the apex were not

identified since these two modifications were performed concurrently. However, the combined effect of these two factors was measured. The average particle size of powder was reduced to 145 ± 28 from about $250 \pm 34 \mu\text{m}$.

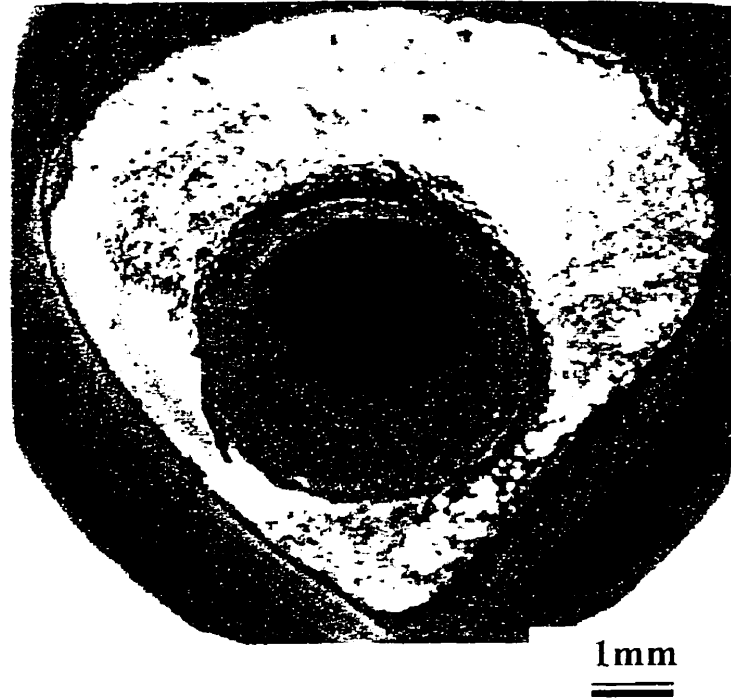


Figure 5.10. Photograph of the wire feeding nozzle before correction of the torch misalignment.

5.4.4 Plasma Jet Accelerating Nozzle

Plasma jet velocity is the most influential parameter for the reduction of the average particle size during plasma atomization. The aerodynamic pressure ($\rho_g v_g^2$) acting on a molten droplet, travelling in the plasma jet or attached to the wire, changes as the square function of the plasma jet velocity. It can also vary with plasma forming gas however, due to the only limited range of plasma forming gas compositions employed, this effect was insignificant. In contrast, a change in plasma jet velocity can affect the atomization process. The plasma jet velocity is

a complex function of torch design, type of plasma forming gas, gas flowrate, plasma power, and front nozzle design. Among these parameters, the plasma current and plasma forming gas flowrate were set at their maxima of 300 A and 120 L/min, respectively. The plasma forming gas was selected as argon and the option of introducing a secondary plasma forming gas such as hydrogen was not considered. Two design modifications were made on the torch. The first modification was a change in cathode I.D. from 7.5 to 6.35 mm and the second was using a plasma jet accelerating nozzle (**Figure 5.11**). This is a typical de Laval nozzle with a restriction diameter of 4.76 mm. The nozzle geometry was developed using various graphite nozzle sizes and visual observation of the shock waves in the plasma jet. The use of the plasma jet accelerating nozzle reduced the average powder size from 145 ± 28 to 60 ± 14 μm .

Graphite was used as nozzle material and fast nozzle erosion was observed which resulted in enlargement of the nozzle I.D. and consequently changed the plasma jet characteristics over time. In addition, graphite contamination was detected in the powder products which is undesirable. This problem may be resolved by using a water cooled refractory metal nozzle.

Two typical plasma atomized powders of Ti and IN 718 produced with optimum nozzle geometry are shown in **Figure 5.12**.

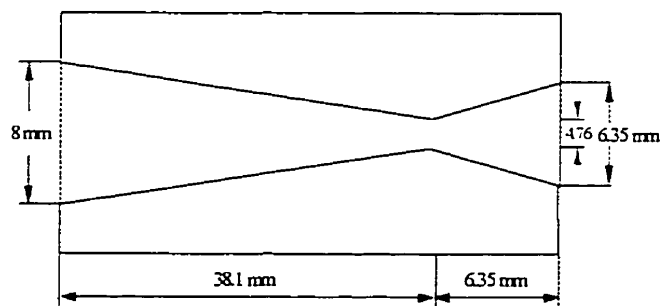
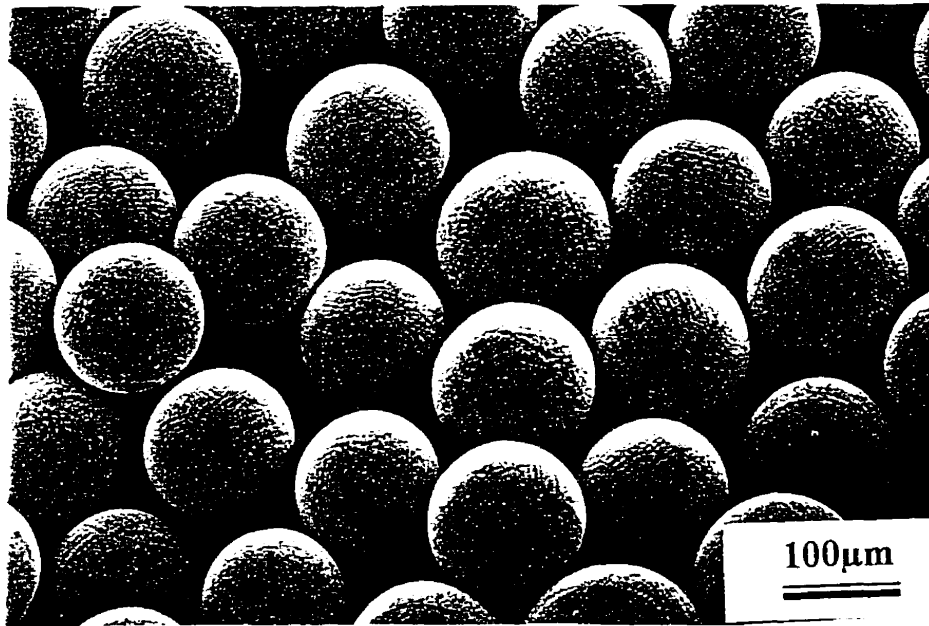
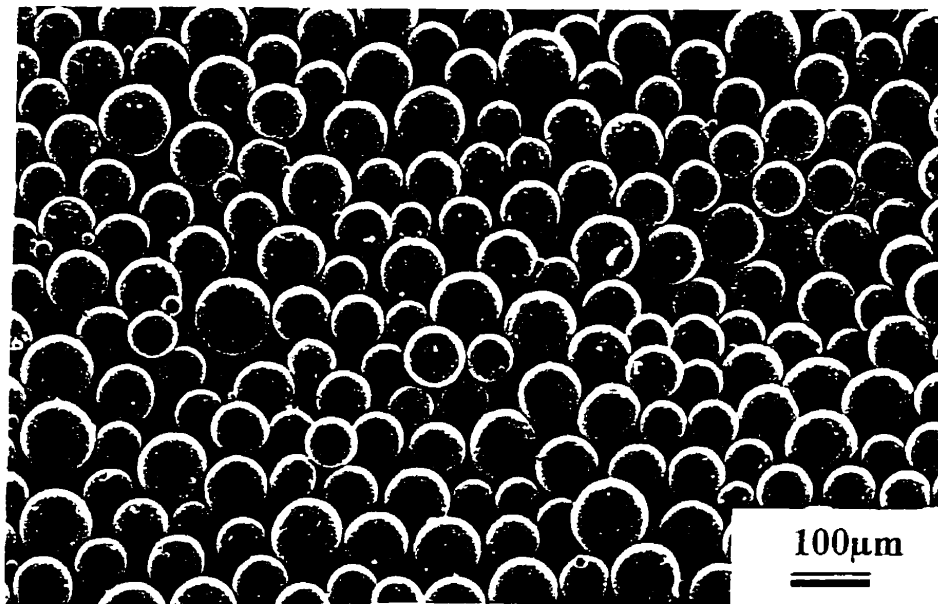


Figure 5.11. Schematic of the optimum nozzle design for plasma atomization.



(a)



(b)

Figure 5.12. SEM of (a) IN 718 and (b) Ti-6-4 powders (+45-75 μm) produced by plasma atomization process.

The powders produced through plasma atomization are very spherical with a very few satellites attached as can be seen from their micrographs. The high sphericity of these powders is very beneficial for applications, which require high flowability (such as plasma spraying) and high tap density (such as HIPping).

Besides a decrease in average powder size, the powder produced has a narrow distribution, which can be characterized by $d_{10} = 10 \mu\text{m}$ and $d_{90} = 110 \mu\text{m}$. This is considered a very narrow particle size distribution if it is compared with metal powders produced through water or gas atomization processes. It should be noted that production of a mono-size powder is almost impossible due to the non-uniform energy transfer from the atomizing medium to a liquid. This irregularity, which involves either velocity or temperature, is inherent to the nozzle design. For most nozzles, the velocity of the atomizing fluid in the center line is higher than that of the peripherals. Therefore, droplets are treated differently during atomization and a powder product with varying size is produced. The progress in reducing the average particle size and powder size distribution are summarized in **Figure 5.13**. Very similar powder

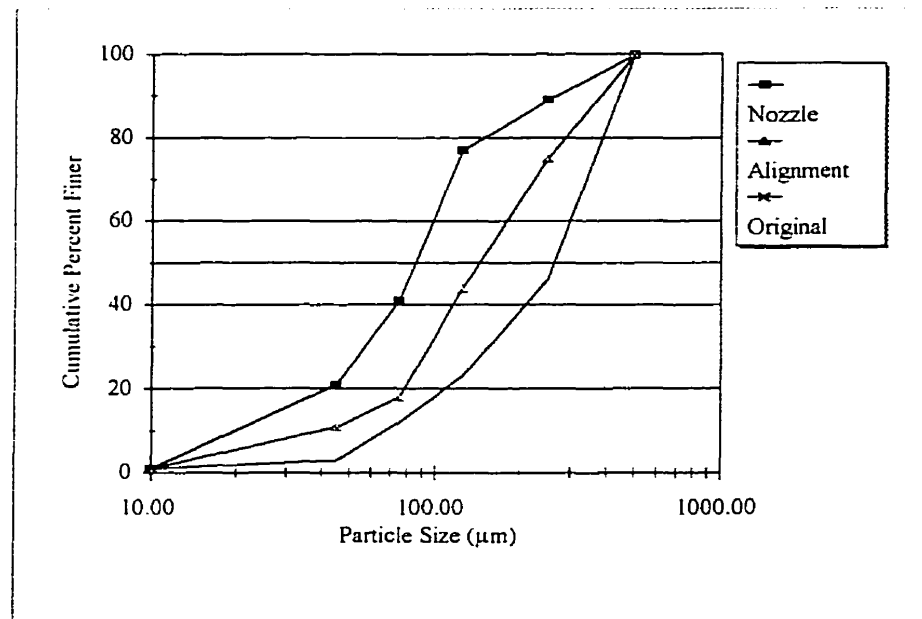


Figure 5.13. The effects of nozzle and torch alignment on particle size distribution in plasma atomization process.

size distributions were obtained for various atomized powders. The average powder size produced from the wire of (1.6 mm diam.) of Ti, Cu, and IN-718 (a nickel-based superalloy) showed only $10\% \pm 4.5\%$ difference at their optimum atomization conditions. These results are very close since an 8% error is usually associated with screen analysis[110]. This implies that the physical properties of the atomized materials are more important in defining the powder production rate and are less influential in controlling the powder size distribution.

5.5 Droplet Formation during Plasma Atomization

The exact mechanism of droplet formation from a wire fed into a plasma jet is not known. Understanding of the droplet formation in plasma atomization can be very helpful to predict their behavior in reactive plasma atomization. Furthermore, studying the droplet formation mechanism in plasma atomization can determine and classify the role of the important parameters during droplet breakup. The best method of investigating plasma atomization is to install and focus a camera on the wire tip and record the process. Unfortunately, such equipment was not available at the time of this research program. However, SEM was used to examine the morphology of the final powders. Morphological study of the powders revealed that the general particle formation mechanism for gas atomization (as shown in (5.1)) can be applied to plasma atomization using the wire feed system. Micrographs shown in **Figure 5.14** were taken from the powders produced by the plasma atomization process. Ligament formation, necking, and spheroidization steps are observed for the powders produced through plasma atomization. These powder examples for some reason solidified in flight before completion of the atomization process. Depending on the ratio of power to wire feed rate, only two to 10 percent of the total powder produced were irregular. It is believed that two droplet formation mechanisms are responsible for overall atomization. The first mechanism can be called primary atomization and occurs by the removal of small droplets from the wire tip. These particles spheroidize and solidify in flight without further breakup.

The other mechanism can be called secondary atomization which is the breakup of the large particles already detached from the wire tip. These droplets are further atomized by the high velocity plasma jets in flight. Since the droplet breakup has been delayed for these particles due to their size, they do not undergo a complete breakup and become irregular.

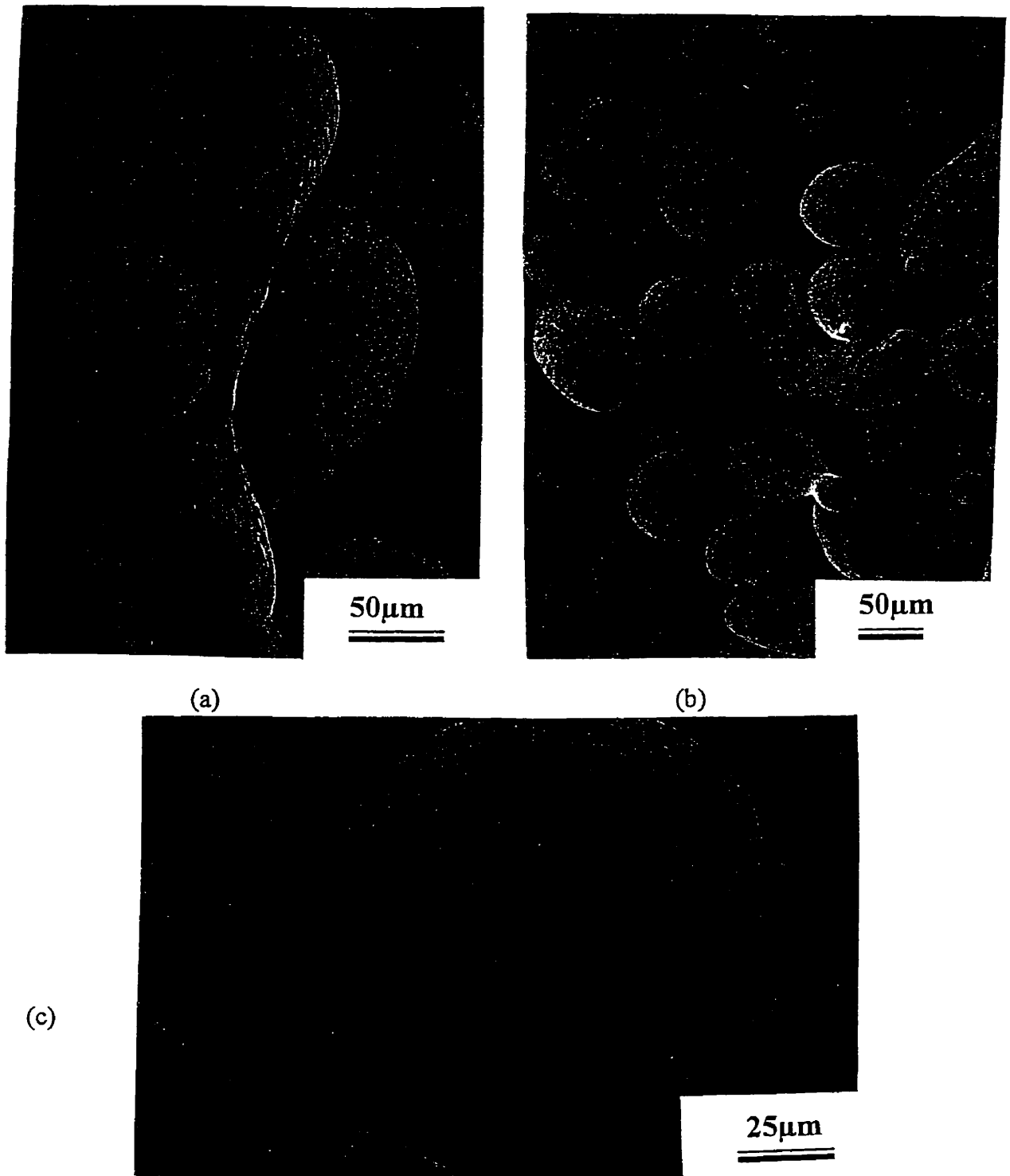


Figure 5.14. Droplet formation during plasma atomization; (a) necking, (b) spheroidization in progress, and (c) end of droplet spheroidization.

5.6 Comparison of Plasma Atomization (PA) with Other Competitive Technologies

Other atomization processes such as gas atomization (GA), rapid spinning cup (RSC), rotating electrode process (REP), and rapid solidification rate (RSR) are able to produce a specific range of particle size and distribution. The best method of comparing PA with these processes is based on average particle size, particle size distribution, powder morphology, contamination, and the microstructure [111].

5.6.1 Average Particle Size

Typical particle size distribution of powders produced by a variety of the atomization processes (as well as the plasma atomization) are shown in **Figure 5.15** [112]. The average particle size of a powder produced the PA process is 50 μm which is finer than those of the GA (80 μm), the RSR (65 μm), and the REP (150 μm); but is larger than that of the RSC (25 μm). The unique advantage of the PA process is the ability of incorporating a reaction into the atomization process and possibility of materials synthesis. In contrast, other atomization

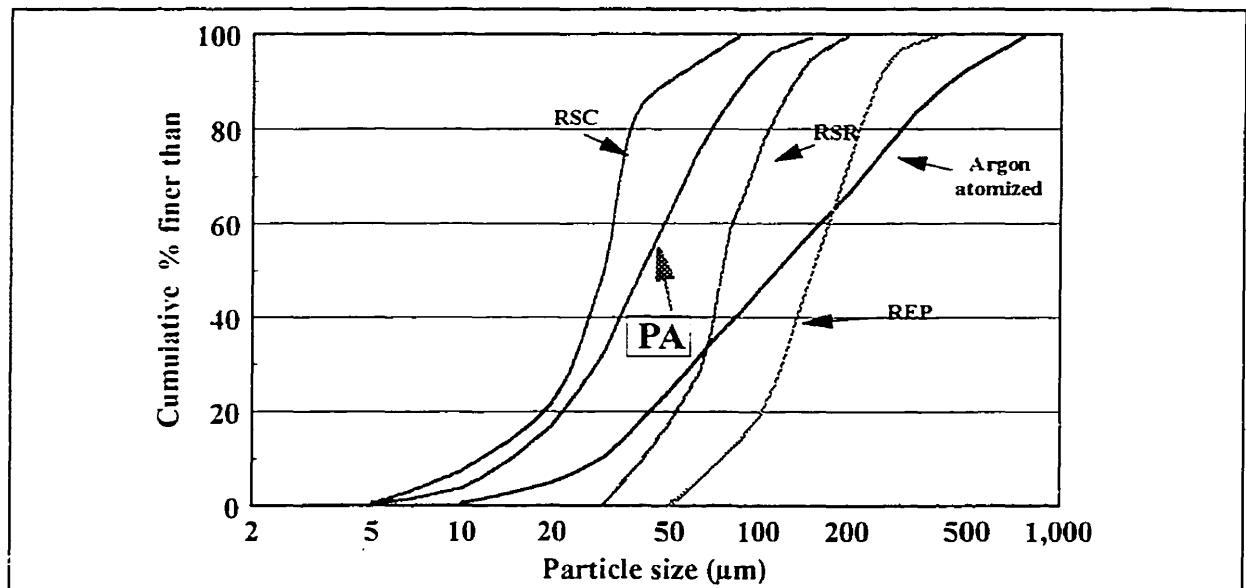


Figure 5.15. Comparison of average particle size distribution of atomization processes.

process cannot easily be used for such applications.

5.6.2 Particle Size Distribution

The particle size distribution for the PA process is narrower than those of the GA and REP, is in the same range of the RSC, and is wider than that for RSR. The particle size distribution for the powder produced through these atomization processes are summarized in Table 5.4. It should be realized that both the narrow and the wide particle size distributions are desirable depending on their applications. For example, thermal spraying requires a narrow particle size distribution while powder metallurgy demands a wider range in order to obtain a reasonable green packing density. The advantage of the powders produced through the PA process is that its average particle size and distribution can easily be classified for either thermal spraying or powder metallurgy.

Table 5.4. Average particle size and distribution for the atomization processes

Process	RSR	RSC	REP	GA	PA
10 % below (μm)	40	10	70	30	15
90 % below (μm)	90	40	200	500	100
Average particle size	65	25	150	80	50

5.6.3 Cooling Rate

The solidification rates for Cu and Al in the PA process were measured from dendrite arm spacing (DAS) observed on the surface of the powders and using the relationship between the secondary DAS and solidification rate provided in the literature and shown in **Figure 5.16** [112]. The solidification rates for Cu powder and Al powder produced through the PA process were 2×10^5 K/s and for 3×10^4 K/s, respectively. The solidification rate for Ti powder

was measured from the average β grain size[113]. The solidification rate was a function of the powder particle size and it was measured as 10^5 K/s for an average particle size of $50 \mu\text{m}$. From these solidification rates, the PA process can be classified as a rapid solidification process. Consequently, powders produced through this process can produce P/M parts which benefit from significant improvements in terms of mechanical, electrical, and thermal properties as well as corrosion resistance.

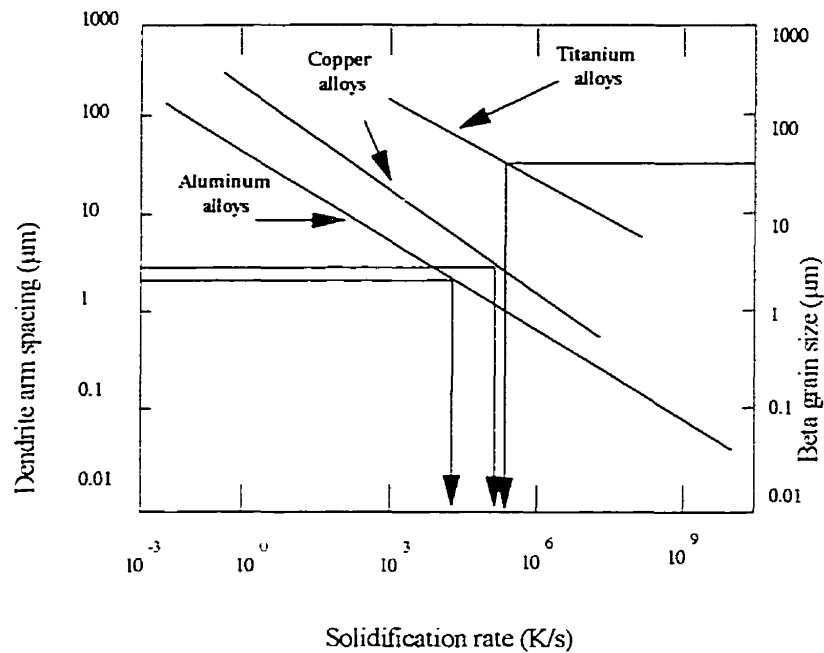


Figure 5.16 Secondary DAS and β grain size as a function of solidification rate.

5.7 CONCLUSIONS ON PLASMA ATOMIZATION

- 1- Torch alignment, the plasma jet accelerating nozzle, the ratio of total plasma power to wire feed rate, and wire diameter are the most influential processing parameters in determining the average particle size and size distribution of the powders produced through plasma atomization.
- 2- The plasma atomization process can produce powders with an average particle size of 50 to 60 μm with a narrow particle size distribution which is characterized by $d_{10}=15$ and $d_{90}=100$.
- 3- Although plasma atomization produces high quality powder, the production rate (melting rate) is limited to 1-2 kg/hr with the type of plasma equipment used in the current study.
- 4- Heat diffusivity, thermal conductivity, and thermal diffusivity of the feed wires are the most important criteria for predicting their melting rates and therefore atomization.
- 5- Poor data reproducibility were obtained using molten metal feed during plasma atomization which can be attributed to (a) the importance of metal feed rate to the system and (b) inaccuracy of controlling the molten metal feed rate.

CHAPTER 6

Al-Ti COMPOSITES

6.1. INTRODUCTION

Many advances in the aerospace and automotive industries are aimed at improving the efficiency and performance of their products by increasing the operating temperature and reducing weight. These improvements require materials with better mechanical properties but at a lower cost. Currently, conventional materials are used to the limits of their performance and cannot meet new design requirements.

Al-TiAl₃ composites are candidate materials for high temperature (>450°C) applications to replace some Ti-based alloys in the aerospace industry. The main advantage of this material over other composite materials is the presence of TiAl₃ phase, which is crystallographically similar to the Al matrix, and is stable at higher temperatures. The production of Al-TiAl₃ is associated with a few technical limitations due to the intrinsic characteristics of the Al-Ti system (Chapter 2, §11).

The mechanical properties of the Al-TiAl₃ composites depend on various microstructural features. In this regard, size, morphology, and distribution of TiAl₃ are the most important factors, which depend strongly on the manufacturing process. In the following sections, the production of Al-TiAl₃ composites will be investigated through five manufacturing processes: casting, powder metallurgy, reactive hot isostatic pressing (RHIPping), plasma spraying using elemental powders, and reactive plasma spraying. The emphasis will be on reactive plasma atomization and the comparison of results will be based on the morphology of the intermetallic phase. The mechanical properties of the material produced by reactive plasma spraying will also be assessed. Finally, the production problems associated with this process will be discussed and possible solutions addressed.

6.2. PRODUCTION OF Al-TiAl₃ COMPOSITES

6.2.1. Vacuum Plasma Spraying Using Elemental Powders

Plasma spraying is classified as a rapid solidification process and is likely to produce a supersaturated microstructure of Ti in Al. Such a supersaturated solid solution can be subjected to heat treatment to produce a fine and a well-distributed reinforcing phase throughout the matrix. However, there are technical limitations associated with the plasma spray process such as feed materials which are introduced in the solid state either as powder or wire. This greatly limits the choice of raw materials. For example, in the Al-Ti system, a supersaturated molten system is required which cannot be easily fed into the conventional plasma spray systems. To overcome this limitation, elemental powder of Al and Ti were mixed and sprayed using a powder feeder. The objective was to combine alloying with the plasma spray process. Alloying may occur either in flight or upon deposition.

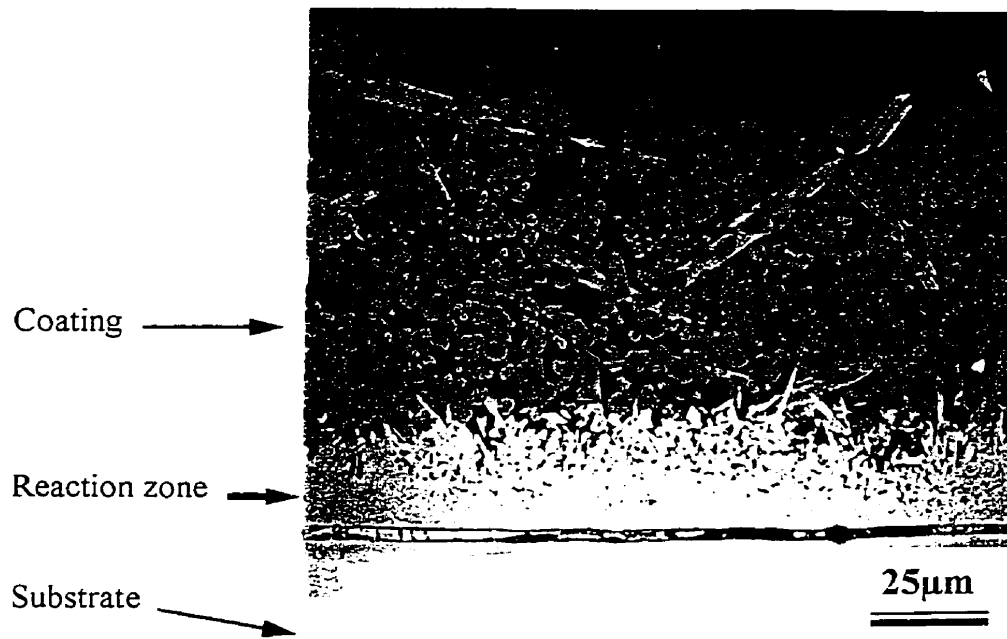
6.2.1.1. Spraying on Stainless Steel (SS)

A typical microstructure of a coating obtained on a stainless steel substrate is shown in **Figure 6. 1(a)**. This microstructure is the result of the experiment 1 in Table 6.1. Complete reaction between Al and Ti is observed in this microstructure forming TiAl₃ phase (gray phases). The EDS spectrum of this phase is shown in **Figure 6. 1(b)**. The intermetallic phase has an average particle size of about 5 μm which is finer than the average particle size of both the Al and Ti starting powders. The TiAl₃ phase is also evenly distributed in the Al matrix. The combination of these two factors, i.e., a fine and a well-distributed intermetallic phase in the Al matrix should grant good mechanical properties to the coating. A bright needle-like phase is also observed in the microstructure. The EDS spectrum obtained from this phase is shown in **Figure 6. 2(a)**. It is composed of mainly Al, Cr, Fe, and trace amounts of Ti and Ni. A reaction occurs at the interface between the Al-Ti coating and the SS substrate. The results of qualitative EDS analysis on the reaction zone showed a wide range of chemical compositions containing Fe, Cr, Ni, Ti and Al. This is a complex and brittle intermetallic compound causing cracking at the interface. The EDS spectrum of a typical reaction zone is shown in **Figure 6. 2(b)**.

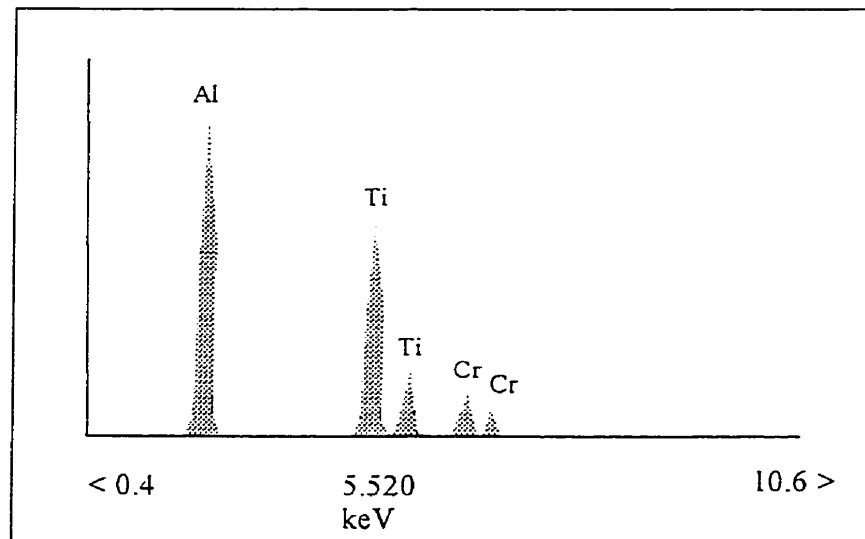
Table 6.1 Experimental set-up and their responses after 5 minutes of spraying.

Exp.	C.P.(mbar)	S.D.(cm)	Substrate	Ti (%)	T (μm)
1	60	40	SS	15	75
2	40	55	SS	15	50
3	40	40	Ti	15	10
4	40	40	SS	5	90
5	60	55	SS	5	460
6	60	40	Ti	5	97
7	60	55	Ti	15	100
8	40	55	Ti	5	0

C.P.: Chamber Pressure, S.D.: Spray Distance, T: Thickness

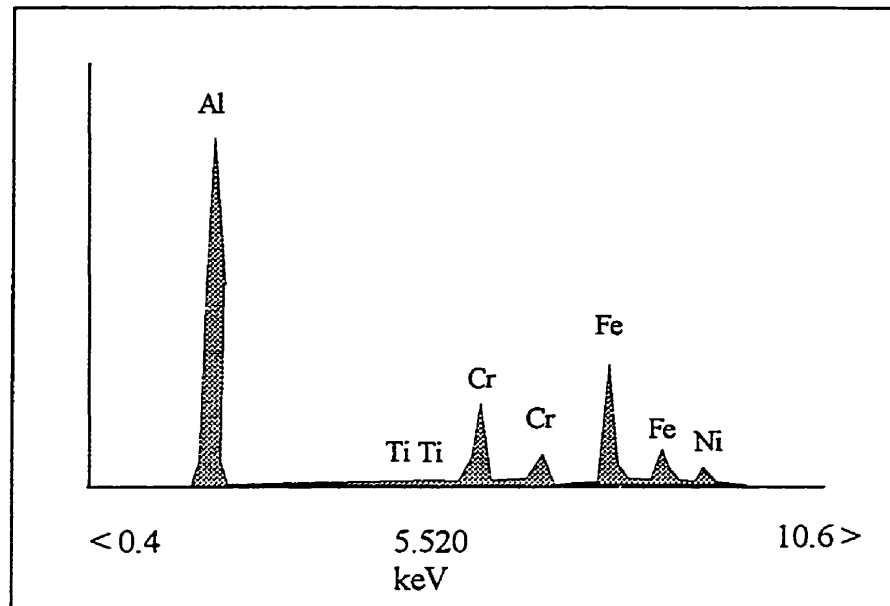


(a)

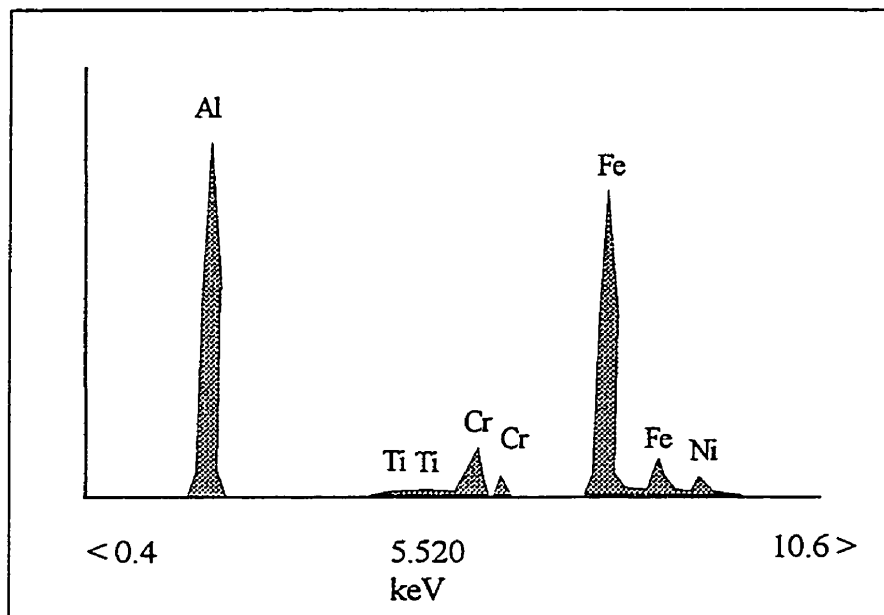


(b)

Figure 6. 1 (a) Backscatter image, and (b) EDS spectrum of the gray phase.



(a)



(b)

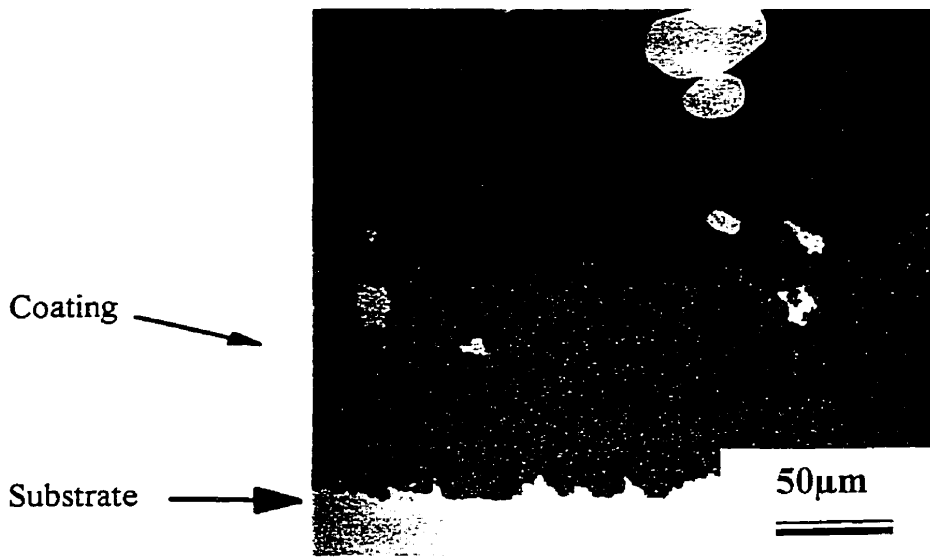
Figure 6.2 EDS spectrum obtained from (a) needle like phase (b) reaction zone.

6.2.1.2. Spraying on Ti Substrate

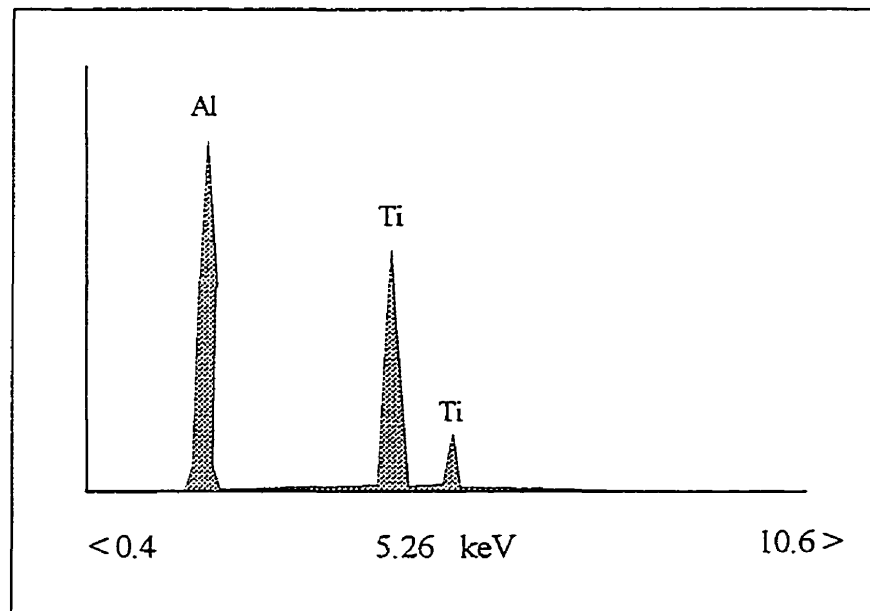
Compared with the coating deposited on SS, less reaction occurred between the Al-Ti coating and the Ti substrate, and a very narrow reaction zone was observed at the interface. **Figure 6. 3(a)** shows the back-scattered electron image (BEI) corresponding to experiment 7 in Table 4.1. The overall microstructure contains intermetallic particles in a matrix of Al. The interface is an Al-Ti intermetallic with a similar chemistry to the intermetallic phase in the matrix, but higher Ti content (see **Figure 6. 3(b)**) which might be coming from the Ti substrate. The interface of this series of coatings on the Ti substrate shows no sign of cracking or delamination. This can be attributed to the chemical and physical compatibility of the intermetallic phase with the Ti substrate.

6.2.1.3. Qualitative Chemical Analysis of the Deposits

The sprayed samples had a higher Ti content (4 ± 1.3 wt.%) than the bulk mixture of the powders used to spray these composites. This can be attributed to the separation of the powders in the powder feeder due to differences in density, particle size and morphology (see **Figure 4.6**). In addition, separation occurs in the plasma flame, since Al and Ti powders undergo different behaviour in the plasma flame due to their differences in physical properties (see Table 6.2). If we consider reactive plasma spraying using elemental powders as a combination of melting, alloying and casting, then the behaviour of these elements in the plasma flame can be compared. Al needs much less energy to melt (981 kJ/kg) than Ti (1295 kJ/kg). This difference would increase significantly if we compare the energy required for boiling. It can be concluded that most of the Al particles reach the substrate at a higher temperature than Ti powders. In fact, the shape of some of Ti particles in the microstructure confirmed that these particles had been only partially melted when they reached the substrate and only partially reacted with Al to form TiAl₃. A typical microstructure illustrating this behaviour is shown in **Figure 6.4**.



(a)



(b)

Figure 6.3 (a) BEI, and (b) the EDS spectrum of the interface of the Al-Ti powder sprayed on Ti substrate.

Table 6.2. Physical properties of Al and Ti.

Physical Property	Al	Ti
Melting point (°C)	660	1660
Latent heat of fusion (kJ/kg)	387	434
Boiling point (°C)	2467	3287
Specific heat (J/kg.K)	900	519
Density (kg/m ³)	2700	4500

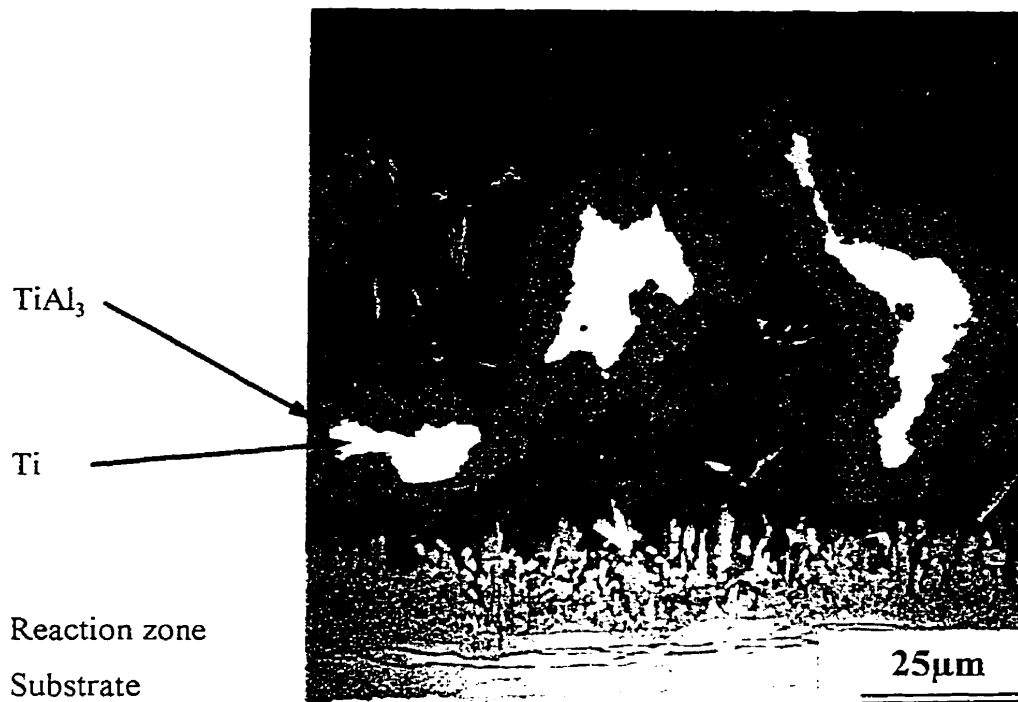


Figure 6. 4. Typical coating microstructure showing the unmelted Ti particles.

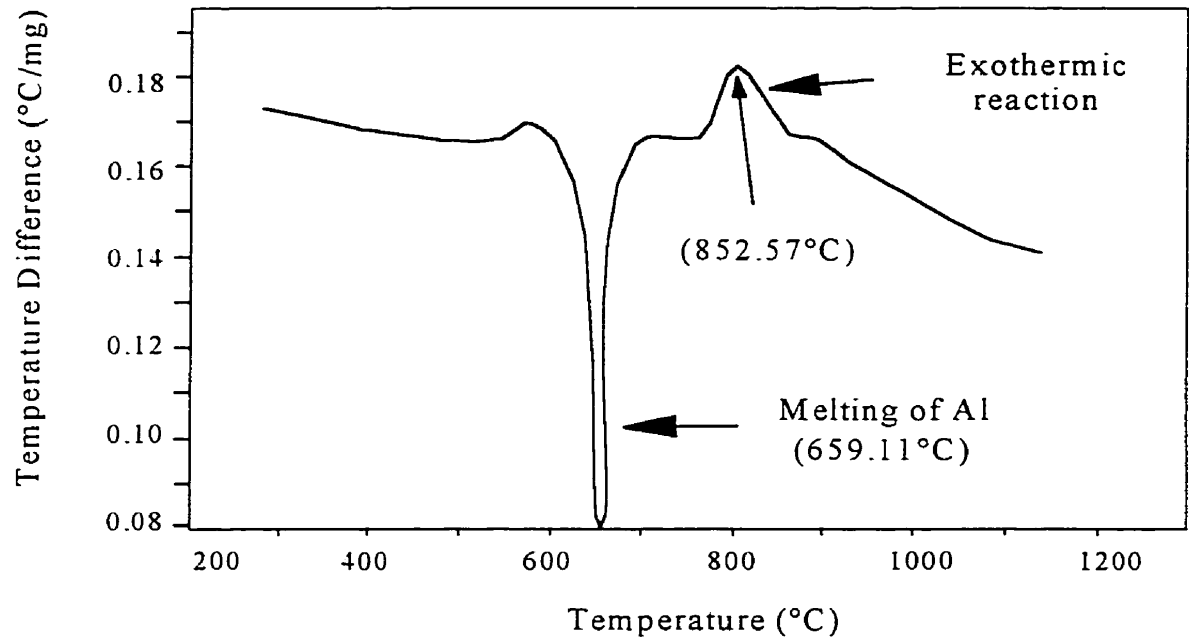
The high Ti content of the coatings can also be attributed to the high temperature of the substrate. The high temperature of the substrate provided a high fluidity for the Al phase in

the composites. Since the substrate stands vertically in front of the plasma torch, the molten Al flowed downward causing an overall increase of the Ti content. Some Al droplets flowed down and collided with Ti particles, forming other solid Al_xTi_y phases, which have higher melting points, ranging from 1370-1430°C.

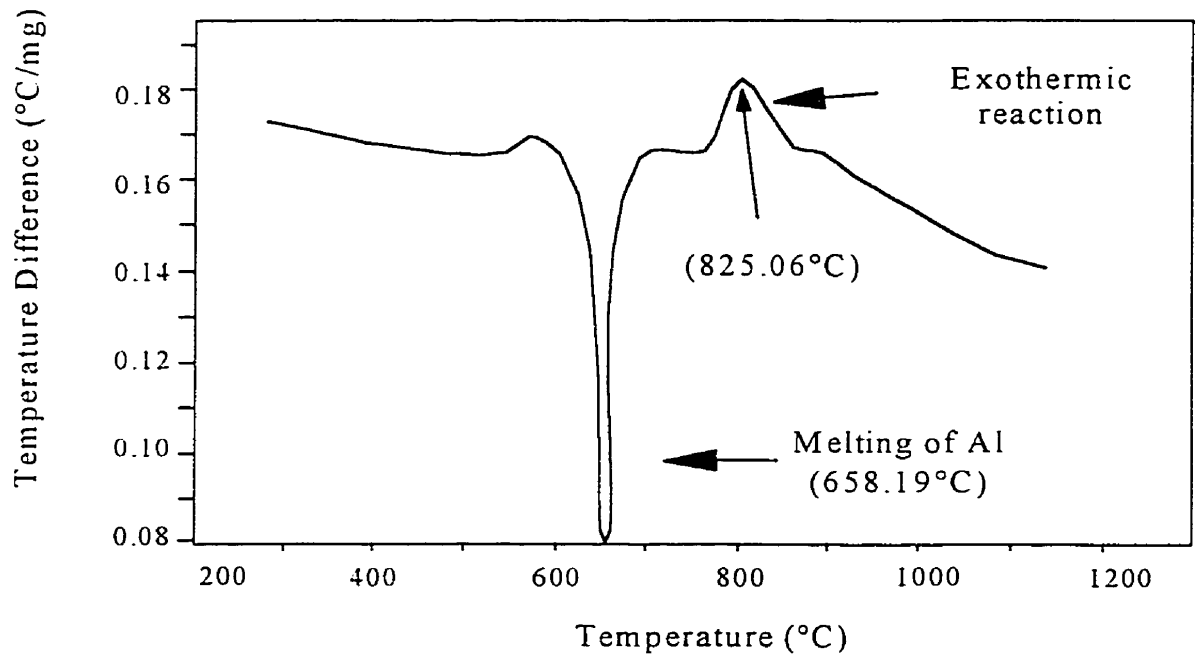
One solution to replace the Al flow is to lower the substrate temperature. However, this temperature should not be lower than 852°C in order to promote reaction. This temperature was determined from differential thermal analyses (DTA) performed on the powder mixtures of Al-5% Ti, Al-10%Ti, and Al-15%Ti, the results of which are shown in **Figure 6. 5(a), (b), and Figure 6. 6**, respectively. The results show various peak temperatures for the exothermic reaction of Al and Ti. This variation of the peak temperatures can be attributed to the different Ti content involved in the reaction. The peak temperature of the reaction decreases with increasing the Ti content.

In plasma spraying, fixing the substrate temperature would be difficult since it varies with torch current, spray distance, plasma gas flow rate, powder carrier gas flow rate, vacuum chamber pressure, spray time, and Ti content of the premixture. In fact a new experimental design is required to optimize these factors to obtain the optimum substrate temperature.

It seems that this problem would be reduced by increasing the Ti content. The increase in the Ti content will increase the probability of collision between the Al and Ti powder particles for a given residence time on the substrate. Then the Al droplets will collide with the Ti powders and react to form a high temperature intermetallic before flowing off the substrate. This needs a uniform flow of both the Al and Ti powders through the feed system. Another solution might be using finer Ti powder. In this way, the distance between Ti particles in the coating will be decreased. The overall reaction would be completed in a shorter time providing less time for Al to flow off the substrate. Even if Al flows on the substrate, there would be a greater chance for it to pass over a Ti particle and react with it.



(a)



(b)

Figure 6. 5 DTA analysis for (a) Al-5%Ti and (b) Al-10%Ti.

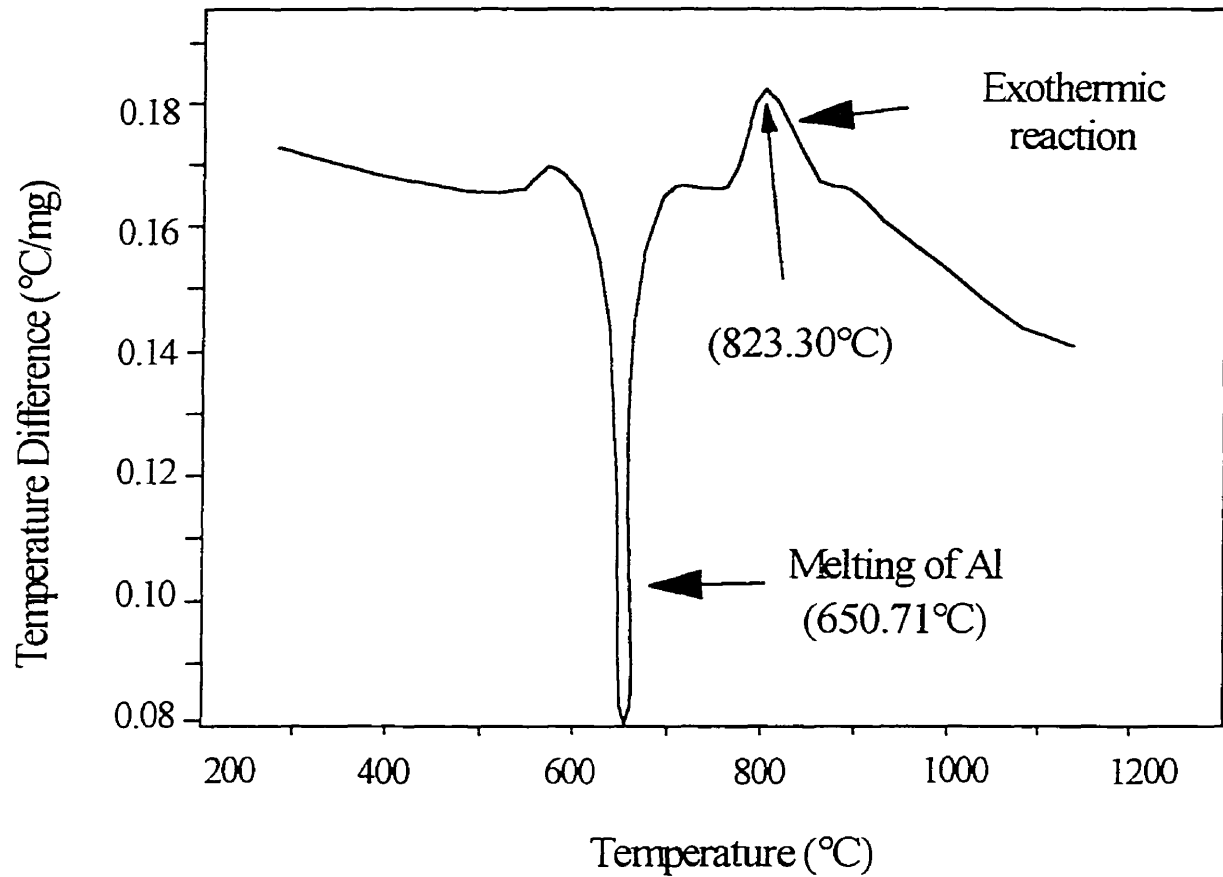


Figure 6. 6 DTA analysis for Al-15%Ti.

The flow of Al on the substrate is desirable to some extent. The flow of Al over Ti particles disperses the intermetallic phases formed at the interface, increasing the concentration gradient at that interface and resulting in accelerated diffusion. In fact, the rate of the process is controlled by the ability of the molten metal to carry away the intermetallic phases produced through the reaction between Al and Ti at the interface. Although, a high substrate temperature is desirable for reaction, it limits the coating thickness to about 100 μm . Therefore, only thin foils of the Al-TiAl₃ can be produced through this process.

6.2.2. Casting of Al-TiAl₃ Composites

A typical microstructure obtained through casting an Al-5%Ti alloy is shown in **Figure 6. 7**. This micrograph contains a needle-like morphology of TiAl₃ phase in an Al matrix. The acicular morphology of the intermetallic phase might be questioned since it appears in two dimensions as plates in the microstructure. However, this morphology for the TiAl₃ phase was confirmed by examining the fracture surface where no plates or parts of embedded plates were observed on the fracture surface. Moreover, in the literature, only the presence of needle and blocky morphologies are reported [114]. The needles were found to have an average length of 30 μm and were evenly distributed in the microstructure. No residual Ti was detected in the microstructure indicating that dissolution and reaction was complete.

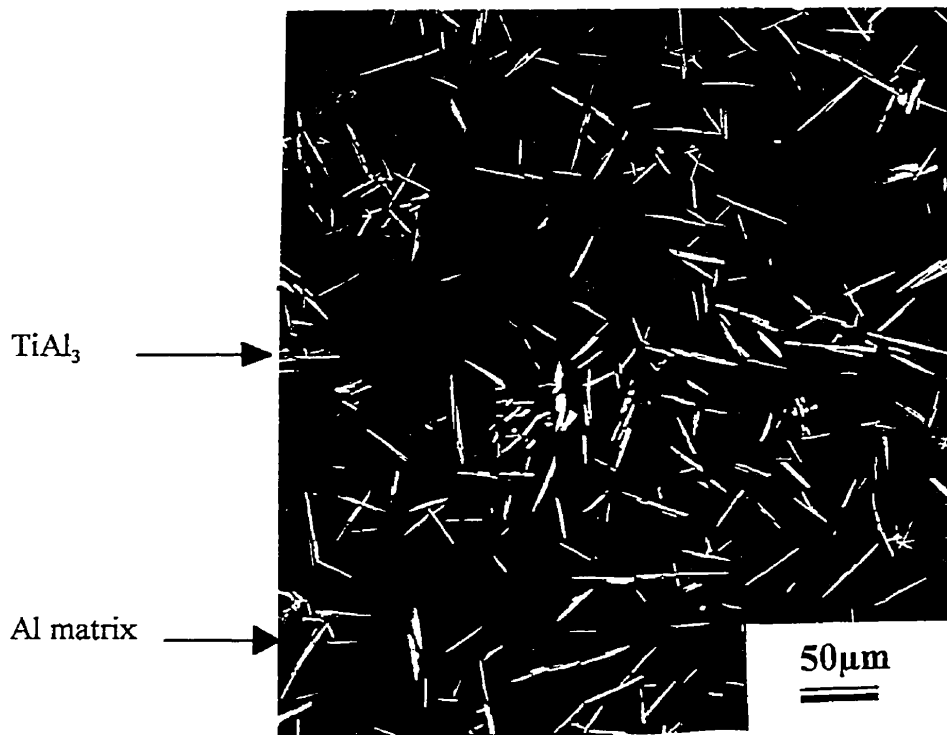


Figure 6. 13. Typical microstructure (5 wt.%Ti) obtained from casting in water-cooled copper mould.

This microstructure would not offer high mechanical properties since the long and sharp needles would act as stress raisers causing premature crack initiation under tensile stresses. In contrast, it may represent high wear resistance at high temperature. However, further analysis will be required to determine the performance of this microstructure.

The quantitative EDS analysis showed that the intermetallic phase contains 27 at.% Ti and 73 at.% Al. This composition is close to that of stoichiometric TiAl₃. This phase precipitates from high temperatures (from 1300°C down to 660°C) depending on the Ti content of the melt. In this range, the liquidus temperature of Al alloys sharply increases with small increases in the Ti contents, i.e., a 2 wt.% Ti addition increases the liquidus temperature to above 1000°C. This rapid increase in the liquidus temperature lowers the casting characteristics of this series of Al alloys. The solidification ranges are between 450 and 700°C for Al alloys containing 5 to 15 wt.% Ti, respectively. The longer the solidification range the more difficult is the feeding of molten metal between solid dendrites, resulting in high shrinkage porosity and coring. These alloys also need to be cast at higher temperatures which cause casting problems such as an increase in oxide content of the melt. In addition, as the Ti content increases, the reactivity of the Al-Ti alloys increases, thus limiting the use of conventional furnaces, crucibles, ladles, and moulding materials.

6.2.3. Powder Metallurgy of Al-TiAl₃ Composites

Typical microstructures obtained from this process for a 10 wt.% Ti are illustrated in **Figure 6. 8**. There was no significant change in the size of the TiAl₃ particles sintered at 600°C and 700°C. In contrast, the TiAl₃ particles of the composites sintered at 1100°C were much coarser than the other microstructures, see **Figure 6. 9**. The coarsening of the intermetallic phase can be explained by the dissolution of fine particles and re-precipitation of the larger ones. Above 700°C, liquid phase sintering is the dominant process responsible for coarsening, since the formation of a liquid Al-phase would facilitate mass transfer.

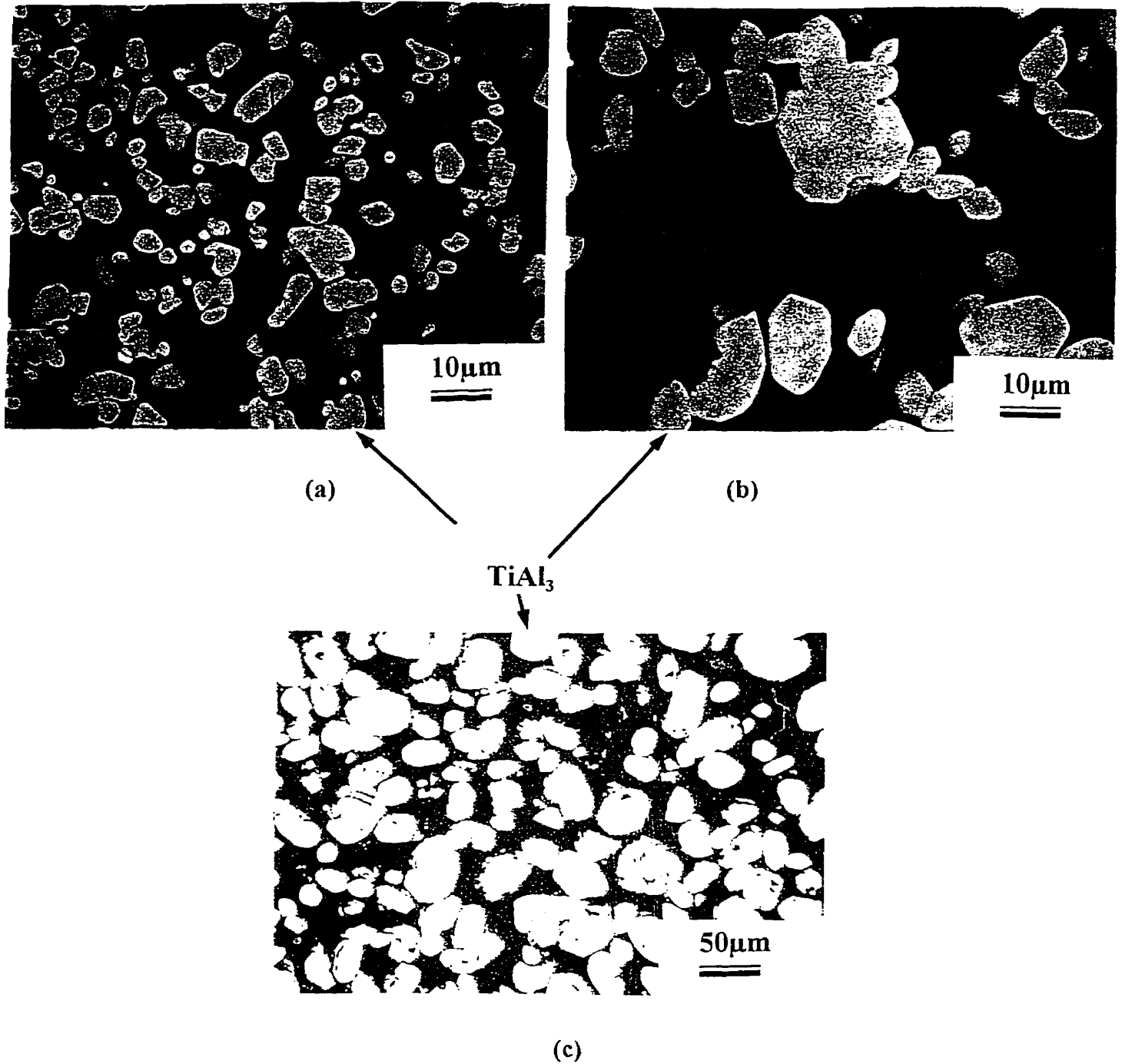


Figure 6. 8. Typical microstructures of composites containing 10 % Ti sintered at (a) 600°C, (b) 700°C and (c) 1100°C for 30 minutes.

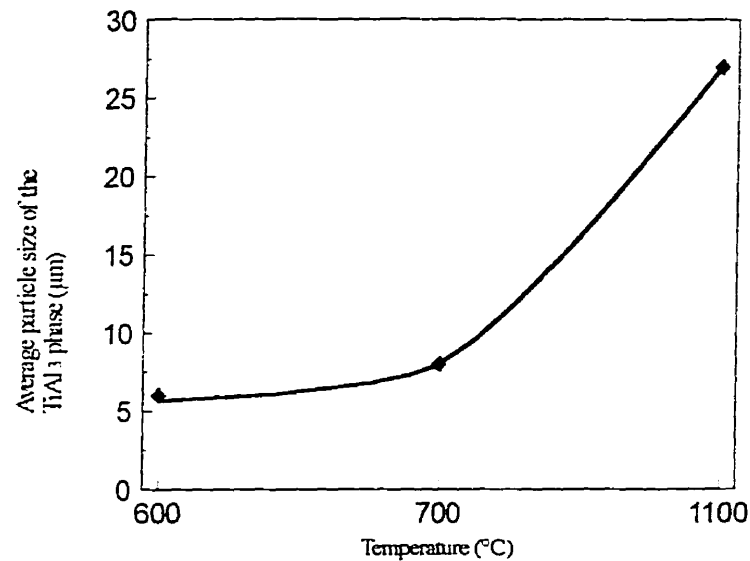


Figure 6. 9 The effect of sintering temperature on the TiAl₃ particle size of a composite containing 10 wt.% Ti.

Cracking and separation of intermetallic phases were observed for all samples, and increased with sintering temperature. Samples sintered at 1100°C presented the largest number of cracks. This may be attributed to the differences in coefficient of thermal expansion (CTE) of the Al-matrix and that of the intermetallic phase¹. The presence of these microcracks in TiAl₃ microstructure has been previously reported, although no explanation for their formation has been given [115].

The TiAl₃ phase appears as particulates in the Al-matrix, but with a different morphology to that observed for cast microstructures. This difference can be explained by the different mechanism of formation of TiAl₃. During casting, the intermetallic phase precipitates at high temperature from a liquid phase which is very fluid. In contrast, in powder metallurgy, the intermetallic phase is formed because of diffusion and reaction between solid Al and Ti powders which is a much slower mass transport mechanism than occurs during solidification.

¹No data has been found for CTE of TiAl₃ so far.

powders which is a much slower mass transport mechanism than occurs during solidification. Moreover, due to the stirring effect of the induction furnace used for casting, the saturated liquid Al at the interface of molten Al and Ti particles is readily dissolved in the bulk Al, therefore, TiAl₃ grows in a less saturated environment than that of powder metallurgy.

The average size of TiAl₃ particles was finer than the size of Ti powder (60 μm) used in the mixture. The average particle sizes for the composites, containing 10 wt.% Ti, sintered at 600 and 700°C were 6 and 9 μm, respectively. This observation can be explained by (a) the formation of the intermetallic phase at the interface between Al and Ti, (b) a breakdown of the intermetallic phase and (c) a redistribution of this phase in the Al matrix. The breakdown of the intermetallic phase at the interface can be explained by both the CTE mismatch between Al, Ti and TiAl₃, and a dissolution of this intermetallic phase in the liquid Al. This mechanism can be better explained by referring to the SEM micrograph shown in **Figure 6.4**, where the formation of TiAl₃ phase at the interface and its breakdown to smaller particulates is clearly evident. This microstructure has been obtained through plasma spraying of an Al and Ti mixture on a substrate preheated to about 300°C. The beauty of this microstructure is that it shows the process arrested before completion of the reaction and precipitation.

The formation of a finer intermetallic phase in the Al matrix can be explained by two possible mechanisms: firstly, the irregular dendritic shape of the Ti powder, (see **Figure 4.6**), which contains small branches. These can be easily broken down, separated from the main body and provide a finer particulate in the matrix. Secondly, the exothermic reaction which occurs between Al and Ti (**Figure 6.6**) provides a local region of molten material at the interface that can carry away the intermetallic particles and redistribute them in the matrix.

The morphology of the aluminide phase in the Al-TiAl₃ composites is determined by the process used to produce this material. For a needle-like structure, the Ti must be added to the

from a source of Ti in the presence of a melt saturated in Ti. This occurs at temperatures where the solubility of Ti in the melt is small; i.e., < 900°C [6.114].

6.2.4. Reactive Hot Isostatic Pressing (RHIPping)

In brief, the HIP process involves sealing metallic powders, under a vacuum, in a metal or a glass can, which is then subjected to both heat and pressure resulting in a dense part. HIPping is used as a consolidation technique for the near-net-shape production of advanced materials. In RHIPping, a reaction is also involved between the canned powder mixture resulting in the formation of new compounds. This process was very attractive for the production of Al-TiAl₃ since the high pressure (200 MPa) applied to the powder mixture guarantees an intimate contact between Al and Ti powder particles. Therefore, a higher mass transfer rate is expected with the RHIPping process. In addition, the parts produced through this process are dense and the mechanical properties can be assessed without the influence of the secondary factors such as porosity and porosity distribution in the consolidated parts.

6.2.4.1. RHIPping Temperature

The HIPping temperature was found to be the most important factor in the production of Al-TiAl₃ composites. The critical HIP temperature is the melting point of Al. Cans HIPped below the melting point of Al showed a microstructure of an Al matrix containing Ti particles reacted only on the surface to form a thin layer of TiAl₃. It is believed that the exothermic reaction between Al and Ti increases the local temperature at the Al/Ti interface. Most of the heat generated is consumed by the latent heat required for melting the adjacent Al. Therefore, a local melting of Al occurs and the TiAl₃ phase partially dissolves in the Al forming discrete particles. The formation of discrete TiAl₃ particles can also be explained by the volume increase (23%) encountered with the formation of the new phase (TiAl₃) compared to the original Ti [116]. In addition, because of the exothermic reaction at the interface, a temperature gradient is established as being highest at the interface but decreases laterally. The temperature gradient fractures the interface and the intermetallic layer due to the CTE mismatch between the Ti core and the intermetallic layer.

As the reaction proceeds, the formation of the intermetallic shell around the Ti particles acts as a diffusion barrier and slows the mass transport of Al to the unreacted Ti. Finally, at equilibrium, the rate of heat generation by the reaction equals the rate of heat loss to the surroundings. Al begins to solidify and the reaction slows down. A typical micrograph of a sample RHIPped at 600°C for one hour showing the formation of TiAl₃ phase at the interface is displayed in **Figure 6. 10**.

RHIPping at a temperature above the melting point of Al accelerates the TiAl₃ formation kinetics. Molten Al gradually dissolves the Ti from the TiAl₃ layer surrounding the Ti core. Since mass transport in the liquid phase is faster than the solid phase, the Ti concentration in the molten Al adjacent to the intermetallic phase is quickly depleted. This results in a steeper concentration gradient and a faster dissolution rate of Ti from the intermetallic layer into the

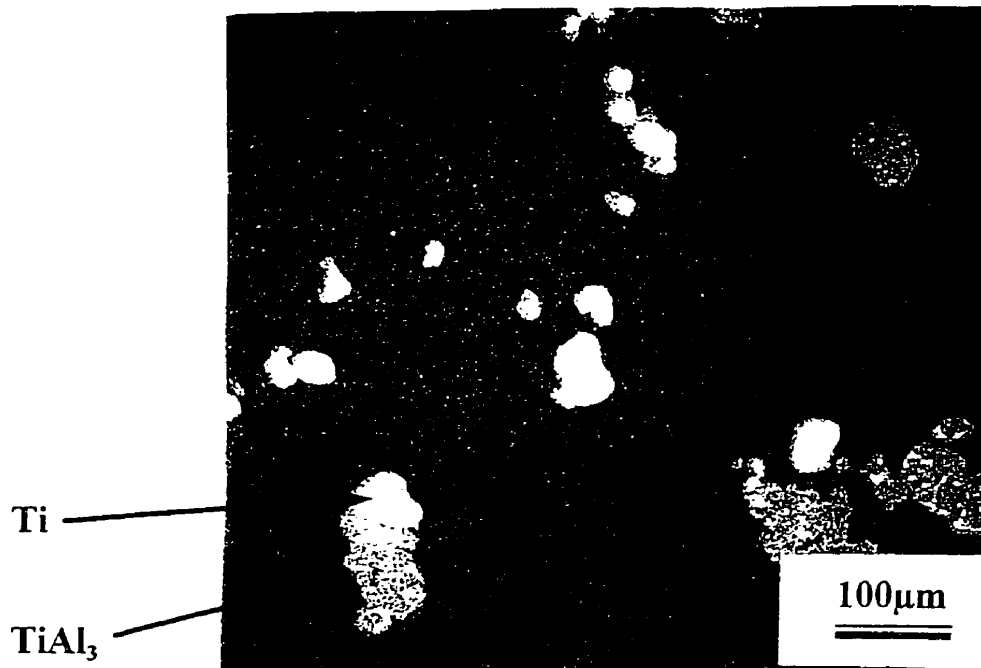


Figure 6. 10 Microstructure of a Ti particle reacted on the surface forming TiAl₃ phase.

molten Al. Furthermore, the reverse diffusion, i.e., diffusion of Al through the intermetallic layer accelerates at higher temperatures. RHIPped samples consolidated above the melting point of Al for as little as 0.5 hr. showed complete dissolution of Ti particles in molten Al. A typical microstructure is shown in **Figure 6. 11**. The growth of the intermetallic layer as a function of time and temperature is shown in **Figure 6. 12**. These data represent the growth of the intermetallic layer both below and above the melting point of Al. The growth of the intermetallic layer at high temperatures is rapid resulting in convergence of the curves. It would have been preferable to present these data separately since Al melts at 660°C and a major change in mass transport is observed. This would have required an extensive series of experiments below and above 660°C, which were beyond the scope of this study.

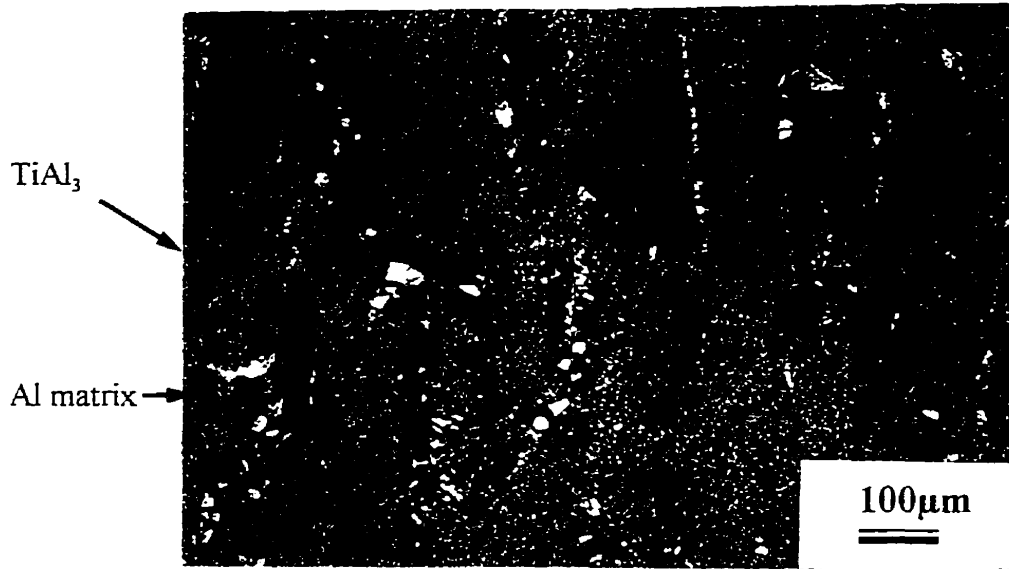


Figure 6. 11 A typical microstructure of the RHIPped samples consolidated at 700°C for 10 min.

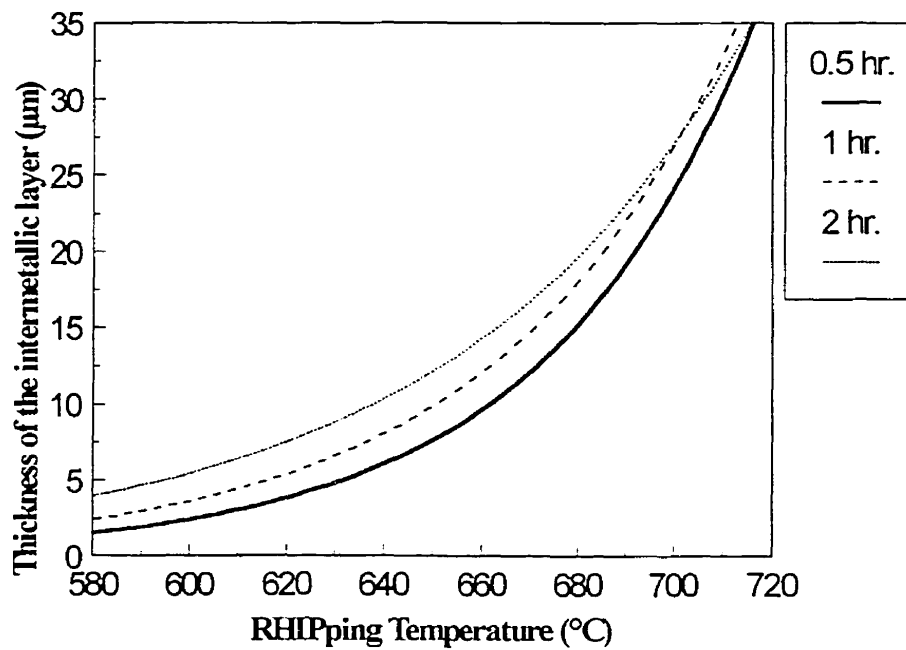


Figure 6. 12 The growth of the intermetallic layer as a function of time and temperature.

The reaction rate above the melting point of Al was so fast that even at 0.5 hr. holding at 670°C the reaction was complete. However, the growth of the intermetallic layer below the melting point of Al was slow and measurable. Therefore, the growth of the intermetallic layer was studied below 660°C and is shown in **Figure 6. 13** for various temperatures. In order to obtain the activation energy for the growth of the intermetallic layer, the slopes of the lines ($\ln k$) in **Figure 6. 13** were plotted versus $1/T$ in **Figure 6. 14**. The activation energy for the growth of the intermetallic layer was found to be 116 kJ/g mol which is in good agreement with Mackowiak *et. al.*'s[117] work which resulted in an activation energy of 121 kJ/g mol.

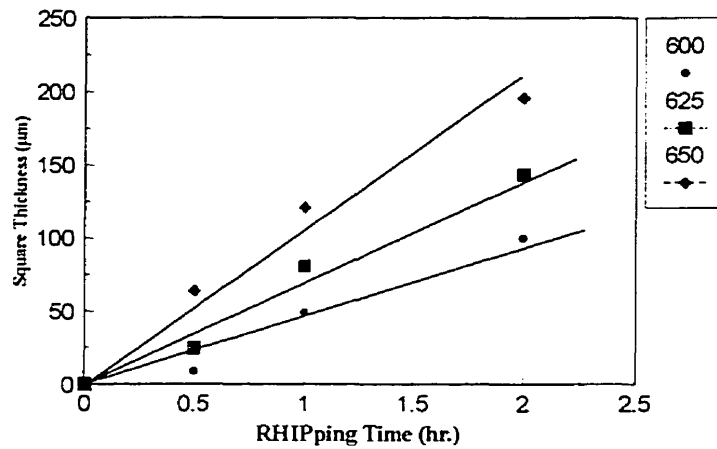


Figure 6. 13 Thickness of the intermetallic layer as a function of RHIPping time.

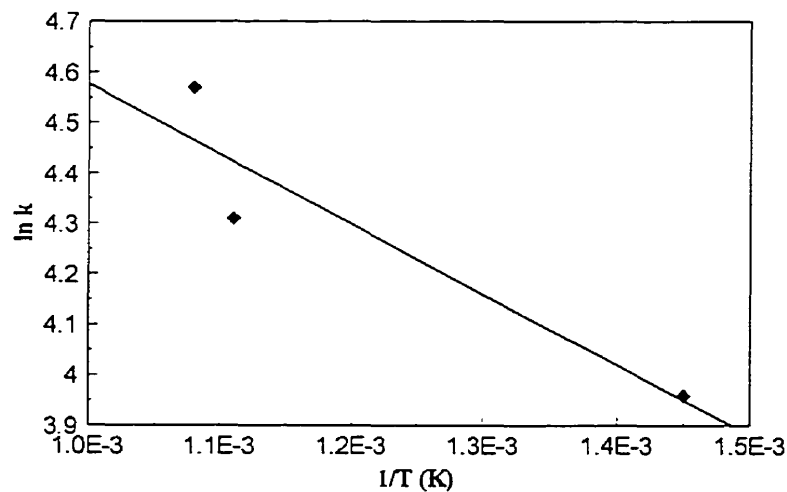
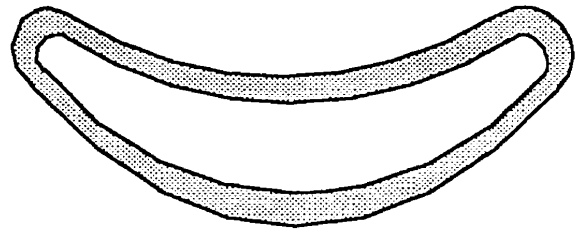


Figure 6. 14 Growth rate of the intermetallic layer as a function of temperature.

Two major technical problems were experienced with HIPping above the melting point of Al. The first was deformation of the cylindrical canning tube to an oval shape during processing, as shown in **Figure 6. 15**. The unexpected large amount of deformation was attributed to the low tap density (48%) of the powder mixture in the can. The low tap density was due to the irregular shape of the powders of both Ti and Al. Generally, spherical powders are used for HIPping since they result in a tap density of about 65%. The tap density of the mixture was increased to 55% by die pressing the powder mixture inside the can however, no change was observed in the ovality of the can. It was then decided to machine flat tensile specimens directly from the oval shape.



The second was a problem associated with the reaction between molten Al and the can

material itself. Originally stainless steel (SS) **Figure 6. 15** Final shape of the HIP can was used and severe reaction was observed after HIPping.

at the interface of the SS and the HIPped sample. Elongated complex intermetallics also were observed in the microstructure which were very similar to those observed for the vacuum plasma sprayed material on SS substrates illustrated in **Figure 6. 1**. Therefore, Ti tube was selected then used and only a very thin reaction layer was observed at the interface between the can and the RHIPped sample, which was removed by grinding prior to hot rolling.

6.3. Reactive Plasma Spraying

In all of the processes discussed above, elemental powder of Ti was used as the starting material. In this section, the production of Al-TiAl₃ composites through reactive plasma spraying will be examined. The original idea was to use TiCl₄ as Ti source instead of elemental Ti metal and react it with molten Al to produce Al-Ti intermetallics. The advantages of using TiCl₄ are: (a) it easily boils at 138°C enhancing the reaction kinetics with Al; and (b) it is more economical than elemental Ti powder. TiCl₄ cost \$2/kg whereas Ti powder is typically \$250/kg; this makes the process commercially very attractive. This concept provides unique capabilities since it combines several metallurgical processes, the reduction of Ti from TiCl₄, alloying, rapid solidification and spray forming in one single step.

Up to now, the idea of reducing TiCl₄ by Al has two approaches. The first was undertaken by Sale[118] who studied the reaction between TiCl₄ and molten Al. The products of this approach were then investigated based on the effects of the temperature, time and partial pressure of the TiCl₄. It was found possible to produce intermetallic compounds ranging from TiAl₃ to Ti₃Al at temperatures ranging from 700°C to 950°C using different TiCl₄ partial pressures. A wide range of morphologies were reported for the products, ranging from a needle-like growth for Ti₃Al to fine particulates of TiAl₃.

The other approach is using plasma. The feasibility of this concept was evaluated by Tsantrizos[119] who injected the Al powder and TiCl₄ into a D.C. plasma torch with the reaction taking place in the tail flame of the plasma flame. This process is called REactive plasma FORMing (REFORM). The products were found to contain up to 85 wt.% Ti depending on the plasma conditions and Al/Ti molar ratio[120]. The resultant microstructures were reported to contain intermetallic phases, with morphologies ranging from needle-like to spherical particulates corresponding to increasing the Ti content in the Al matrix.

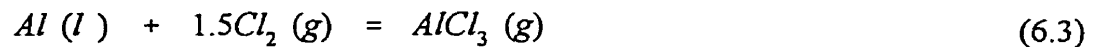
Thermodynamics of Al-TiCl₄ system

Several years ago, Kroll and Hunter introduced the use of metallic reducing agents (Mg and Na) for the extraction of Ti and Zr from their volatile tetrachlorides [121],[122]. One requirement for the metallic reducing agent is that it forms a more stable chloride than tetrachlorides. This can be easily determined using Ellingham diagram for chlorides [123]. The other is the immiscibility of the chloride by-products in the metal product.

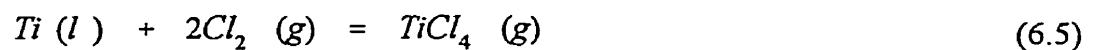
This concept can also be applied to Al-TiCl₄ system. The standard free energies (J) of AlCl₃, AlCl₂, TiCl₄ and overall reaction (see Equation 6.1-6.7), per gram-mole of chlorine, occurring between Al and TiCl₄ are represented in **Figure 6. 16**[124]. The temperature of these reactions (in plasma) are assumed to be 2000°C. It can be seen that Al can reduce TiCl₄ since its chlorides (AlCl₂ and AlCl₃) are more stable than TiCl₄ above 600°C.



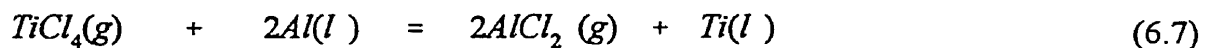
$$\Delta G^0_R = -338016.51 - 9.50 T \quad (6.2)$$



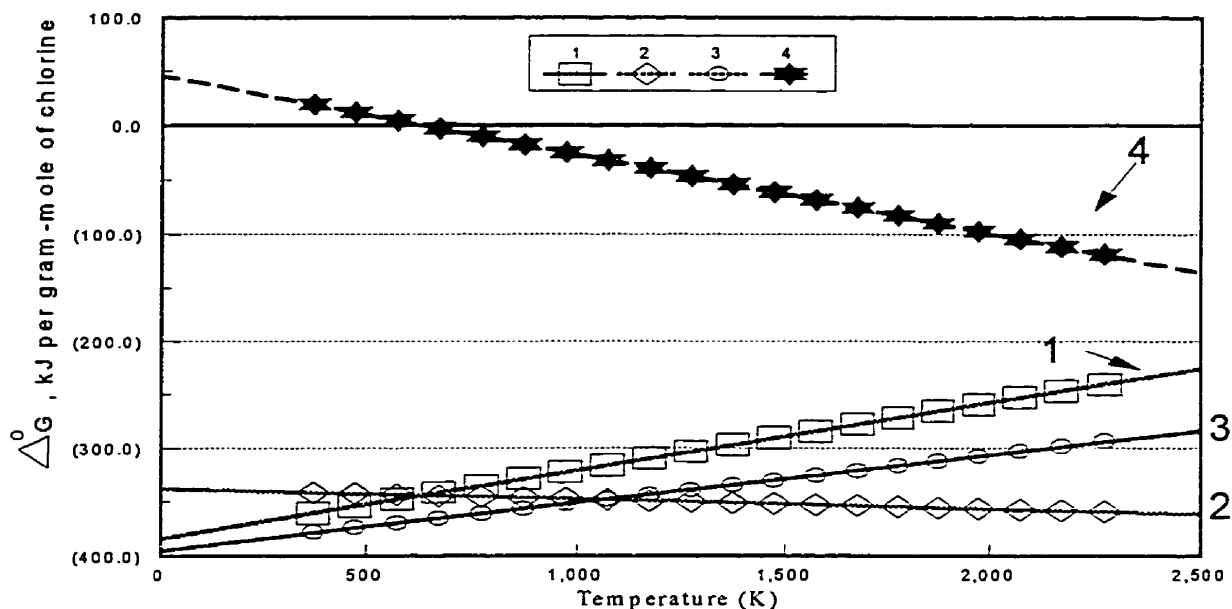
$$\Delta G^0_R = -587854.8 + 29.51 T + 10.46 T \log T \quad (6.4)$$



$$\Delta G^0_R = -771245.4 + 152.47 T - 7.54 T \log T \quad (6.6)$$



$$\Delta G_R^0 = 95212.38 - 171.625 T + 7.87 \log T \quad (6.8)$$



1. $\text{Ti (l)} + 2\text{Cl}_2 \text{ (g)} = \text{TiCl}_4 \text{ (g)}$
2. $\text{Al(l)} + \text{Cl}_2 \text{ (g)} = \text{AlCl}_2 \text{ (g)}$
3. $\text{Al (l)} + 1.5 \text{Cl}_2 \text{ (g)} = \text{AlCl}_3 \text{ (g)}$
4. $\text{TiCl}_4 \text{ (g)} + 2\text{Al (l)} = 2\text{AlCl}_2 \text{ (g)} + \text{Ti (l)}$

Figure 6.16. The standard of free energies of Al-chlorides and overall reaction as a function of temperature.

According to Equation 6.7, TiCl_4 is reduced by metallic Al to form Ti and AlCl_2 . However, interesting industrial possibilities arise if Al is supplied in excess and is allowed to react with the Ti obtained by the reduction of TiCl_4 . Therefore, the final product will be an alloy in the Al-Ti system. This product can then be collected as powder for further processing powder metallurgy, sprayed as a coating or used as an Al-Ti master alloy in Al casting.

Using the FACT equilibrium program, the chemical equilibria of the TiCl₄-Al system were investigated at various temperatures (from 1000 to 2000 K) and a constant pressure (1 atm.), as shown in **Figure 6. 17**. From the preliminary microstructural analysis it was found that more than 90% of the Al particles achieved a temperature between 1000 and 2000 K (discussed in details in § 6.3.2.2.).

At high temperatures, the production of Al chlorides with low Cl/Al ratios (such as AlCl and AlCl₂) are promoted. It shows that a higher Al is consumed for the reduction of every mole of TiCl₄. In practice, forming Al chlorides with higher Cl/Al ratios is desirable (such as AlCl₃) since a lower Al will be required for full reduction of TiCl₄. It can also be seen that at low reaction temperatures (i.e., 1200 K), TiAl forms while at high reaction temperature (1800 K) Ti is produced. In contrast to the results of the thermodynamics predicting the formation of TiAl at low reaction temperatures, the microstructural analyses of the product showed that TiAl₃ is the dominant phase. Finding experimentally which phase forms first requires a series of reaction tests followed by rapid quenching. However, due to the high Al concentration on the surface of the molten Al droplet, and according to the Al-Ti phase diagram (see §

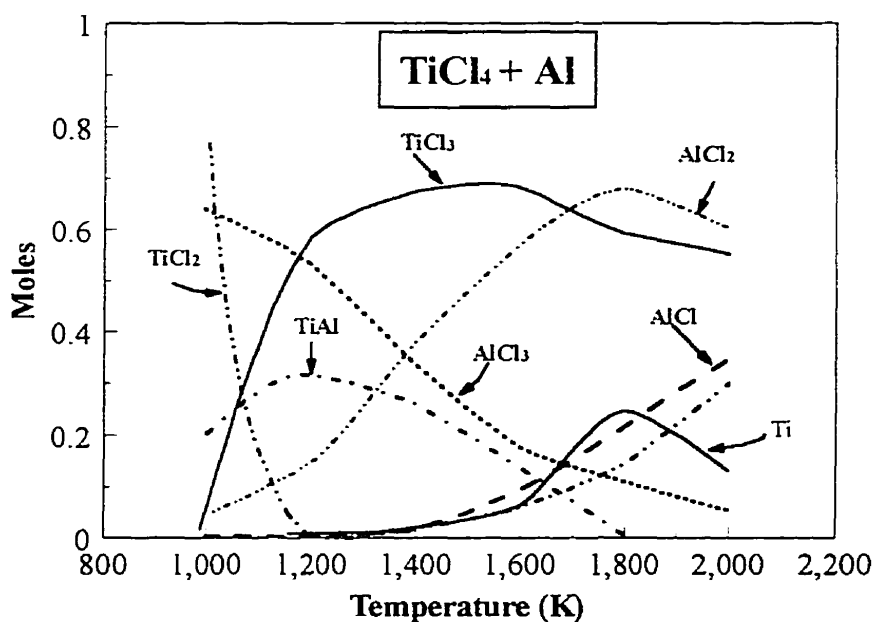


Figure 6. 17 Chemical equilibrium of Al-TiCl₄ system as a function of temperature (the presence of species with a concentration lower than 10⁻² are not shown).

the surface of the molten Al droplet, and according to the Al-Ti phase diagram (see § 6.3.2.1), TiAl₃ forms despite the chemistry of the phases formed through the Al-TiCl₄ reaction. In fact the reaction between TiAl₃ and TiCl₄ should be investigated, since below 1600 K TiAl₃ forms on the surface of the molten Al resulting in a solid outer shell and isolating the core from further reaction with TiCl₄. The results of the thermodynamic study on the TiAl₃-TiCl₄ reaction are shown in **Figure 6.18**. By increasing the reaction temperature, less TiCl₃, higher Ti, and AlCl are produced. Again, it is shown that at low temperatures TiAl is more stable than TiAl₃. Above 1600 K, TiAl₃ melts and forms a Ti-Al melt. It is believed that this temperature is a breakthrough in the TiAl₃-TiCl₄ reaction since above this temperature, molten Al-Ti reacts with TiCl₄ and is expected to have a higher reaction rate.

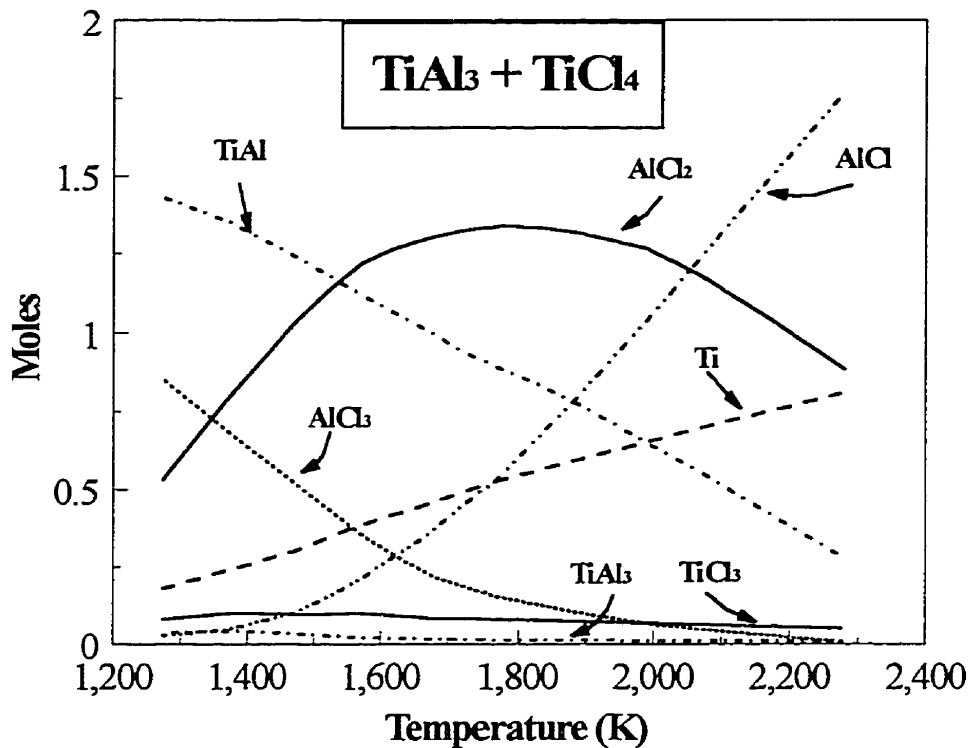


Figure 6.18. Moles of the products in TiAl₃-TiCl₄ reaction at equilibrium and various temperatures (the presence of species with a concentration lower than 10⁻² are not shown).

6.3.1. Single Plasma Torch

Al-TiAl₃ materials were produced through reactive plasma spraying using a single plasma torch. Al powder and TiCl₄ vapor were injected into the plasma jet at the plasma torch exit using argon as the carrier gas. The products of the reactive plasma spraying were collected both as a deposited layer and powder. The schematic of the process was shown in **Figure 4.4**. Various microstructures were obtained throughout this process. The best microstructure of the reactively formed Al-TiAl₃ composite is shown in **Figure 6. 19**. Only 15% of the deposit volume contained such a microstructure. The backscatter electron image shown in this figure reveals two major phases, a light and a dark gray phase. EDS analyses showed that the bright phase contains 25 at.% Ti and 75 at.% Al which corresponds to the composition of TiAl₃. The even distribution of the fine (~ 1 μm) intermetallic particles in an Al-matrix may result in a good ductility. This illustrates the strong potential of reactive plasma spraying to

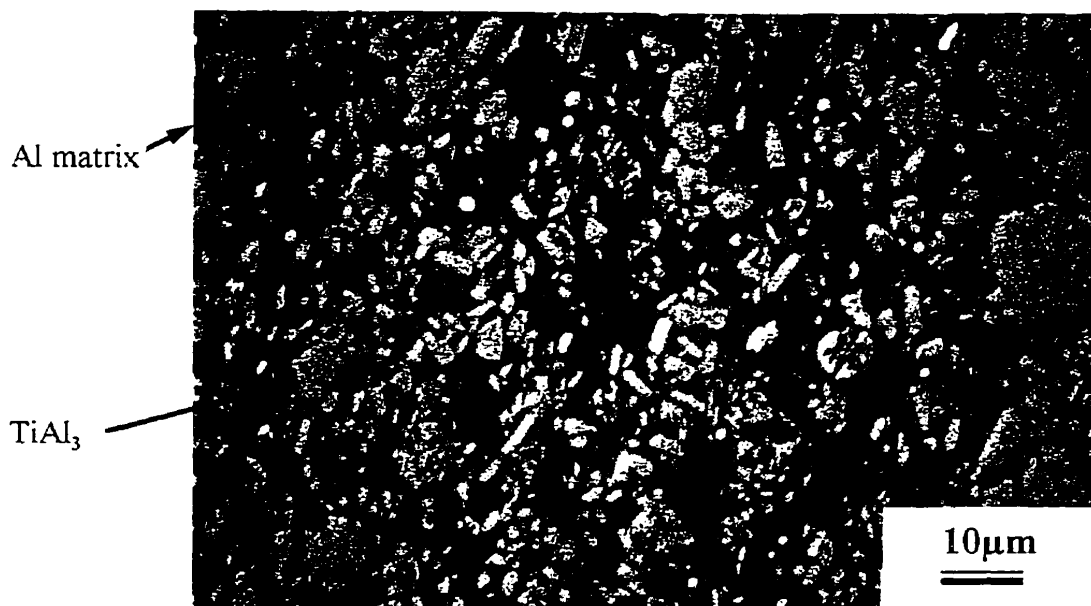


Figure 6. 19 Microstructure of the Al-TiAl₃ composite produced through reactive plasma spraying.

overcome the low ductility of the Al-TiAl₃ composites. The results of EDS analysis also revealed the presence of chlorine on the flat surface of the powders. In contrast, no chlorine was detected in the cross-section of the powders. This implies that chlorine might only be surface contamination. The chlorine content was also quantitatively analyzed by ICP-AES (Inductively Coupled Plasma-Atomic Emission Spectrometry) and was found to contain 1.5 at.% chlorine.

6.3.1.1 Thermogravimetry Analysis

Chlorine in the composite material can be either chemically bonded to Al and Ti or physically adsorbed on the surface of the particles. In the former case, selection of the dechlorination procedure strongly depends on the physical and chemical properties of the chloride compounds. None of the Al and Ti chloride compounds are stable above 660°C. Based on this fact, heat treatment of the chlorine contaminated composite in this temperature range should remove all traces of chlorine. The results of the TGA confirmed this fact, as shown in **Figure 6. 20**. The TGA represents three distinct events which can be described as follows:

- The first event occurs at 70°C when the rate of weight loss slows. This temperature is close to the melting point of aluminum per-chlorate, [Al(ClO₄)₃].6H₂O].
- The second event occurs at about 100°C. It is very close to the temperature at which aluminum chloride hexa-hydrate, [AlCl₃.6H₂O], decomposes through a dehydrolysis reaction.
- The third event occurs at about 120°C and finishes at about 170°C. This temperature is close to the boiling point of aluminum chloride (AlCl₃).
- The final event is over the range 250-625°C where the weight loss can be attributed to evaporation and dissociation of titanium chlorides (e.g. TiCl₂ or TiCl₃) [125].

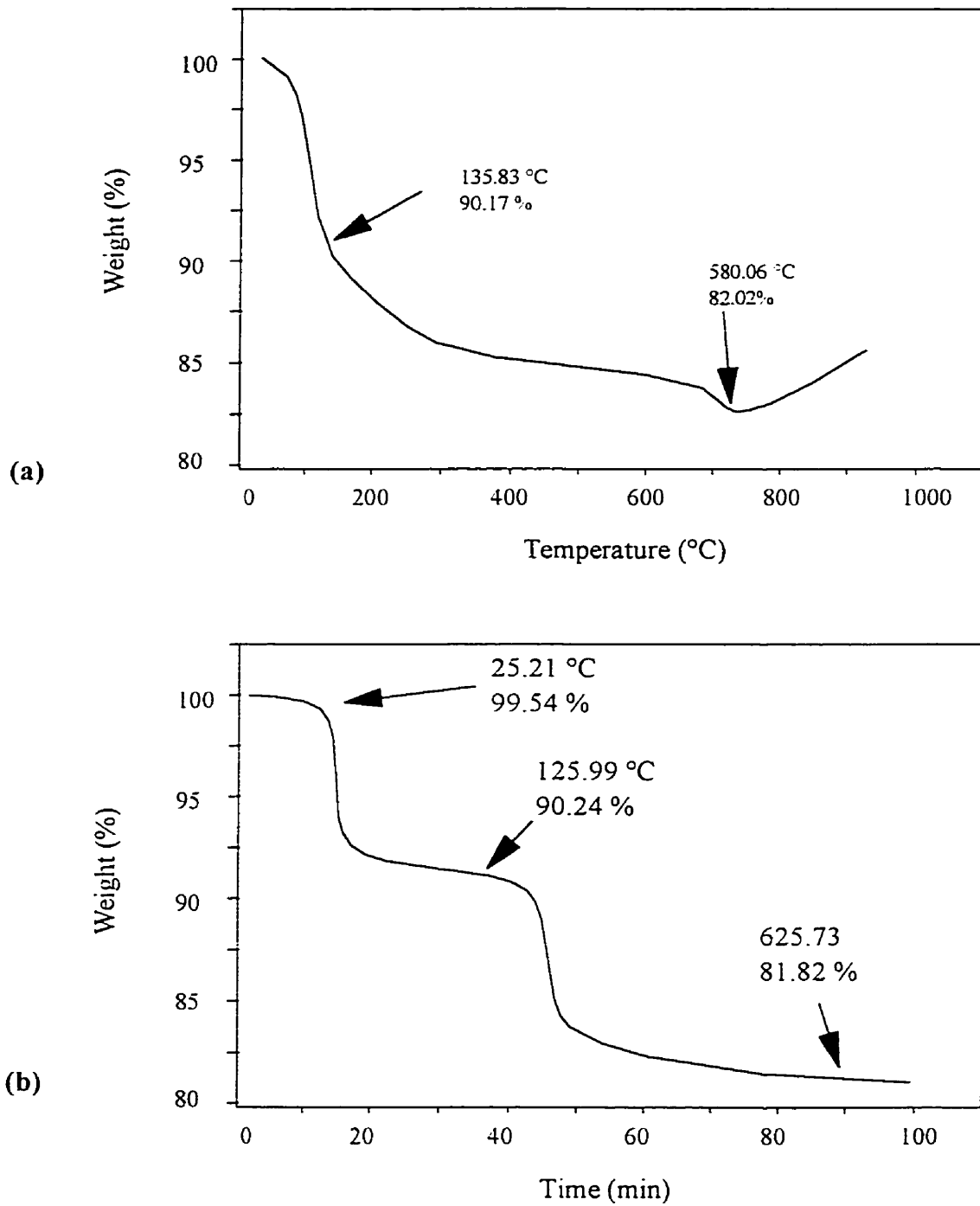


Figure 6. 20 The results of TGA performed on reactively formed composites contaminated with chlorine. Weight changes versus (a) temperature and (b) time.

For a few reacted powder particles, the intermetallic phase was observed only formed on the surface of the Al powder, see **Figure 6. 21**. It can be seen that the reaction between Al and TiCl₄ initiates at the surface of the Al and proceeded inward although not to completion. Forty percent of the Al particles produced similar microstructures and the remaining deposit on the surface of the substrate remained unreacted forming the Al matrix, as shown in **Figure 6. 22**. Obviously, a uniform distribution of the intermetallic phase is desirable for the final product. Uniform particle reaction and mixing depend on particle temperature. Treating individual particles evenly is almost impossible due to the intrinsic presence of temperature and velocity gradients in the plasma jet. An attempt to improve the product by parametric variation of: Al carrier gas, plasma power, and Al/TiCl₄ feed ratio did not result in an improved product.

The most significant problem associated with single plasma system was the difficulty in maintaining a constant flow rate of Al. Clogging of the injector was frequent due to the sintering of Al powder at the injection point. Many measures such as using gas cooled coaxial tubes, changing the injection position, and increasing the carrier gas flow rate extended the maximum duration of the experiments to only five more minutes. On average, each experiment lasted 15 minutes and was stopped due to clogging of the Al injection port.

Another problem with single plasma spraying was the presence of unmelted particles in the spray deposit. Apparently, some Al powder particles followed arbitrary trajectories in the plasma jet and that resulted in unmelted particles. The unmelted particles do not bond well to other splat formed particles since they are in the solid state when they reach the substrate. Usually, porosity was found next to these unmelted particles and their presence in the deposit are undesirable since they lead to a deterioration of the physical and mechanical properties of the material. From the above results concerning product quality and inability of the process for mass production of Al-TiAl₃, it was decided to use a triple plasma system.

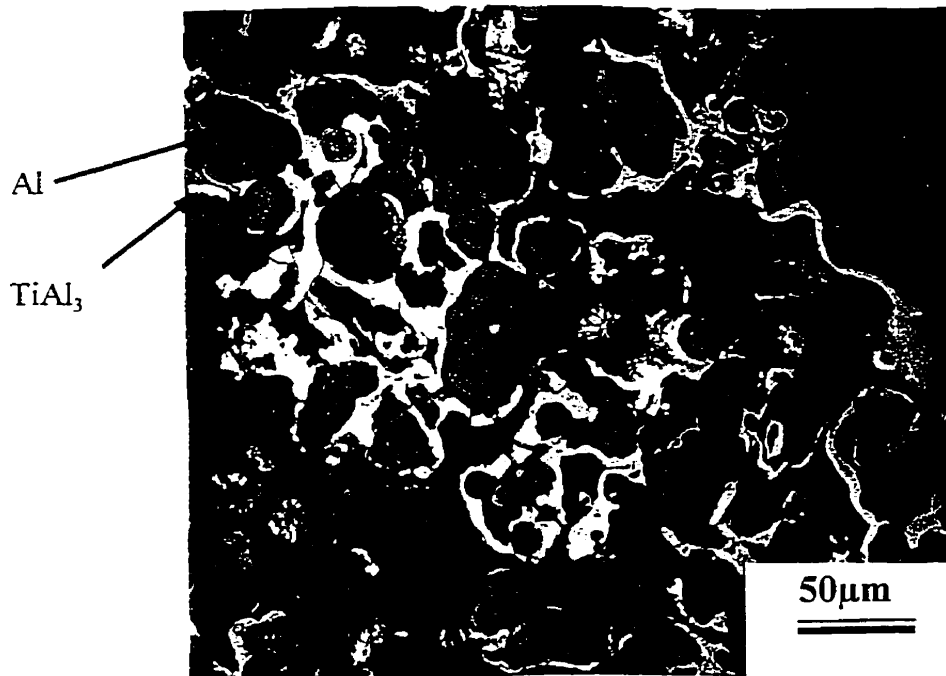


Figure 6. 21 Backscatter image of the reactively formed composite showing that reaction has occurred only on the surface of the powder particles.

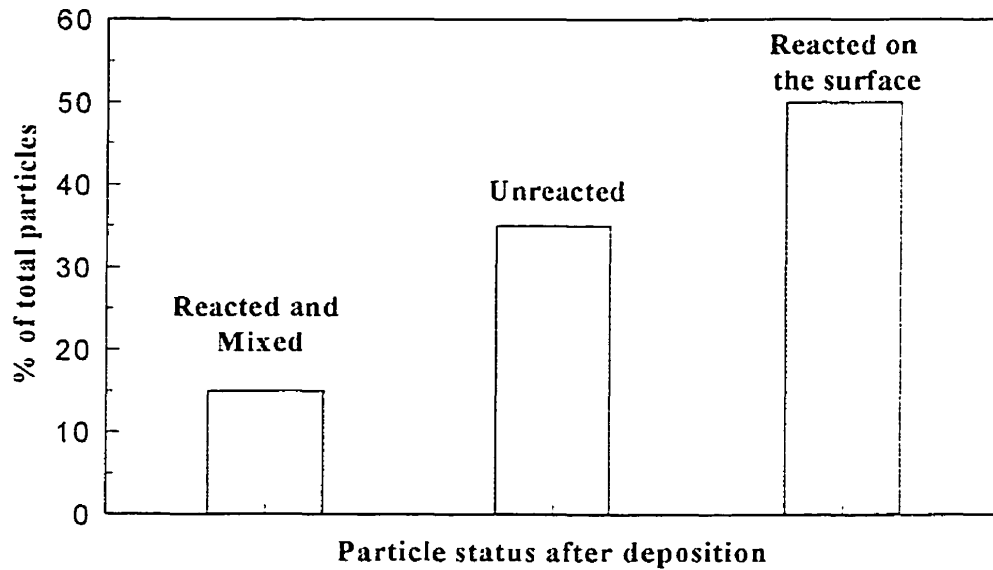


Figure 6. 22 Particle status according to extent of their reaction with TiCl₄. P=20kW, Spray Distance=40cm, Al feed rate=20g/min, TiCl₄= 15mL/min, Al feed carrier gas= 5L/min, TiCl₄ carrier gas= 4 L/min.

6.3.2. Triple Plasma System

The experimental setup for reactive plasma spraying using a triple plasma system was shown in **Figure 4.5**. Al wire is injected into the apex of the system while TiCl₄ is introduced in front of individual torches through the graphite nozzles. The products are collected on the surface of a water cooled substrate. Image analysis was used to measure the Ti content and the distribution of the intermetallic phase across the deposit.

6.3.2.1. Ti Distribution Across the Deposit

A non-uniform distribution of Ti was observed across the deposit, resulting in a low concentration of Ti at the center and a higher concentration in the peripheral region, as shown in **Figure 6. 23**. These results represent the average of four experiments done under the same conditions.

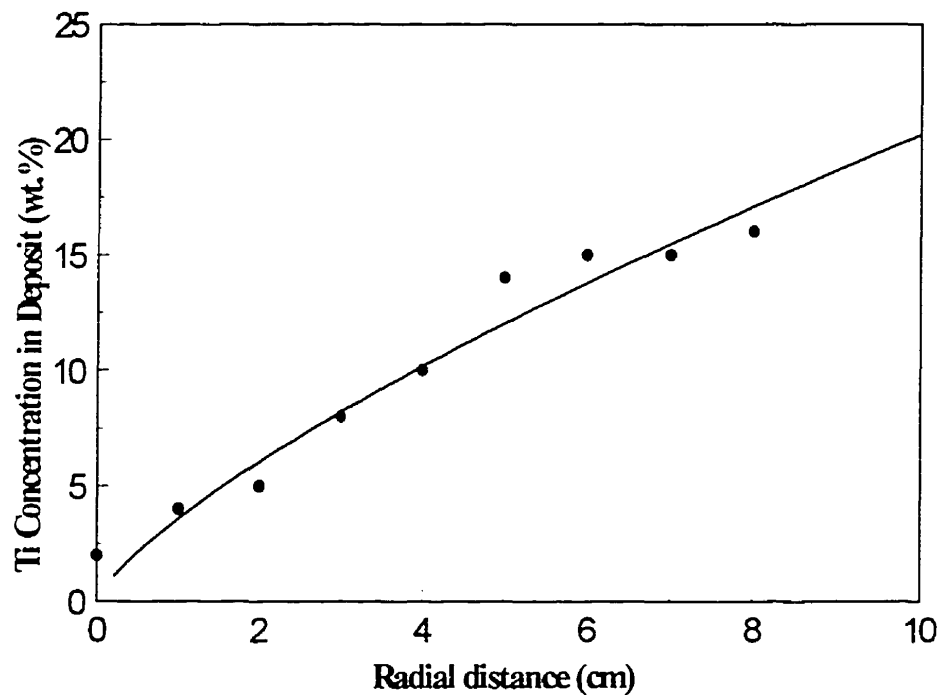


Figure 6. 23 Ti Concentration in the reactively sprayed deposit as a function of distance.

It was proposed that this difference may be due to:

- a) non-uniform mass distribution of reactants (i.g., TiCl₄ and Al) in the reaction region;
- b) particle size difference between the particles travelling in the center and on the periphery;
- c) temperature and velocity differences in the central and peripheral regions.

The hypotheses (a) and (b) were investigated using containers under the atomizer to collect powders which represent atomized powders from the central and peripheral regions of the atomization plume. Powder particles collected from individual containers were weighed and subjected to particle size analysis. The results of mass distribution are shown in Figure 6. 24.

It can be seen that most of the sprayed particles land in the central regions. In other words, the mass distribution across the reaction zone is not uniform and the Al/TiCl₄ ratio varies significantly as a function of distance from the apex. In the central regions, a high Al/TiCl₄ ratio can explain low Ti content in these regions. This is true if we assume that there is a uniform distribution of TiCl₄ across the reaction zone. The same analogy can be used to show a low Al/TiCl₄ ratio in the peripheral regions and therefore, a higher concentration of Ti is obtained.

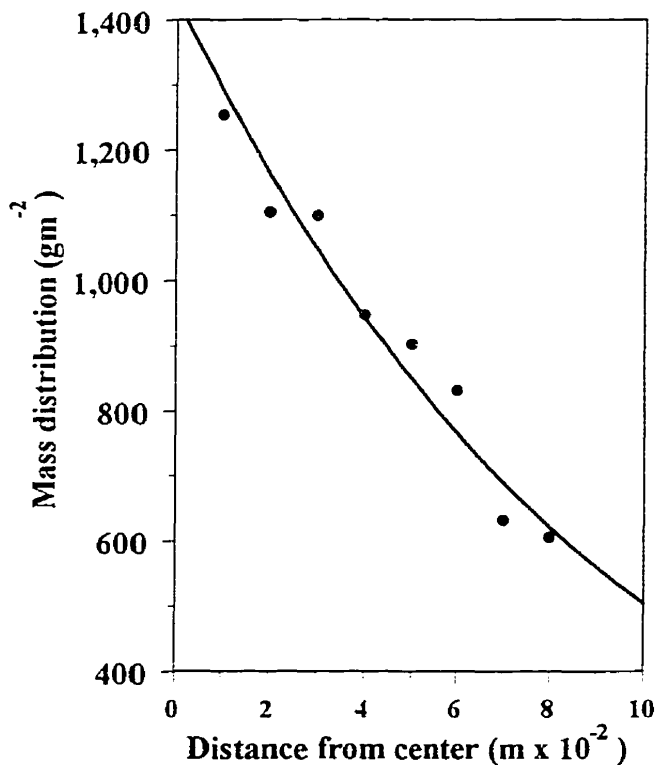


Figure 6. 24 Mass distribution as a function of distance.

The results of particle size distribution from central and peripheral regions are shown in **Figure 6. 25**. The average particle size for the powders which landed in the central region is $82 \pm 1\%$ μm whereas that of the peripheral region is $60 \pm 1\%$ μm . Therefore, the particles moving in the peripheral region are finer and thus reach a higher temperature (compared with coarser particles) due to their smaller mass, assuming a uniform temperature distribution in the system. This results in a high reaction yield and therefore, a higher Ti content in these regions. It is believed that a larger size difference exists between particles in the central and peripheral regions which cannot be measured due to the presence of turbulent flow and vortices in the atomization reactor. The latter mixes the powders from the two regions resulting in false sampling and errors. Klar et al., examined the average particle size as a function of distance from the nozzle center and reported a 100 μm difference in average

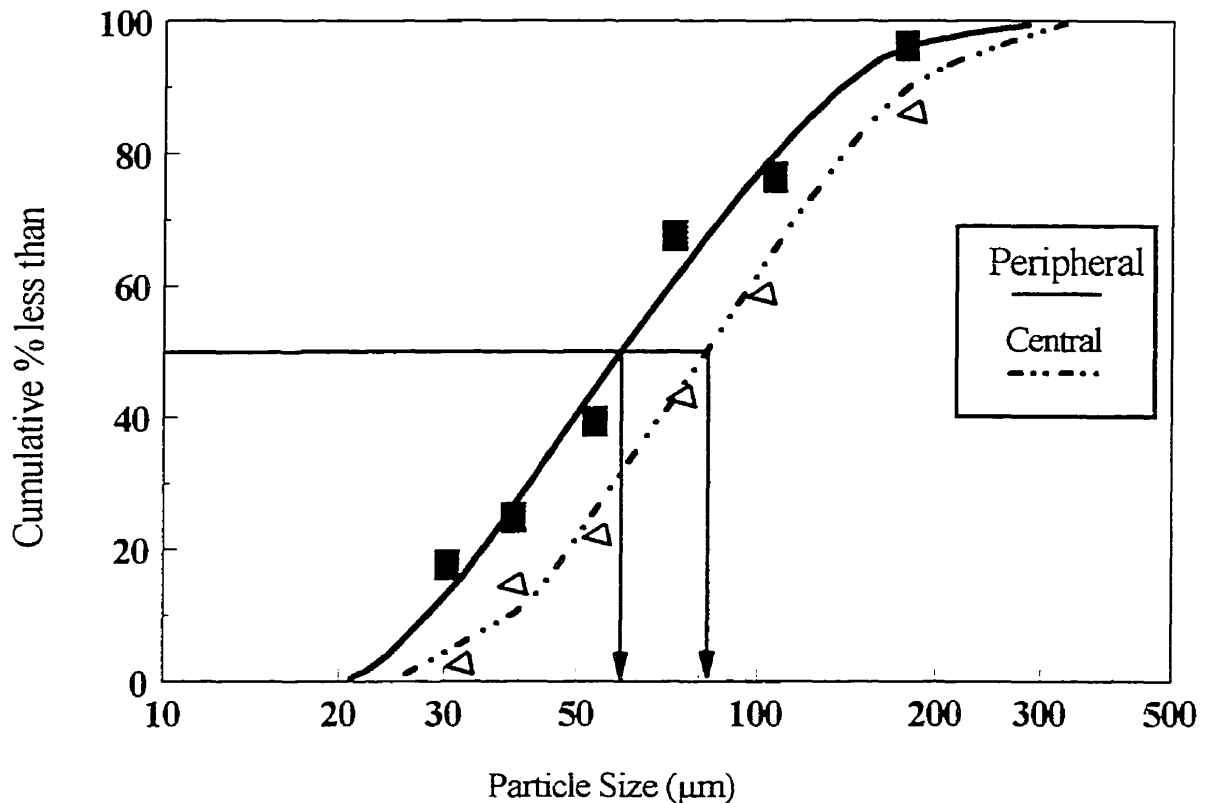


Figure 6. 25 Particle size distribution for powders collected in the central and peripheral regions.

particle size between powders in the central and peripheral regions, i.e. coarser in the centre [126]. Another diagnostic procedure, preferably an on-line method based on image analysis or light detection, [127] should be performed on the atomization plume to increase the confidence level of the above findings. Using these methods, temperature, velocity, and particle diameter can be measured. In addition, the effects of process parameters such as plasma power, Al feed rate, TiCl₄ carrier gas flow rate, and plasma jet accelerating nozzle dimensions can be measured more accurately and optimized on-line. Unfortunately, the complex geometry of the triple plasma system hindered the use of standard equipment. Furthermore, the low emissivity of Al particles limits the use of such equipment.

Hypothesis (c) assumes that in the reaction zone or atomization plume there are temperature and velocity profiles providing atomized powders with different temperature histories. Before discussing the variation of temperature and velocity in the atomization process it is preferable to emphasize on the importance of particle temperature both on its reaction with TiCl₄ and its microstructural development.

6.3.2.2. Microstructural Evolution

The reaction yield of TiAl₃ is determined by the reaction temperature. In other words, the process is temperature controlled. Besides the yield of TiAl₃, the temperature attained by the particles also influence their microstructure. There are four possible thermal histories for Al particles:

- 1) The Al particle may exceed its melting temperature (>660°C), but it may have no TiCl₄ for reaction and such a particle will deposit as pure Al. These particles form the matrix in all of the microstructures shown in this study and the thermal history for this group of particles is represented by case (1) in **Figure 6. 26**. In a single torch reactive plasma spraying, there is a chance that some Al particles may not even melt during the spray process and land on the substrate unreacted;

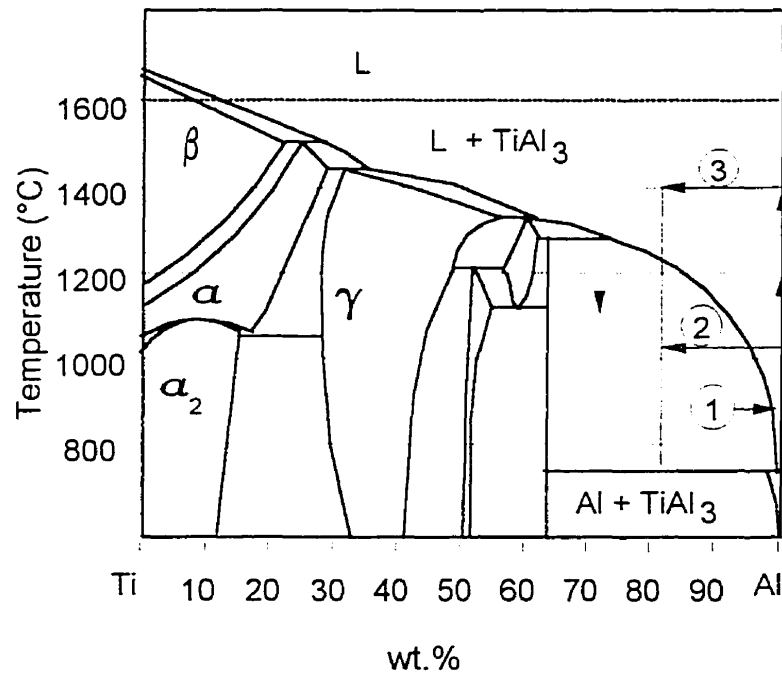


Figure 6. 26 Al-Ti phase diagram with the proposed thermal histories for Al powder particles.

- 2) The particle may be heated above 664°C but lower than about 700°C and react with TiCl₄, forming a solid layer of TiAl₃ around the particle according to reaction (6.7). Upon cooling, the reaction stops and the particle solidifies with a TiAl₃ shell and an Al core. Depending on the thickness of the intermetallic layer, it may adhere to the particle or separate forming a hollow sphere due to CTE mismatch between Al and TiAl₃ and solidification shrinkage of the molten Al droplet. The thermal history for this group of particles is represented by case (2) in **Figure 6. 26**. The typical microstructure and proposed model are shown in **Figure 6. 27** and **Figure 6. 28**, respectively;

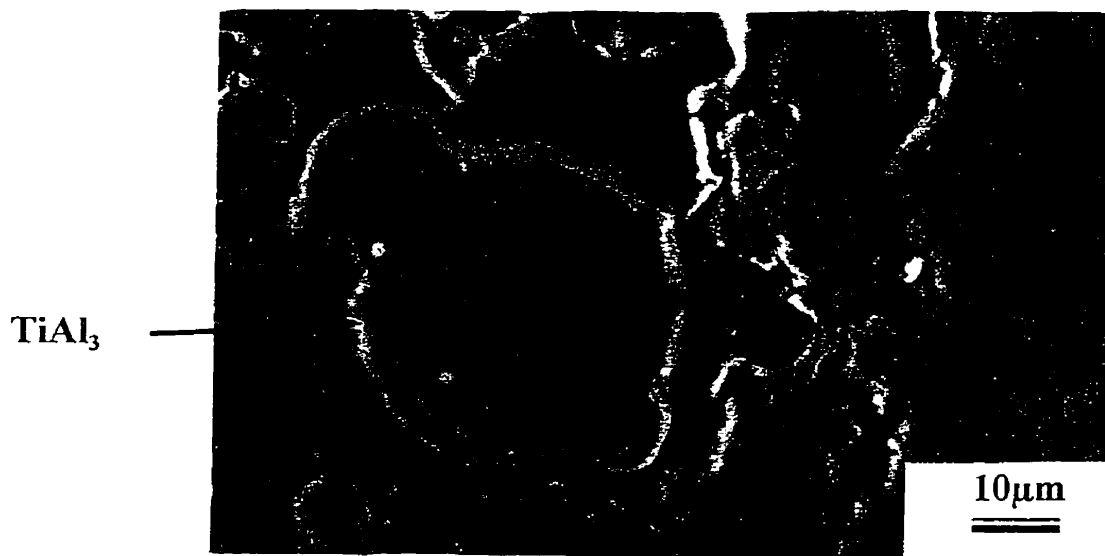
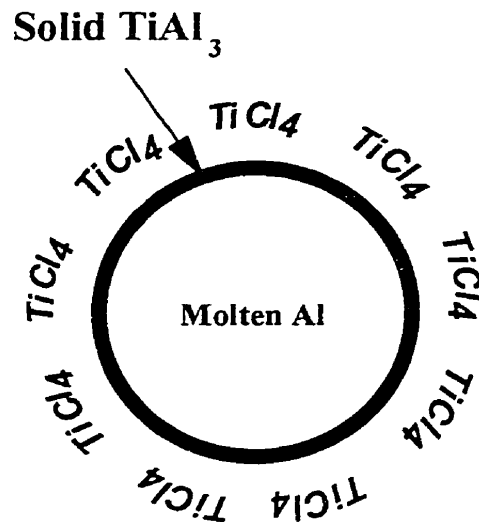


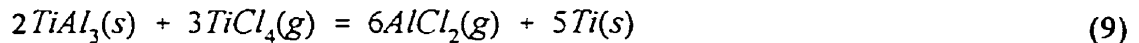
Figure 6. 27 Microstructure of an Al particle which has undergone the thermal history Case 2.



solidus < T < liquidus

Figure 6. 28 Proposed model for thermal history Case 2.

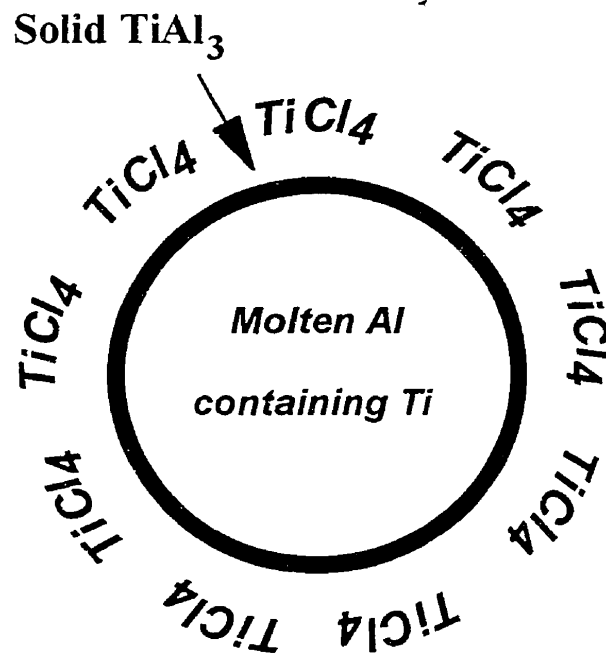
- 3) The particle may be heated to a temperature above 660°C but below the corresponding liquidus temperature, and then react with TiCl₄ according to reaction (7), forming a solid outer layer of TiAl₃. The reaction between Al and TiCl₄ is replaced with a slower reaction between TiCl₄ and TiAl₃ that may be represented as:



When the particle stays molten, part of the TiAl₃ dissolves in the molten Al (core) to satisfy the phase equilibrium. The overall reaction rate at this step is controlled by the dissolution rate of TiAl₃ in the molten Al. Upon quenching, the final microstructure is an Al-TiAl₃ composite inside a TiAl₃ shell. The typical microstructure, and its schematic model are shown in (9). Again, case two in **Figure 6. 26** represents its corresponding thermal history; and



(a)



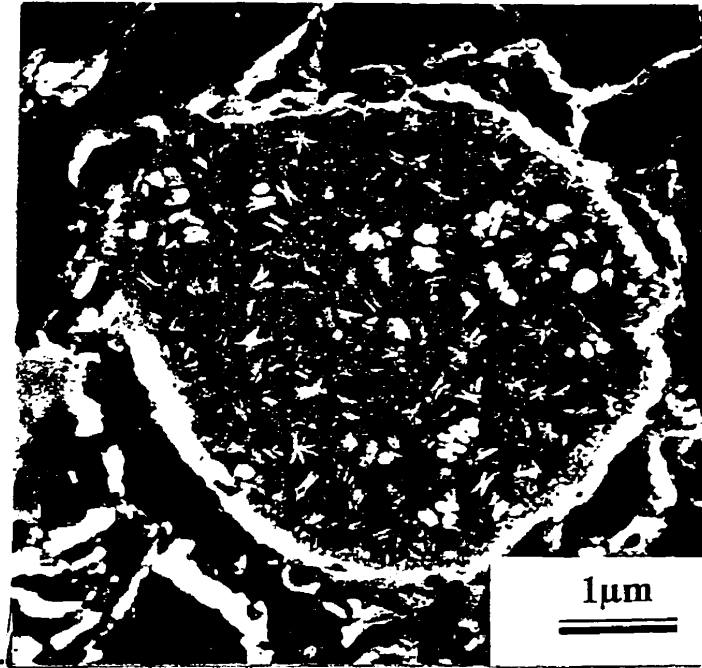
(b)

Solidus < T < Liquidus

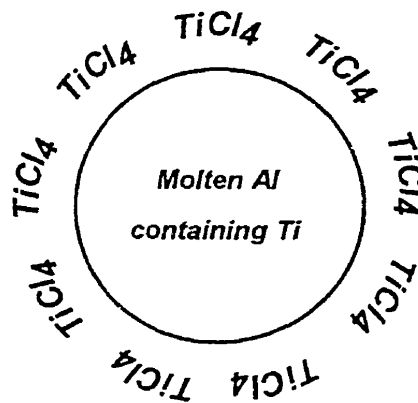
Figure 6. 29 (a) Microstructure, and (b) schematic model for thermal history, case 3.

- 4) The particle may be heated above the liquidus temperature of the alloy. While the reaction starts on the surface of the particle, the TiAl₃ does not form. Instead, the Ti recovered from the TiCl₄ dissolves in the molten Al, and the molten Al (containing Ti) is exposed to TiCl₄. The reaction proceeds according to reaction (6.7) but the reaction kinetics is controlled by the activity of Al in the molten Al-Ti alloy. Gradually, the concentration of Ti is increased on the surface of the droplet and Ti-rich intermetallics such as TiAl or Ti₃Al are formed. Very fine particles sometimes obtain a very high temperature and form such intermetallics. Occasionally, these intermetallics were observed in the microstructure and their contents were estimated to be less than one vol.% using image analysis. Temperatures higher than liquidus temperature and long reaction time promote the formation of Ti-rich intermetallics. Unfortunately, the residence time in thermal plasma spray is of the order of milliseconds which is very short for particle heating, melting, and full reaction. Eventually, the saturated molten Al is quenched and the product consists of a very fine dispersion of TiAl₃ in an Al matrix. The thermal history corresponding to this case is represented by curve three in **Figure 6. 26**. The microstructure of this group of particles and its schematic model are shown in **Figure 6. 30**.

A case has not been considered above and that is when an Al particle is heated so quickly in the plasma jet that only surface melting occurs. In other words, the convective rate of heat transfer on the surface is faster than the rate of heat conduction through the Al particle thus surface melting occurs. Here, molten Al on the particle surface reacts with TiCl₄ forming a TiAl₃ shell. This case is prone to produce similar microstructure to case two as discussed above.



(a)



(b)

T > liquidus

Figure 6. 30(a) microstructure, and (b) schematic model for thermal history, case 4.

6.3.2.3. Velocity and Temperature Distributions

Velocity and temperature are the two most important characteristics of and thermal plasma system. It was hypothesized in § 6.3.2.1 of this chapter that the temperature and velocity distributions in the reaction zone and atomization plume may cause Ti content variation from the centre to the periphery of the reactively sprayed deposit. Typical velocity and temperature distribution in a thermal plasma were shown in **Figures 2.2 and 2.3**. However, no information is available for temperature and velocity distributions within a triple plasma system in the literature. This system is very similar to water or gas atomization and very little literature is available on velocity distribution. For example, See et.al., have studied the quadruple gas jet atomization system and have measured the velocity profiles, as shown in **Figure 6.31**. It can be seen that in the centre of the atomization plume the gas velocity is higher than at the periphery. Higher gas velocity results in higher particle velocity assuming that particles in the jet obtain their adjacent gas velocity. A very similar pattern is expected for the triple plasma atomization system but with much higher velocity profiles.

The impact of this variation in velocity on reactive plasma atomization can be viewed as:

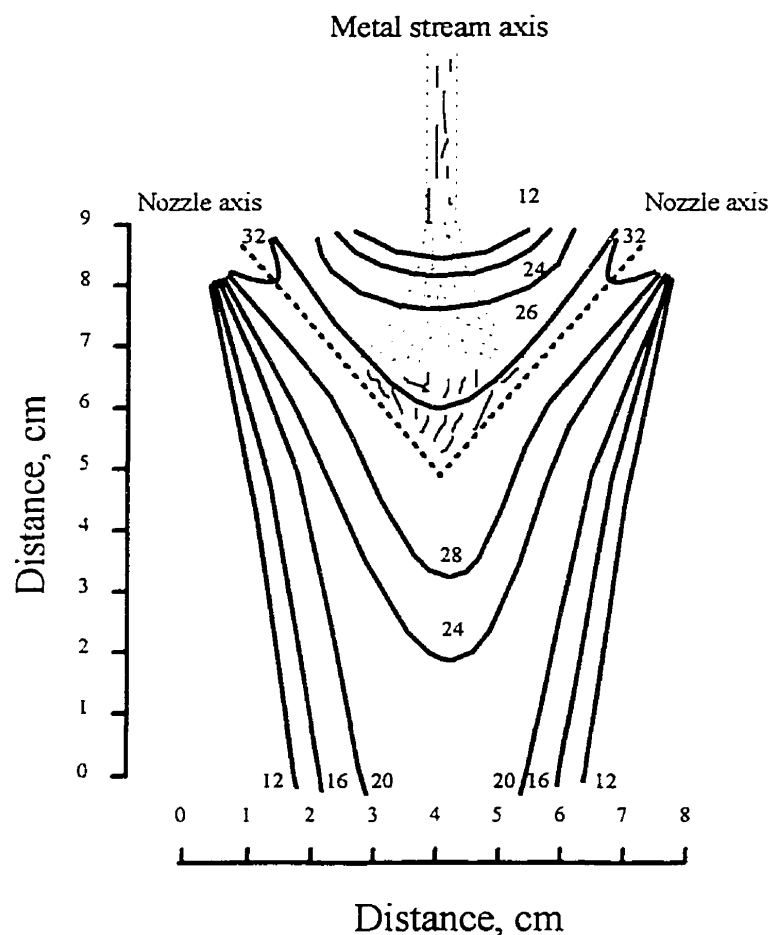


Figure 6.31 Lines of constant gas velocity (m/s) in gas atomization.

- a) higher particle velocity means shorter residence time in the hot plasma jet, which results in shorter reaction time and consequently lower Ti content, and *vice versa*; and
- b) longer residence time can be translated into higher temperatures for these particles, as well as a higher reaction yield, and Ti content.

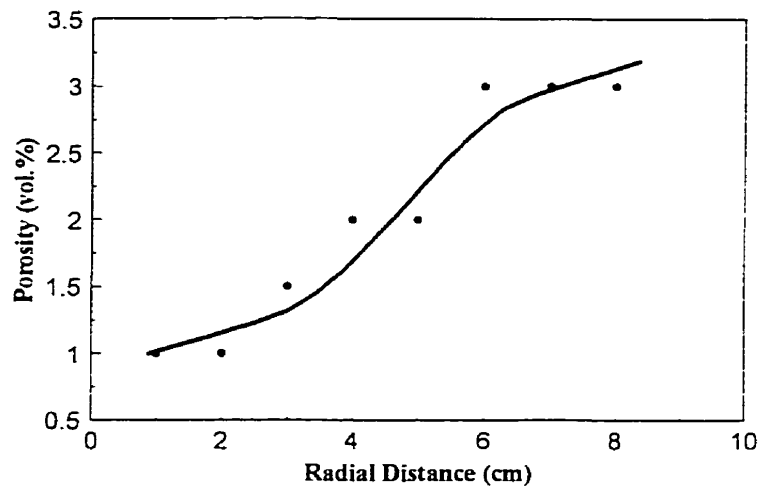
The combination of longer residence time, higher temperature, larger surface area available for reaction, and smaller mass characteristics for the particles travelling in the peripheral regions can explain the higher Ti content.

It should be noted that these particles (in the peripheral regions) are cooled faster than the particles in the central regions due to the mixing with the surrounding gases. Considering their lower mass, it can be concluded that these particles achieve a lower temperature, which contradicts the above conclusions. However, it is believed that both of the above arguments play a role and the overall result is a combination of both effects.

6.3.2.4. Porosity Distribution

Porosity content of the reactively sprayed deposits as a function of position is shown in **Figure 6. 32**. A higher porosity was measured in the peripheral regions than in the central regions. The lower porosity content in the central regions can be explained by: (a) the higher velocity of the particles deposited in this region, and can be interpreted from **Figure 6. 31**; and (b) the higher melting point of the particles deposited in this region.

Higher particle velocity means a higher particle kinetic energy on impact with the substrate resulting in a high degree of (deformation) flattening. The better deformation of the molten droplet on the substrate results in better filling of the pores already present in the deposit. In



dynamic liquid compaction, there is a competition between heat transfer to the substrate and material deformation. Ideally, it is preferred to have complete flattening before the start of the solidification process. During solidification, there is a higher resistance to deformation than in the molten state. Higher particle velocity on impact improves particle deformation while the substrate physical properties determine the heat transfer or solidification rate.

The combination of a lower particle velocity and a higher melting point (resulting from higher Ti content) for the particles deposited in the peripheral regions lowers the high temperature ductility of the particles and a higher porosity content is obtained.

6.4. PRODUCT DEVELOPMENT

6.4.1. Rolling

The as-sprayed samples were porous and had an irregular shape which made them unsuitable for testing. Coupons were cut from the sprayed deposits and subjected to rolling in order to: (a) remove porosity and, (b) obtain a regular shape for mechanical testing.

The rolling of a new material can be very challenging since there is usually little information available on its mechanical properties. The rolling temperature and amount of reduction in each pass are the two most important variables of any rolling operation. These variables can be easily estimated if the tensile properties of the material such as elongation, yield, and ultimate strength to fracture are known. However, this information was not available for Al-TiAl₃ composites, although, the literature provides such data for some other composites with similar microstructure but different chemistry. The mechanical properties and deformation characteristics of Al-SiC[128] composites are well documented and these values were used as the first approximation for rolling of Al-TiAl₃. The reasons for selecting the Al-SiC data as the first approximation was their availability and the similarity in terms of the second phase content.

6.4.1.1. Surface Condition of Coupons

The uneven surface of the coupons caused rolling defects due to inhomogeneities in deformation. In the initial rolling trials of Al-TiAl₃, the two surfaces of the coupon passing between the rolls were not parallel thereby causing one edge of the coupon to be thinner than the other. Since volume and width remained constant, this edge elongated more than the other and caused the rolled sheet to bow. Furthermore, edge barrelling was observed during all of the rolling experiments.

6.4.1.2. Effect of Reduction on Rolled Sheets

It was observed that the rolled samples at 350°C were elongated more in the center than along the edges, thus forming a pointed strip coming out of the rolling mill. At high reductions, between 15% and 25%, edge cracking was experienced as shown in **Figure 6. 33a**. Further rolling of these sheets resulted in the lengthening of the cracks towards the center of the sheets. Sometimes, edge cracking was observed at low reductions (less than 10%). These samples were ground on their edges to remove the cracks before any further rolling was performed. Under severe conditions, above 25% reduction, center splitting of the sheet was observed, see **Figure 6. 33b**. In most of the rolling trials curling of the sheet was observed, and in some cases alligating type of fracture was noticed (**Figure 6. 33c**). This was attributed to: (a) misalignment of the roll from the centerline of the roll gap, and (b) spray defects including porosity and poorly bonded particles.

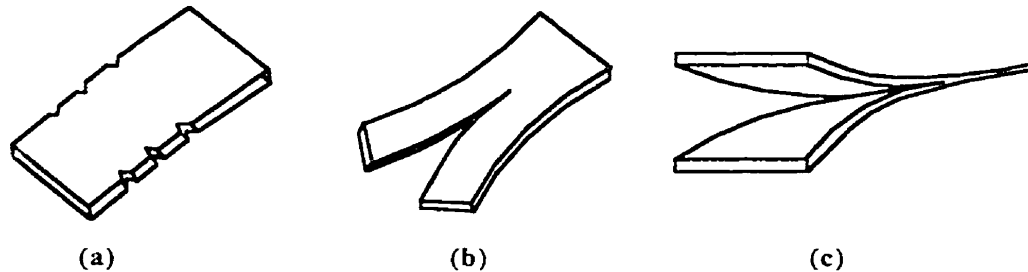


Figure 6. 33 Rolling defects observed during rolling of Al-TiAl₃, (a) edge cracking, (b) center split, and (c) alligating.

6.4.1.2. Effect of Rolling Temperature

Increasing the rolling temperature from 350 to 400 and to 450°C, improved the rolling of these composites at high reductions (higher than 10 %) resulting in fewer rolling defects. The maximum reduction for hot rolling at 450°C was 15%; above that edge cracking was observed. The increase in temperature is believed to produce strain-free grains through the recovery and recrystallization of the Al matrix. These softening mechanisms cause a decrease in the yield strength and an increase in ductility of the material.

6.4.1.3. Annealing

Hot rolling of Al-TiAl₃ composites (even at 450°C) caused an increase of 25% in the hardness of the sheets. In other words, the rolled sheets did not fully recover from the work hardening stresses developed during hot rolling. It is believed that this increase in hardness is due to the fact that:

(a) either Al recovers and recrystallizes from rolling stresses, however, the intermetallic particles (TiAl₃) interfaces with the matrix remain highly stressed. The annealing temperature (450°C) is high enough for complete recovery and recrystallization of the solid solution Al. It is assumed that the TiAl₃ phase undergoes very little deformation during rolling since this TiAl₃ phase has a very low ductility at fracture *i.e.* 5% at 400°C[129]. However, any deformation would not be stress relieved by annealing at such a temperature.

(b) or the temperature loss during rolling lowers the process into a temperature range where dynamic recovery and recrystallization of the Al matrix are incomplete.

Post annealing of the rolled sheets at 450°C for one hour decreased the hardness back to its original value. This suggests that most of the increase in hardness was due to the strain hardening of the Al matrix and the Al/TiAl₃ interfaces, and not by the TiAl₃ particles themselves.

In order to optimize the annealing time and temperature, samples were annealed at 350, 400, and 450°C, and three samples were removed from the furnace every 20 minutes. The hardness values of samples rolled at 450°C with 10% reduction and annealed at the above temperatures are shown in **Figure 6. 34**. The effect of temperature on softening the rolled sheet is more

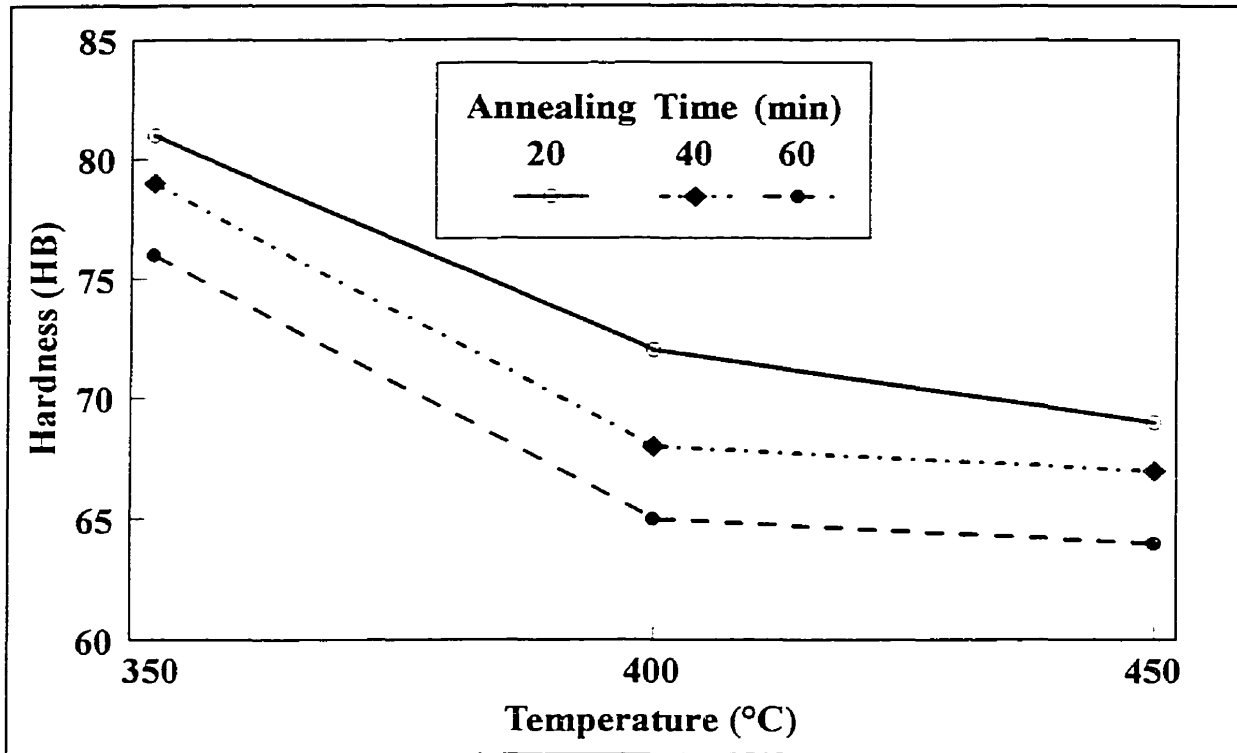


Figure 6. 34 The effects of annealing time and temperature on the hardness of the Al-TiAl₃ composite (10% Ti) rolled at 450°C with 10 % reduction.

significant than time. This is due to the importance of temperature on diffusion controlled softening mechanisms such as recovery and recrystallization. Annealing temperatures above 400°C and periods longer than 60 minutes had little effect on the hardness of the rolled sheets.

6.4.1.4. Effects of Rolling and Annealing on the Microstructure of the deposits

The TEM microstructure of an as-sprayed Al-TiAl₃ composite with 10 wt.% Ti is shown in **Figure 6.35**. This microstructure is characterized by the presence of Al grains and subgrains forming the matrix of the composite and the presence of the TiAl₃ precipitates. Moderately dense dislocation networks were observed and resulted from the splat quenching of the particles on the surface of the substrate and the impact of oncoming molten particles. The contraction of the individual particles is hindered by neighbouring particles, resulting in the creation of deformation zones observed in the microstructure.



Figure 6.35 TEM micrograph showing the microstructure of the as-sprayed Al-TiAl₃ composite.

Hot rolling deformed the as-sprayed microstructure and produced elongated subgrains after annealing 350°C; they become equiaxed at 400 and 450°C (Figure 6. 36).

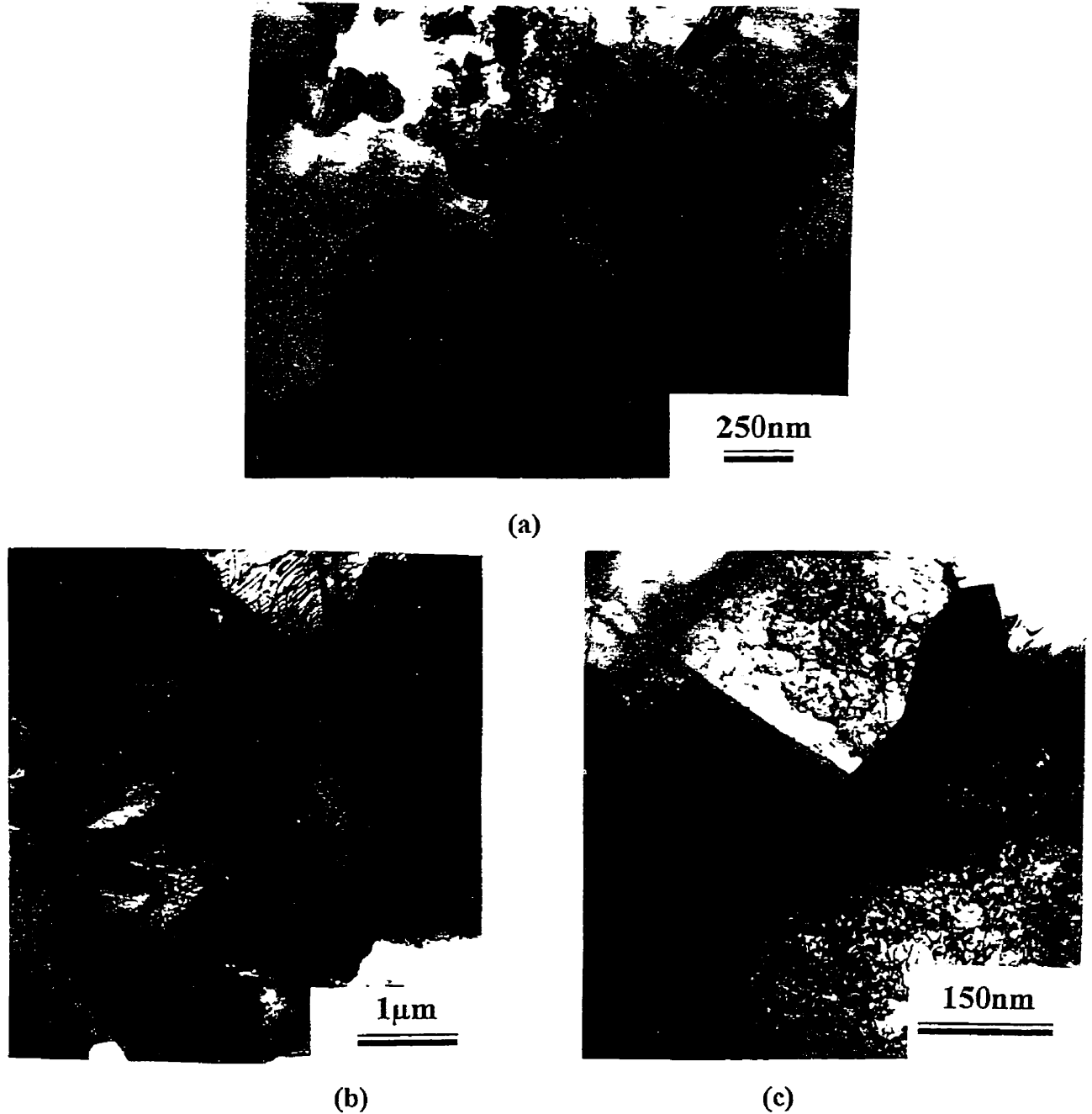


Figure 6.36 Elongated subgrains are observed for (a) sample tested at 350°C; equiaxed substructure for samples tested at (b) 400 and (c) 450°C.

It can be seen that by increasing the rolling temperature, the dislocation density of the matrix decreases while the subgrain size increases. The dislocation density decreases since they are annihilated and consumed through the dynamic recovery and recrystallization processes. The occurrence of dynamic recrystallization during hot rolling of Al-TiAl₃ composites was confirmed by the observation of the highly misoriented spots in the diffraction pattern. A typical dynamically recrystallized structure obtained after hot rolling at 400°C and its corresponding diffraction pattern are shown in **Figure 6. 37**.

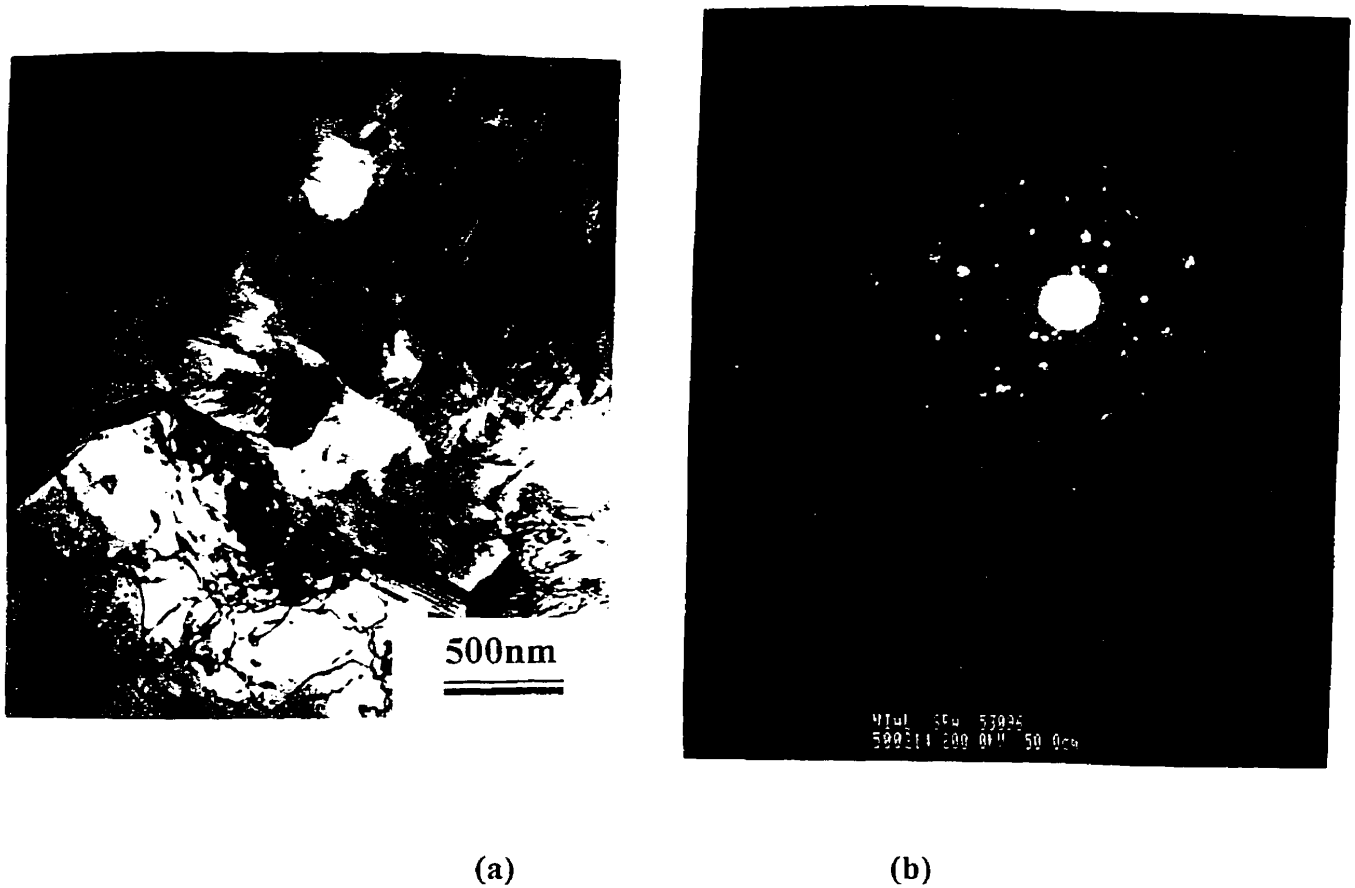


Figure 6. 37 (a) microstructure and (b) diffraction pattern of the dynamically recrystallized structure hot rolled at 400°C.

Hot rolling produced a microstructure containing partially recrystallized grains and deformation zones. Samples rolled at 450°C were annealed at various temperatures for a longer period (196 hours) in order to study the effect of high temperature exposure on the microstructure and room temperature tensile properties. It was observed that by increasing the annealing temperature the dislocation density decreases and subgrains grow.

New precipitates were formed during annealing at 300°C and above and were very fine; measuring a few nanometres in size as shown in **Figure 6. 38**. The size of these precipitates and their high interfacial coherency with the matrix indicates that they are formed from a supersaturated matrix such as those seen with heat treatable Al alloys through solution and aging treatment[130]. At equilibrium, only 0.15 at.% of Ti can dissolve in Al at room

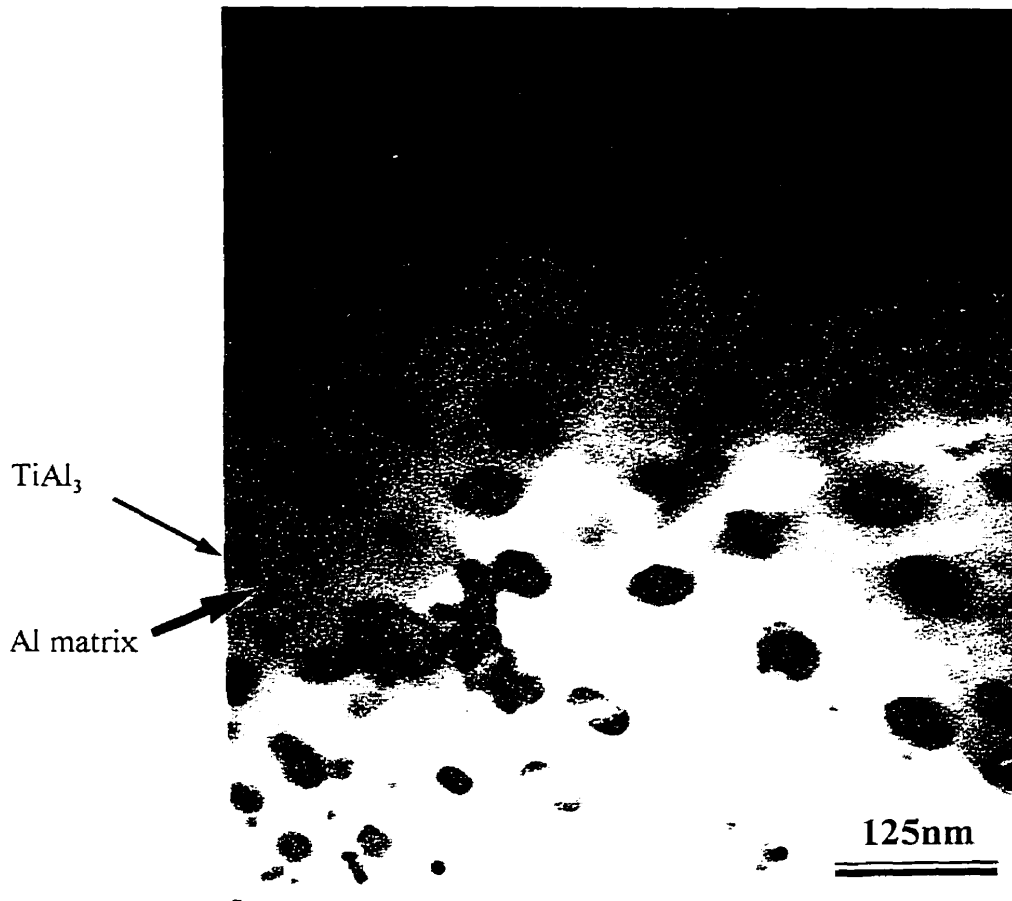


Figure 6. 38 Very fine dispersion of TiAl₃ in Al matrix formed during annealing at 300°C for 196 hours.

temperature. However, it has been reported that up to 2 at.% of Ti can be dissolved in through rapid solidification processes such as melt spinning and splat quenching[131]. Plasma spray deposition is considered to be a rapid solidification technique, with a cooling rate as high as 10^6 K/s.[132]

The image analysis performed on the micrographs obtained through TEM showed that 1.7 at.% of Ti can be dissolved in Al through reactive plasma spraying. Only TiAl₃ particles finer than 100 nm were counted and considered as particles formed during annealing and precipitation from solid solution. The TEM samples of the as-sprayed microstructure did not reveal any particles finer than 100 nm. Therefore, particles finer than 100 nm observed after annealing were considered to have precipitated from solid solution.

Annealing of the Al-TiAl₃ composites at 450°C for 196 hours showed three microstructural changes which can be summarized as follows:

- a) no grain boundary structure was observed under the optical microscopy and this was attributed to the very fine grain size ($\sim 2 \mu\text{m}$) of the matrix developed during the plasma spray deposition. TEM analysis performed on ten random locations showed only $8\% \pm 1.5$ increase in the average grain size. A typical coarse grain structure ($>3 \mu\text{m}$) is shown in **Figure 6. 39a**, which can be compared with the original microstructure shown in **Figure 6. 36c**;
- b) grain growth of the TiAl₃ particles, and
- c) creation of a low dislocation density (**Figure 6. 39b**).

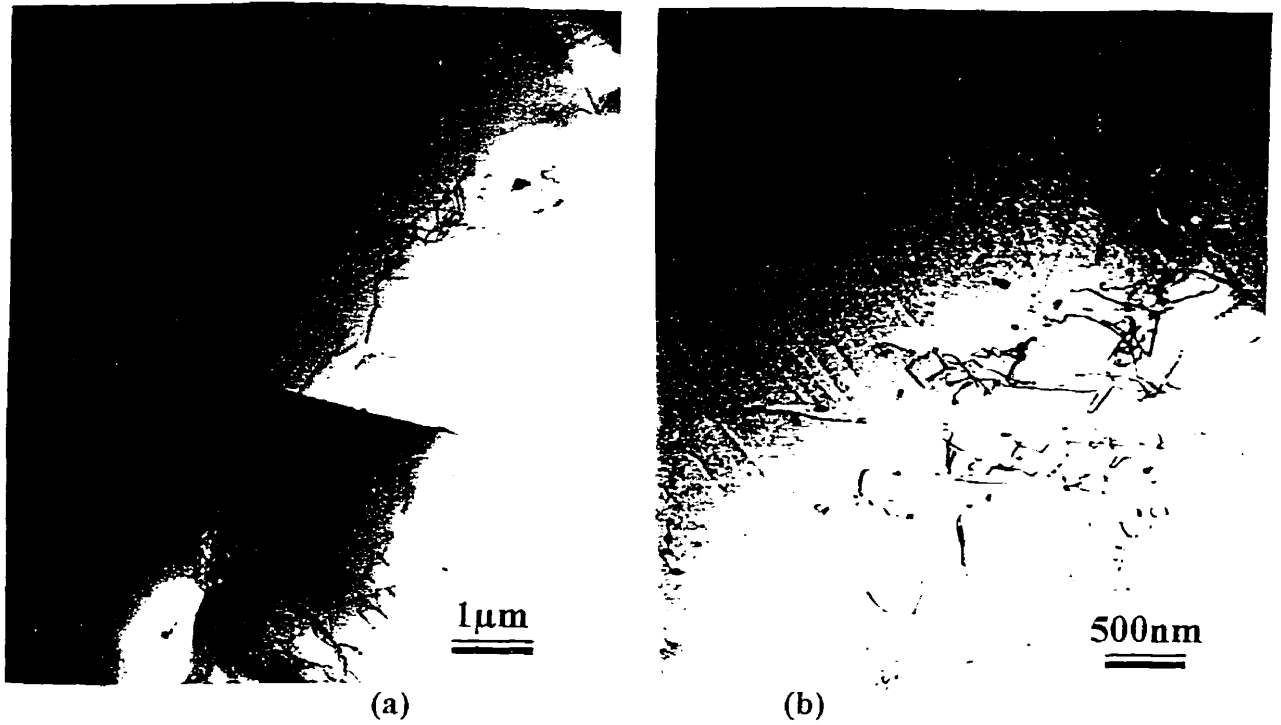


Figure 6. 39 TEM microstructure of the Al-TiAl₃ composite annealed at 450°C for 196 hours showing (a) grain growth and (b) low dislocation density.

6.5. MECHANICAL PROPERTIES

6.5.1. Yield Strength

The average yield strength of the as-sprayed material was 100 MPa (**Figure 6. 40**) and was increased by 50% after rolling and annealing. The reasons for this increase are: (a) the closure of the porosity and the increase in the effective surface area subjected to tensile stresses; (b) the improvement of the surface finish and the elimination of the surface irregularities associated with the as-sprayed surfaces; (c) the increase in matrix-particle bonding; and (d) texture alignment. The effect of annealing temperature on the yield strength of both 2024-T4 Al alloy and reactive plasma sprayed deposit of Al-10% Ti are compared in **Figure 6. 40**. It can be seen that above 250°C, the yield strength of the Al-TiAl₃ alloy is greater than that of 2024-T4 alloy. It should be noted that pure Al was used for this reaction and is the matrix of the microstructure. It is believed that by using Al alloys containing Mg and Mn, a higher strength matrix will be obtained and, consequently, the overall properties of the composite will improve markedly. However, assessing this possibility was beyond

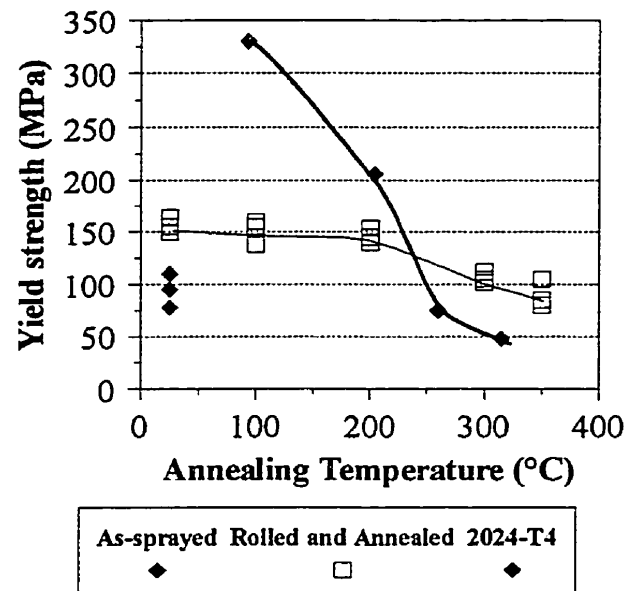


Figure 6.40 Room temperature Yield strength of Al-10 wt.% Ti after annealing at various temperatures.

scope of the current investigation.

6.5.2. Tensile Strength

The average room temperature tensile strength of the as-sprayed materials containing 10 wt.% Ti was 100 MPa. Rolling the sprayed material increased this value by 75%, up to 175 MPa (**Figure 6. 41**). It can be seen that the Al-Ti alloy retains its tensile and yield strengths up to 300°C. This is a good indication that there is no significant change in chemistry and microstructure of this material. Above 300°C, the tensile, and the yield strengths are decreased significantly. This is believed to be due to the removal of residual stresses, recrystallization, and growth of strain-free regions. In addition, the dissolution and growth of the very fine intermetallic particles (shown in **Figure 6. 38**) in the Al matrix leads to reduced strength. In general, pure Al may not be a proper matrix for an alloy designed for high temperature application since it loses its tensile properties above 150°C. The use of a

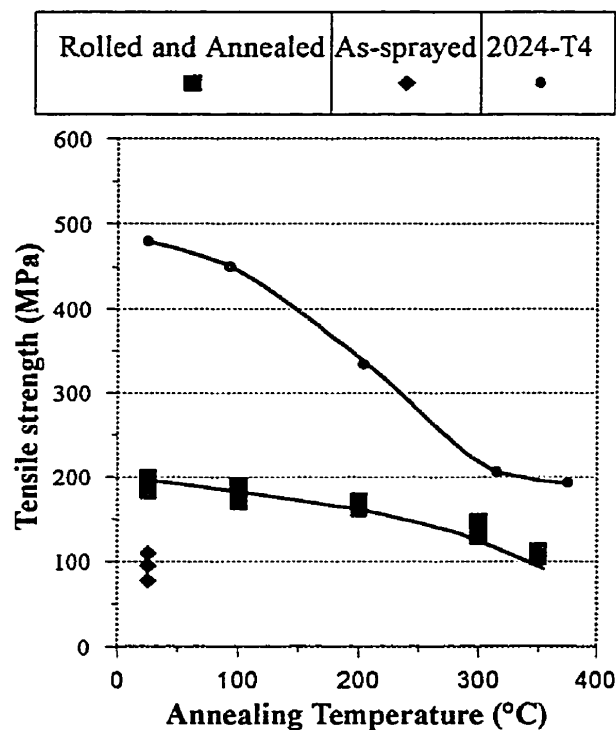


Figure 6.41 Tensile strength of the reactive plasma sprayed material.

heat-treatable Al alloy instead of pure Al should result in a much higher strength. Pure Al was used in this research program in order to simplify the complex chemistry involved in the process.

6.5.3. Elongation

The elongation of the as-sprayed material was approximately 1% and was increased to 5 % after rolling and annealing (Figure 6. 42). The low ductility for the as-sprayed materials can be explained by the presence of porosity, oxide and chloride contents and low inter-particle cohesion. Therefore, an improvement in the elongation was observed after hot rolling, since this treatment improves the density, the particle-matrix, and the inter-particle bonding. Furthermore, the growth of strain-free regions softens the materials at high temperatures.

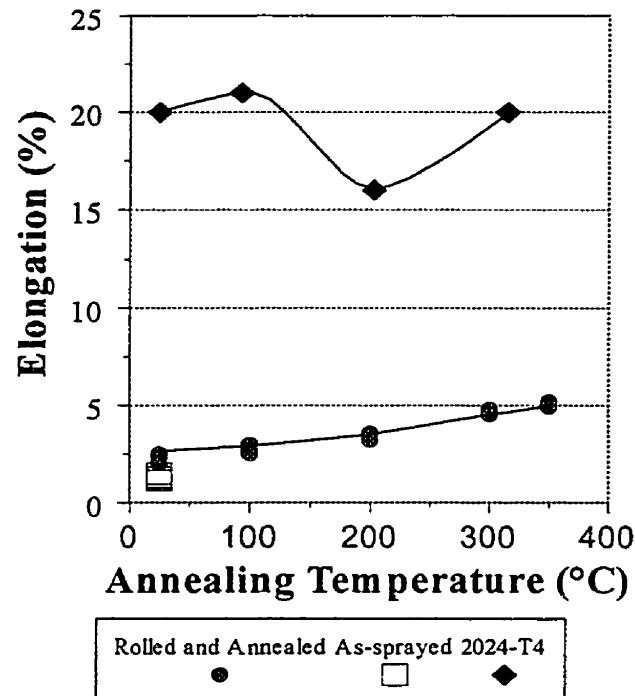


Figure 6.42 Elongation of the reactive plasma sprayed material compared with 2024-T4.

However, the elongation of the sprayed material is very low as compared with that the 2024-T4 alloy.

The results of tensile tests performed on reactively sprayed materials and HIPped are compared with squeeze cast A356-20 vol.% SiC and 2024-0 Al alloy in Table 6.3.

Table 6.3. Room temperature mechanical properties of the reactively sprayed materials compared with competing materials.

Material	Tensile Strength (MPa)	Yield Strength (MPa)	Elongation (%)
HIPped, Rolled, Annealed	210	170	8
Reactively sprayed material	175	150	5
Squeeze cast A356-20 vol.%SiC	279	250	0.3
2024-O[133]	180	75	20

* Pure Al matrix

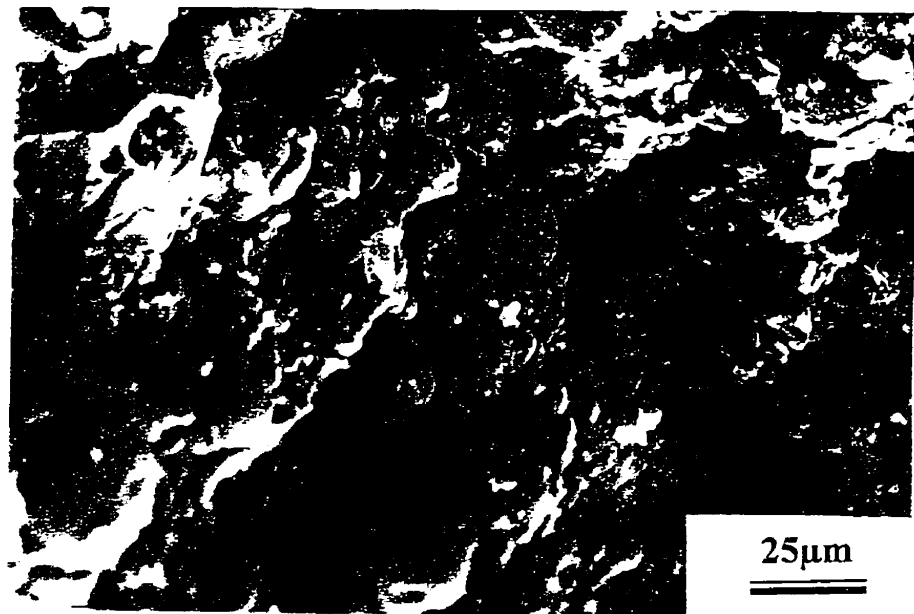
It can be seen that the room temperature mechanical properties of the reactively sprayed material are lower than that of the HIPped material. The main reason is the presence of discontinuities such as: porosity, chlorides, and in-flight solidified particles in the sprayed material. These defects reduce the effective surface area subjected to the force applied; therefore, a lower value is obtained.

6.5.4. Fractography

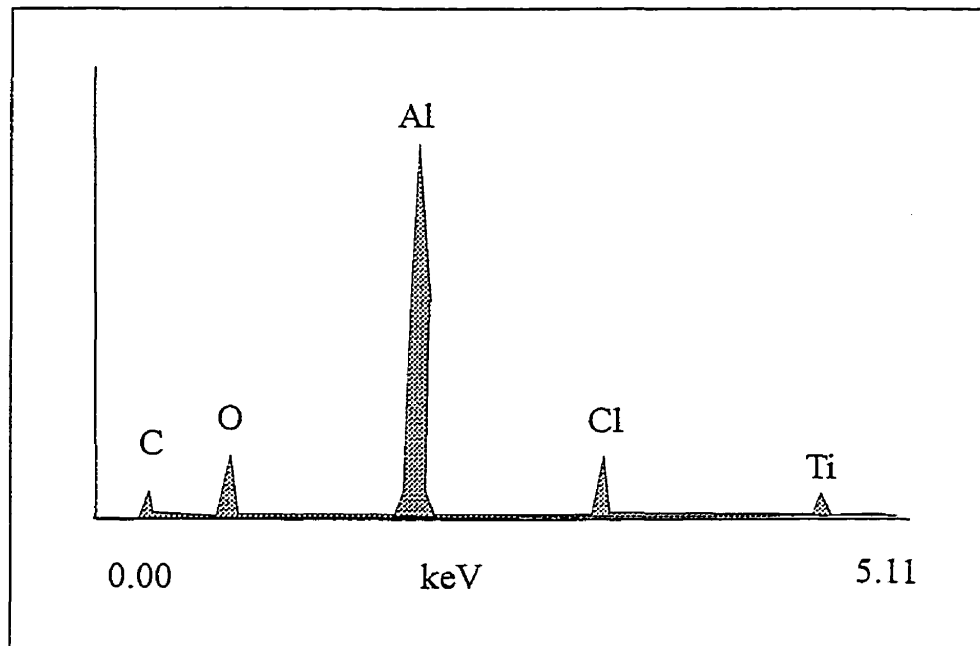
A fracture surface of the reactively sprayed material is shown in **Figure 6. 43a**. This sample resulted in a yield strength of 80 MPa. The present of spherical powder in the fracture surface suggests that some particles solidify in flight after spherodization and before deposition. These series of particles were not well bonded to other particles deposited on the substrate and result in a lower strength and ductility. The spherical shape of these particles shows that they have not experienced any deformation while impacting on the substrate. For this specimen, a high volume of spherical powders (10 vol. %) is observed resulting from a long spray distance (50 cm). The volume of these particles was reduced to 2 vol. % by reducing the spray distance to 35 cm. The fracture surface of a deposit sprayed at the shorter distance is shown in **Figure 6. 44**. It can be seen that the fracture mode has been changed from interparticle fracture to dimple and, therefore, ductile fracture mode. This specimen resulted in a yield strength of 160 MPa.

The EDS analysis of the fracture surface also revealed the presence of chlorine and oxygen, as shown in **Figure 6. 43b**. Chlorine was not detected on the surface of the polished samples prepared for metallography. This implies that chlorine is only a surface contaminant and has deposited and become trapped in pores. The substrate temperature was kept at 600°C, as found from TGA (§ 6.3.1.1) to ensure that most of chloride compounds remain volatile and are removed through the off-gas. However, it seems that a higher temperature will be required for complete removal of chlorine from the reactively sprayed materials. A higher substrate temperature (above 660°C) results in melting of the Al matrix defeating the purpose of obtaining a splat quenched and fine microstructure.

Oxygen also was detected on the fracture surface suggesting the presence of oxides, which can also contribute to low ductility of the reactive plasma sprayed materials. Surface oxides may form during atomization as a result of the reaction between the molten Al droplet and



(a)



(b)

Figure 6.43 (a) Fracture surface of the reactive plasma sprayed materials and (b) EDS spectrum showing the presence of Cl.

the oxygen. The presence of a refractory oxide on the surface of the droplets hinders interparticle micro-welding which results in a lower inter particle bonding. The oxidation of molten Al is almost inevitable due to the high affinity of Al for oxygen even at a very low oxygen partial pressures ($<10^{-20}$ mbar). The oxygen contents of the reactively sprayed deposits were analyzed to contain an average of 1.70 ± 0.5 wt.%. The original Al wire used for these experiments had 1 wt.% percent of oxygen. The major source of oxygen is believed to be the surface oxide on the Al wire. Since a very thin Al wire diameter (ϕ 1.58 mm) was used, a relatively large surface area of oxide was introduced to the system. For every gram of Al, 20 cm of wire was fed to the reactor and is accompanied by 0.4 cm^2 of oxidized surface. Some precautions may have helped in reducing the oxygen content e.g. chemical etching of the wire with a HF solution before feeding. Using a thicker wire reduces the surface area per gram of Al wire however, it influences the atomization process producing large particles, as discussed in Chapter 5.

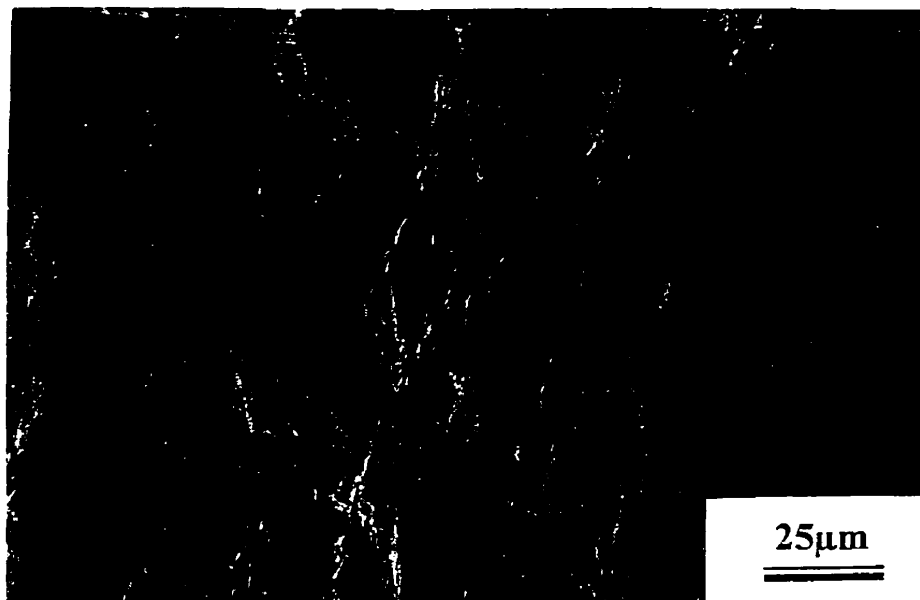


Figure 6.44 Fracture surface of the material formed at a spray distance of 35 cm.

6.6. CHLORINE CONTENT

The formation of Al and Ti chlorides are inevitable in this system. Thus, their deposition on the substrate should be avoided. The chlorine content of the reactively sprayed material varied from 0.3 to 1.3 wt.% depending on the experimental conditions. Parameters influencing the presence of chlorides in the products can be classified in two major groups. The first group includes factors which promote Ti and Al chloride formation. The Al subchlorides can be removed more easily than Ti subchloride. These parameters include: TiCl₄/Al ratio, argon flow rate, TiCl₄ injection port geometry, Al wire size, power/Al ratio, and TiCl₄ carrier gas flowrate. The second group involves parameters which prevent subchlorides deposition on the substrate. These parameters include: substrate temperature, temperature and pressure inside the reactor, and spray distance. Most of these parameters are dependant parameters and their study was beyond the scope of this research program. Some parameters therefore, were obtained from prior art and the effect of the key parameters are discussed here[134]. The effect of TiCl₄ feed rates on chlorine content of the reactively sprayed material is shown in **Figure 6. 45**. It can be seen that by increasing the TiCl₄ flow rate while maintaining the other paramteres constant, the chlorine content of the products increases. At high TiCl₄/Al ratios, TiCl₄ cannot be completely reduced thus Al subchlorides are not formed. Instead TiCl dissociates forming Ti subchlorides which have a higher boiling temperature than Al subchlorides and thus deposit on the substrate and increase the chlorine content of the deposit.

Power to Al ratio determines the melting location of the wire, average particle size and temperature of the powder produced, and were discussed in Chapter 5. The combination of these effects influences reaction (6.7) to provide a higher reaction yield for Ti recovery from TiCl₄. The effect of power/Al ratio on Cl₂ and Ti contents of the sprayed deposit are shown in **Figure 6. 46**. Higher Cl₂ and Ti contents were measured in the deposit by increasing the power/Al ratio. Higher power in the system provides higher heat for the

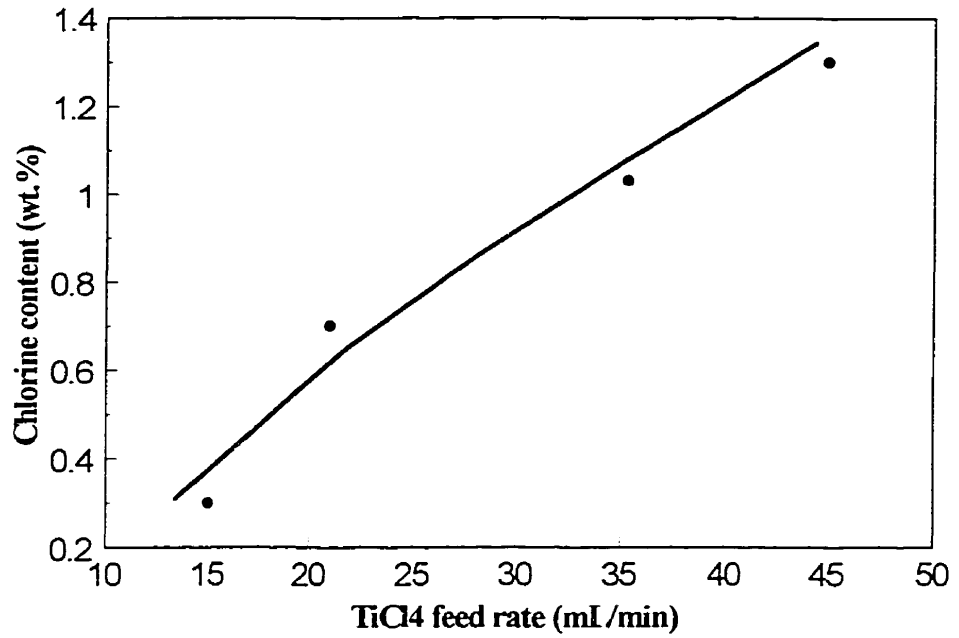


Figure 6. 45 Chloride content of the reactively sprayed materials as a function of TiCl₄. Flow rate. P=85kW, Ar= 110 L/min, T_{TiCl₄}= 220°C, Power/Al=1.9 kWh/(g/min), Al wire dia.= 0.24 cm, and S.D. =30 cm.

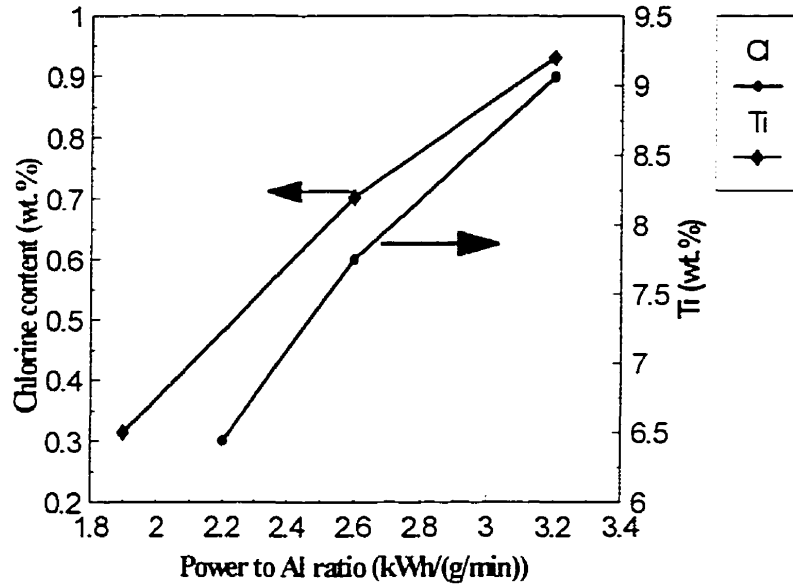


Figure 6. 46. Cl₂ and Ti contents as a function of power to Al feed rate ratio. TiCl₄= 21mL/min, Ar=110 L/min, T_{TiCl₄}=220°C, Al wire dia.= 0.24 cm, and S.D.=30 cm.

endothermic reduction of TiCl_4 by Al. Therefore, reaction (6.7) shifts toward an increase production of metallic Ti and subchlorides.

Decreasing the Al wire size increased the Ti and Cl_2 contents of the deposit, as shown in **Figure 6. 47**. Only two available wire sizes of 0.16 and 0.24 cm were tested. It is believed that decreasing the wire size produces high temperature particles which produce higher Ti and consequently higher subchlorides.

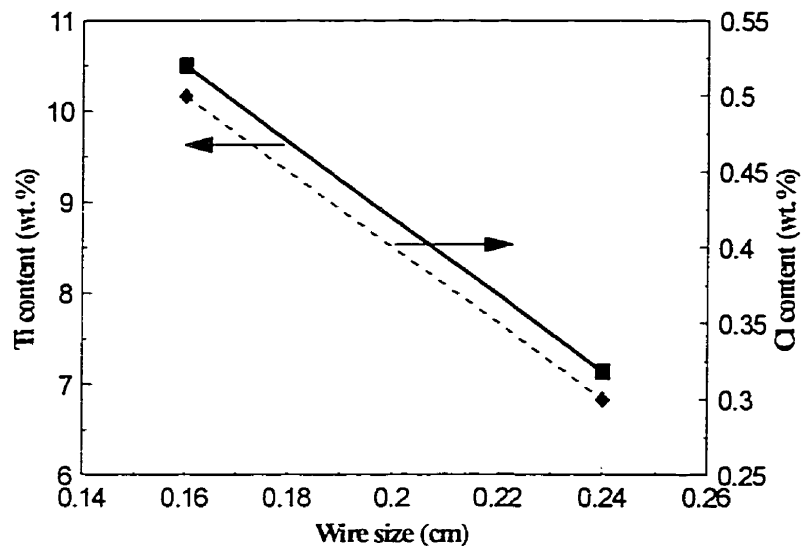


Figure 6. 47 . Effect of wire size on Ti and Cl_2 content of the deposit.

6.6.1. Chlorine Removal

The reactively over-sprayed powder was subjected to various time and temperatures under vacuum (10^{-5} mbar) to remove the chlorine through vacuum sublimation. The results of vacuum sublimation are shown in **Figure 6. 48**. The original sample contained 1.3 wt.% of chlorine and a vacuum of 10^{-5} mbar reduced it to between 0.4 and 0.6 wt.%. Increasing time and temperature also reduced the chlorine content. It can be concluded that vacuum sublimation can be used to remove chlorine contamination from reactively produced powders.

However, it cannot be so effective for reactively sprayed deposits since some chlorine is also trapped inside pores while for powders it is only adsorbed on the surface. This was confirmed by the fractography results where chlorine was detected on the fracture surface of the tensile specimen.

The presence of chlorine is specific to reactively sprayed Al-Ti materials. The same source of chlorine contamination has been observed with the products produced through the Kroll process. Ti sponge produced through this process contains about 0.12 wt.%Cl and parts produced using such powders have lower mechanical properties compared to chlorine-free materials and has been attributed to the presence of chlorine in the closed pores [135].

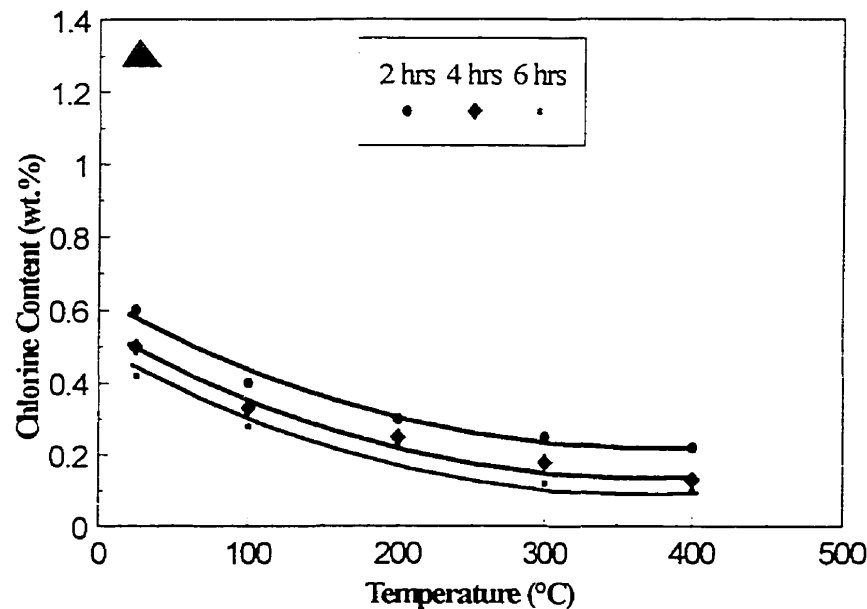


Figure 6. 48. Chlorine content of the reactively produced powder.

CHAPTER 7

ACHIEVEMENTS

and

CONCLUSIONS

7.1. Technical Achievements

7.1.1. Reactive plasma atomization

- Al-10 wt.%Ti alloys were produced using both a single plasma and a triple plasma system, with Al and TiCl₄ as raw materials.
- A triple TiCl₄ feeding system was built for triple plasma spraying.
- A vacuum sublimation system was designed, built and used for chlorine removal from reactively sprayed deposits.

7.1.2. Plasma Atomization

- A new atomization process called *Plasma Atomization* was developed. This process can produce fine spherical powders with an average particle size ranging from 40 to 100 μm .
- The effects of processing parameters in the plasma atomization process such as wire feed rate, wire feed size, plasma power to metal feed rate ratio, reactor size, and front nozzle design were optimized.

7.2. Conclusions

The following conclusions can be drawn from this investigation:

7.2.1. Reactive plasma spraying

- The particle temperature is a very important factor controlling the reaction yield, and microstructure of the reactively sprayed deposits.
- The reactively sprayed materials were characterized with an extremely fine dispersion of TiAl_3 intermetallics ($< 5\mu\text{m}$) within the aluminum matrix.
- A non-uniform distribution of Ti was observed across the deposit, resulting in a low concentration of Ti at the centre and a higher concentration in the peripheral regions.
- The non-uniform Ti distribution was attributed to the particle size, velocity, temperature, and mass differences between the central and peripheral regions.

- It was established that within the central regions three times higher mass of materials was deposited than in peripheral regions. In addition, the average particle size for the central and peripheral regions were measured to be 82 and 60 μm , respectively. It is believed that finer particles on the periphery achieved a higher temperature and thus a higher reaction yield which results in a higher Ti content.
- Chlorine was found in reactively sprayed materials. The TGA performed on the reactively sprayed powders revealed that chlorine compounds can be removed by vacuum sublimation at 625°C. However, the EDS analysis of the tensile specimen fracture surface, subjected to vacuum sublimation before testing, revealed the presence of chlorine, confirming entrapment of chlorine in the reactively sprayed deposits.
- Hot rolling of reactively produced materials was found very difficult. At high reduction (>25%) centre splitting occurred, and at reductions between 15 and 25%, edge cracking was observed. The optimum rolling conditions for reactively sprayed material containing 10 wt.% Ti were 450°C and 15% reduction per pass.
- Thermo-mechanical treatments (rolling and annealing) increased the tensile and yield strengths, and the elongation of the as-sprayed products. It was also shown that the reactive plasma sprayed materials are thermally stable and retain their room temperature mechanical strengths after annealing up to 300°C.

7.2.2. Plasma Atomization

- Experiments with molten Al feed resulted in inconsistent data. It was found that the alignment of the feeding nozzle tip with respect to the apex, the plasma forming gas flowrate, and the control over the molten metal feed are the most important factors

in this process. Overall, it can be concluded that powder with an average particle size between 200 and 400 μm and production rates as high as 177 g/min can be produced using the molten metal feed approach. The powders produced by molten metal feed are too coarse for reactive plasma atomization.

- For plasma atomization feeding metal wires, it was found that the metal feed rate to power is a very important parameter determining the melting and atomization location along the feed wire. It also was found that the optimum metal feed rate depended on the physical properties of the metal. Metals with higher thermal conductivity and diffusivity result in a higher optimum metal feed rate and a higher production rate.
- The alignment of three plasma torches within the apex and the use of plasma jet accelerating nozzles in front of the plasma torches are the key factors for production of high quality spherical powders in the 50 μm size range. Smaller wire diameters produced a finer powder size.
- When compared with existing atomization processes, the plasma atomization process offers unique capabilities in the atomization of reactive metals such as Ti, and Zr. It is the only known process capable of producing spherical Ti powder in the 50 μm range.

7.2.3. Casting, Powder Metallurgy, HIPping, and Plasma Spraying

- Casting produced acicular TiAl_3 morphology while powder metallurgy and vacuum plasma spraying produced blocky TiAl_3 in an Al matrix. The average TiAl_3 size was found to increase with sintering temperature.
- Spraying a mixture of Al and Ti powder onto a stainless steel substrate produced a

thin layer of Al-TiAl₃ microstructure. It was found that the coating reacts with the substrate forming complex intermetallics at the interface. Spraying on Ti substrate resulted in a very thin reaction zone at the interface.

- The DTA performed on the elemental powder of Al and Ti showed that they react at about 825°C. Therefore, a substrate temperature of at least 825°C is required.

- HIPping elemental powders of Al and Ti below the melting point of Al produced an Al matrix with partially reacted Ti particles. HIPping above the melting point of Al produced a sound fully dense and reacted microstructure.

Contributions to Original Knowledge

The salient points of this thesis, with respect to novelty and originality, are given as follows:

- 1- For the first time, a triple plasma configuration was analysed for the bulk production of structural materials (in particular Al-TiAl₃ composites).
- 2- The product obtained by reactive plasma spraying was compared with more conventional metallurgical processes such as: casting, powder metallurgy, and reactive hot isostatic pressing.
- 3- Through this study the importance of the plasma atomization step which occurs prior to reaction was discovered. For the first time the plasma atomization process using a triple plasma system was developed and used for powder production. The effects of the most important process parameters such as reactor size, wire diameter, torch alignment, and power/feed rate were studied and optimized.
- 4- Novel Al-TiAl₃ composites were produced in large quantity using a triple plasma spray system. The non-uniform distribution of Ti in the product was evaluated and attributed to particle velocity, size, and temperature.
- 5- For the first time the product of reactive plasma spraying using a triple plasma system (*i.e.* Al-TiAl₃ composites) was processed by hot rolling and the resulting mechanical properties and microstructure were evaluated.

- [1] Thermal Plasmas, Fundamentals and Applications, Vol.1, M.I. Boulos, P. Fauchais, and E. Pfender, Plenum Press, New York, (1994).
- [2] M. Vardelle, A. Vardelle, P. Fauchais, and M.I. Boulos, *AIChE J.* **29**, p. 239, (1983).
- [3] M.L. Thorpe, "Advanced Materials and Processes", 143 [5], p. 50, (1993).
- [4] H. Herman, *KONA, Powder Science and Tech.* **9**, p. 187, (1991).
- [5] C.C. Berndt et al., *J. Thermal Spray Tech.* **1**(4), p. 341, (1992).
- [6] D.L. Houck, "Modern Developments in Powder Metallurgy", **12**, p. 485, (1980).
- [7] S. Sampath, "Rapid Solidification During Plasma Spraying", Ph.D. thesis, State University of New York, Stony Brook, (1989).
- [8] Plasma Spraying of Metallic and Ceramic Materials, D. Matejka and B. Benko, John Wiley & Sons, West Sussex, UK, (1989).
- [9] K.A. Kowalsky, D.R. Marantz, R.A. Neiser, and M.F. Smith, "Proceedings of the International Thermal Spray Conference", C.C. Berndt, ed., Orlando, FL, May, 28-June 5, p. 337, (1992).
- [10] R. Greenlaw, M.S. Thesis, SUNY Stony Brook, (1995).
- [11] H. Herman, *Scientific American*, Vol. 256 [9] p. 112, (1988).

- [12] E. Muehlburger, "A High Energy Plasma Coating Process", Proceedings of the 7th International Thermal Spray Conference, London, England, (1973).
- [13] M.R. Jackson, J.R. Rairden, J.S. Smith, and R.W. Smith, "Production of Metallurgical Structures by Rapid Solidification Plasma Deposition", J. Metals, 33, p. 23-27 (Nov.1981).
- [14] S. Sampath and H. Herman, J. of Metals 45(7), p.42, (1993).
- [15] R. Tiwari, H. Herman, S. Sampath and B. Gudmundsson, "Plasma Spray Consolidation of High Temperature Composites", Mat.Sci. and Eng. A144 p.127-131, (1991).
- [16] P. Chraska and M. Hrabovsky, "Proceedings of International Thermal Spray Conference", Orlando, ASM Int., Ed. C.C.Berndt, p. 81, (1992).
- [17] D.R. Marantz, "Electromagnetically Coalesced Multi-Arc Plasma Torch With True Axial Powder Feed", Proceedings of the 1990 National Thermal Spray Conference, Long Beach, CA, ASM, (1991).
- [18] J. Finckel, W.D. Swank and D.C. Haggard, J.Thermal Spray Tech. 2(40) p.345, (1993).
- [19] E. Pfender, Surf. Coat. and Tech. 34(1), p. 1, (1988).
- [20] H. Herman, Scientific American , Vol.256 [9] p. 112, (Sept.1988).
- [21] M. Houben, Ph.D.Thesis, Eindhoven University of Technology, Eindhoven, Holland,

- (1988).
- [22] M. Moss, *Acta Met.*, 16, p. 321, (1968).
- [23] V. Wilms, Ph.D. Thesis, SUNY Stony Brook, (1978).
- [24] C. Moreau, P. Cielo, M. Lamontagne, S. Dallaire, J.C. Krapez and M. Vardelle, *Surf., and Coat. Tech.* 46, p. 173, (1991).
- [25] C. Moreau, P. Cielo, and M. Lamontagne, *J. Thermal Spray Tech.* 1(4), p. 317, (1992).
- [26] S. Sampath and H. Herman, "Microstructure Development in Plasma Sprayed Coatings", *Proceedings of International Thermal Spray Conference, Welding Inst., London Vol.1*, p. 53 (1989).
- [27] K.D. Krishnanand and R.W. Cahn, *Rapidly Quenched Metals*, Ed. N.J. Grant and B.C. Giessen, pp.67-75, MIT Press, Cambridge, 1976., 33. H. Herman and H. Bhat, *Synthesis and Properties of Metastable Phases*, Ed. E.S. Machlin and T.J., Rowland, TMS, AIME, Pittsburgh, PA., p.115-137, (1980).
- [28] S. Sampath and S.F. Wayne, "Microstructure and Properties of Plasma Sprayed Mo-Mo₂C Composites", *J. Thermal Spray Tech.* Vol.3, No.3 p. 282, (1994).
- [29] S. Sampath, R.A. Neiser, H. Herman, J.P. Kirkland and W.T. Elam, "A Structural Investigation of a Plasma Sprayed Ni-Cr based Alloy Coating", *J. Mater. Res.*, Vol.8, No.1, p. 78, (1993).

- [30] Safai and H. Herman, "Plasma Sprayed Material", Treatise Mtls. Sci. & tech., ed. H. Herman New York: Academic Press, p. 183-214, (1981).
- [31] S. Sampath, "Rapid Solidification During Plasma Spraying", Ph.D. thesis, State University of New York, Stony Brook, (1989).
- [32] A. R. E. Singer, "The principles of Spray Rolling of Metals", Metall. Mater., 4, p. 246-250, (1970).
- [33] G.J. Vogt, R.S. Vigil, L.R. Newkirk, and M. Trkula, Seventh International Symposium on Plasma Chemistry, Eindhoven, p.668, (1985).
- [34] T. Yoshida, H. Endo, H. Nishimura, and K. Akahi, Sixth International Symposium on Plasma Chemistry, Montreal, p. 225, (1983).
- [35] J. Canteloup and A. Mocellin, Special Ceramics 6, p.209, (1975).
- [36] T. Yoshida, A. Kawasaki, K. Nakagawa, and K. Akasi, J. Mater. Sci.,(14), p. 1624, (1979).
- [37] R.M. Salinger, Ind. Eng. Chem. Prod. Res. Develop., 11, p. 230, (1972).
- [38] P.C. Kong, M. Suzuki, R. Young, and E. Pfender, Plasma Chem. Plasma Process., p. 115, (1983).
- [39] T.I. Barry, R.K. Bayliss, and L.a. Lay, w. Mater. Sci., 3, p.229, (1968).
- [40] A.Audsley and R.K. Bayliss, J. Appl. Chem., 19, p.33, (1967).

- [41] J. Feinman, "Plasma Technology in Metallurgical Processing", Chapter 7, Iron & Steel Society, 1987.
- [42] M. Thorpe, Chemical Engineering, P. 54, November (1991).
- [43] P. Ronsheim, A. Mazza, and A.N. Christensen, "Thermal Plasma Synthesis of Transition Metal Nitrides and Alloys", Plasma Chemistry and Plasma Processing, Vol. 1, No. 2, p.135, (1981).
- [44] Y. Tsunekawa, M. Okumiya, K. Gotoh, T. Nakamura and I. Niimi, "Synthesis of Iron aluminide matrix in situ composites from elemental powders by reactive low pressure spraying", Materials Science and Engineering, A159, p. 253-259, (1992).
- [45] Y. Tsunekawa, K. Gotoh, M. Okumyla, and N. Mohrl, "High Temperature Stability of Titanium Aluminide Matrix Composites Fabricated by Reactive Low Pressure Plasma Spraying", Proceedings of the International Thermal Spray Conference & Exposition, Orlando, Florida, USA, p. 189-194. (28 May-5 June, 1992).
- [46] R. Castro, M.S. Thesis, Drexel University, Philadelphia, PA, USA, (1991).
- [47] Z.P. Lu, and E. Pfender, "Synthesis of AlN Powder in a Triple Torch Plasma Reactor", ISPC-9, Pugnochiuso, Italy, p. 675-680, Sept. 4-8, (1989).
- [48] M. Nagamori, "Computer Model for the $TiCl_4$ -Al Reaction", Final report, Noranda Technology Center, (1989).
- [49] R. D. Lewis, D. Webster, I. G. Palmer, "A Feasibility Study for Development of Structural Aluminum Alloys from Rapidly Solidified Powders for Aerospace

- Structural Applications," Technical Reports, AFML-TR-78-102, DARPA Order no. 3417. Lockheed Missiles & Space Company, Palo Alto, California, (1978).
- [50] H.G. Paris, F. R. Billman, W.S. Cebulak, and J.I. Petit, In Rapid Solidification Processing: Principles and Technologies II, R. Mehrabian, B.H. Kear, and M. Cohen, eds. Claitor's Baton Rouge, Louisiana, p. 331-341, (1980).
- [51] M. Bishop, and K.E. Fletcher, *Int. Met. Rev.*, 17, p. 230-225, (1972).
- [52] M. S. Zedalis and M. E. Fine, "Precipitation and Oswald Ripening in Dilute Al Base-Zr-V Alloy Metall. Trans. A, 17A pp. 2187-2198, (1986).
- [53] C. M. Adam, "Structure/Property Relationships and Applications of Rapidly Solidified Amorphous and Crystalline Alloys" ed. B. H. Kear et al. Elsevier Science Pub. Co., Amsterdam, Netherlands, p. 411-422 (1982).
- [54] S. K. Das, P.S. Gilman and D. Raybould, "Applications of Rapidly Solidified High Temperature Aluminum Alloys", *Key Engineering Materials*, Trans Tech Publications, Switzerland, Vols. 38 & 39 pp. 367-392, (1989).
- [55] L. A. Davis, "Advanced Aerospace Alloys via Rapid Solidification", *Key Eng. Mater*, Vol. 77-78, pp. 171-176, (1993).
- [56] D. H. St. John and L. M. Hogon, "Thermal Stability in the Al-Al₃Ti System, " *Journal of Materials Science*. 15, 2369, (1980).
- [57] S. Srinivasan, P.B. Desch and R.B. Schwarz, *Scr. Metall.*, 25, p. 2513 (1991).

- [58] J. H. Westbrook, Ed., "Intermetallic Compounds", NY: John Wiley and Sons, 307 (1938).
- [59] D. A. Granger, "Ingot Casting in the Aluminum Industry", Part 3, eds. A.K.Vasudevan, R. D. Doherty, "Aluminum Alloys-Contemporary Research and Applications, Treatise on Materials Science and Technology" Vol.31, p. 109-135, (1989).
- [60] I. G. Davies, J. M. Dennis, and A. Hellawell, Met. Trans, 1, 275-280, (1970).
- [61] G. Sigworth, Met. Trans, 15A, p. 227-282, (1984).
- [62] J. L. Murray, "Binary Alloys Phase Diagrams", Al-Ti, ASM International, p. 225-227. Second Edition, Vol. 1, (1990).
- [63] Heinz G. F. Wisdorf et al., "Very High Temperature Aluminum Materials Concepts," Biannual report No.2, AFWAL Contract No. F33615-86-C-5074, Light Metals Center, University of Virginia, (1987).
- [64] W.E. Frazier, "A Fundamental Study of the Mechanical and Microstructural Response of Elevated Temperature PM Aluminum-Titanium Alloys", Ph.D. thesis, Drexel University, (1987).
- [65] G.S. Murty, M. J. Kocczak, and W.E. Frazier, "High Temperature Deformation of Rapid Solidification Processed/Mechanically Alloyed Al-Ti Alloys", Scripta Met., 21, p.141, (1987).
- [66] D. H. St. John and L. M. Hogon, "Thermal Stability in the Al-Al₃Ti System, "Journal

- of Materials Science. 15, 2369, (1980).
- [67] L. F. Mondolfo, Aluminum alloys; Structure and Engineering Materials, NY: John Wiley, 14, (1976).
- [68] J. H. Westbrook, Ed., "Intermetallic Compounds", (NY, NY: John Wiley and Sons, 307 (1938).
- [69] P. Villars and L.D. Calvert, Pearson's Handbook of Crystallographic Data for Intermetallic Phases, 1076, Metals Park, OH: ASM, (1985).
- [70] J. Weber and D. Chellman, "Mechanically Alloyed Aluminum Alloys for Aircraft Applications", Presented at the ASM International Conference On Structural Applications of Mechanical Alloying, Myrtle Beach, SC, March 26-29, (1990).
- [71] P. K. Mirchandani, R. C. Benn, and K. A. Heck, "Structure-Property Relationships in Elevated Temperature High Stiffness Mechanically Alloyed Al-Ti Based alloys" light-Weight Alloys for Aerospace Applications Edited by E. W. Lee, E. H. Chia and N. J. Kim, The Minerals, Metals & Materials Society, p.33-58, (1989).
- [72] P. K. Mirchandani, R. C. Benn, and K. A. Heck, "Structure-property Relationships in Elevated Temperature High Stiffness Mechanically Alloyed Al-Ti Based Alloys", Light-Weight Alloys for Aerospace Applications, Edited by E. W. Lee, E. H. Chia and N. J. Kim, The Minerals, Metals & Materials Society, (1989).
- [73] W.E. Frazier and M.J. Koczak, "Mechanical and Thermal Stability of Powder Metallurgy Aluminum-Titanium Alloys", Scripta Met., 21, p. 129, (1987).

- [74] W.E. Frazier, "A Fundamental Study of the Mechanical and Microstructural Response of Elevated Temperature PM Aluminum-Titanium Alloys", (Ph.D. thesis, Drexel University, (1987).
- [75] W.E. Frazier and M.J. Koczak, "Grain Boundary and Orowan Strengthening of Elevated Temperature PM Aluminum-Titanium Alloys", Dispersion Strengthened Aluminum Alloys, Edited by Y.W. Kim and W. M. Griffith, The Minerals, Metals & Materials Society, p. 573-602, (1988).
- [76] R. E. Reed-Hill, in Physical Metallurgy Principles, Brooks/Cole, Monterey, CA, (1973).
- [77] Metals Handbook, vol. 2, "Properties of Non-Ferrous Metals", Tenth edition, (1992).
- [78] U.S. Bureau of Mines Report #5490.
- [79] M. Nagamori, "Computer Model for The $TiCl_4$ -Al Reaction", Noranda Inc, Project No. 88LN04, (1989).
- [80] G. E. P. Box, W. G. Hunter and J. S. Hunter, "Statistics for Experimenters an Introduction to Design, Data Analysis, and Model Building", John Wiley & Sons, Inc., (1978).
- [81] W. J. Huppman and K. Dalal, "Metallographic Atlas of Powder Metallurgy", Verlage Schmid GMBH, Freiburg, Germany, (1986).
- [82] G. Dowson, "Powder Metallurgy, the Process and its Products", Adam Hilger, New York, (1990).

- [83] J.J. Dunkley, "Producing Metal Powder", *Metals and Materials*, Vol. 6, No. 6, p. 361, (1990).
- [84] J.J. Dunkley, "Liquid Atomization", *Powder Metall.*, Vol. 32, No. 2, p.96, (1989).
- [85] A. Lawley, "Atomization, The Production of Metal Powders", *Metal Powder Industries Federation*, Princeton, New Jersey, (1992).
- [86] J.S. Thompson, *J. Inst. Met.* 74, 101 (1948).
- [87] J.F. Joyce, *Defence Metals Information Center Review*, Section in *Powder Metallurgy*, (1967).
- [88] P. Rao, "Shape and Other Properties of Gas Atomized Metal Powders", *Ph.D. Thesis*, department of Chemical Engineering, Drexel University, Philadelphia, PA, (1973).
- [89] S. Small and T.J. Bruce, *Int. J. Powder Metall.* 4, 7 (1968).
- [90] H. Lubanska, *J. Met.* 2, 45 (1970).
- [91] I. P. Goldaev, A. P. Montornenko, *Sov. Powder Metall. Met. Ceram.* 6, p. 433 (1967).
- [92] E. Klar and W.M. Shafer, *Powder Metallurgy for High Performance Applications*, Syracuse University Pres, p. 57-68, (1971).
- [93] L. Rayleigh, *Proc. London Math. Soc.* 10, 4 (1878-79).

- [94] N. Dombrowski and P.C. Hooper, *Chem. Eng. Sci.* **17**, 291 (1962).
- [95] J.K. Beddow, "The Production of Metal Powders by Atomization", Hayden & Son Ltd, Philadelphia (1978).
- [96] Yu. I. Naida, *Sov. Powder Metall. Met. Ceram.* **3**, p. 187, (1971).
- [97] A. F. Silaev, *Sov. Powder Metall. Met. Ceram.* **5**, p. 350, (1967).
- [98] B. N. Putimtsev, *Sov. Powder Metall. Met. Ceram.* **5**, p. 351, (1971).
- [99] J.O. Hinze, *AiChEJ.* **1**, p. 289, (1955).
- [100] O.S. Nichiporenko and Yu.I. Naida, "Heat Exchange Between Metal Particles and Gas in the Atomization Process", *Soviet Powder Metall. Ceramics*, Vol. 7, No. 67, P. 509, (1968).
- [101] J.B. See, and G.H. Johnson, "Interactions Between Nitrogen and Liquid Lead and Tin Streams, " *Powder Tech.*, Vol. 21, p. 119, (1978).
- [102] P. Rao and J.A. Tallmadge, "Change of Shape of Metal Droplets in Quench Atomization," *1971 Fall Powder Metallurgy Conference Proceedings*, Edited by S. Mocarski, Metal Powder Industries Federation, New York, NY, p. 251, (1972).
- [103] K.A. Kowalsky, D.R. Marantz, R.A. Neiser, and M.F. Smith, *Proceedings of the international Thermal Spray Conference*, C.C. Berndt, ed., Orlando, FL, p. 337 May 28-June 5, (1992).

- [104] B.P. Bewlay, and B. Cantor, *Met. Trans.* 21B, p. 899, (1990).
- [105] B.P. Bewlay, and B. Cantor, *Met. Trans.* 21B, p. 899, (1990).
- [106] M. Pilch and C.A. Erdman, *Int.J. Multiphase Flow*, 13, p. 741, (1987).
- [107] T. Iida and R.I.L. Guthrie, "The Physical Properties of Liquid Metals", Clarendon Press, Oxford, (1988).
- [108] *An Introduction to Transport Phenomena in Materials Engineering*, David R. Gaskell, Macmillian Publishing Company, (1992).
- [109] *Handbook of Chemistry and Physics*, D. R. Lide, 77th Edition, CRC Press Inc.,
- [110] *Powder Metallurgy Science*, R.M. German, Metal Powder Industries Federation, Princeton, New Jersey, U.S.A, (1984).
- [111] M. Entezarian, F. Allaire, P. Tsantrizos, and R.A.L. Drew, "Plasma Atomization:A
- [112] C. Suryanarayana, *Material Science and Technology*, ed. R.W. Cahn, P. Haasen, and E.J. Kramer, New York, VCH Publishers Inc., (1991).
- [113] T. F. Broderick, *et al.*, *The Effect of Cooling Conditions on the Microstructure of Rapidly Solidified Ti-6Al-4V*, *Met. Trans.* 16A p. 1951, (1985).
- [114] M.M. Guzowski, D.A. Sentner, and G.K. Sigworth, "Aluminum Grain Refiner Containing Duplex Crystals," UK Patent Application 2162540 A, (1985).

- [115] M. Yamaguchi, "High Temperature Intermetallics-With Particular Emphasis on TiAl", *Materials Science and Technology*, 8, p. 299-307, April (1992).
- [116] J. Mackowiak and L.L. Shreir, "The Nature and Growth of Interaction Layers Formed during the Reaction between Solid Titanium and Liquid Aluminum," *Journal of Less-Common Metals*, Vol. 1, p. 456, (1959).
- [117] J. Mackowiak and L.L. Shreir, "Kinetics of the Interaction of Ti with Al", *J. Less-Common Metals*, 15, (1968).
- [118] F. R. Sale, "Novel Processing Techniques for Powder Production", *Mater. Production*, p. 281-287, May (1990).
- [119] P. G. Tsantrizos, Ph.D Thesis, McGill University, (1988).
- [120] P. G. Tsantrizos, L.T. Mavropoulos, M.I. Boulos, J. Jurewicz, and K. Chen, *ISPC-10 Conference Proceedings*, Paper 1.4-2, Bochum, (1991).
- [121] W. J. Kroll, *Trans Electrochem Soc*, 1940, 78, 35; 1959, 215, p. 546; *Trans AIME*, (1959).
- [122] M.A. Hunter and A Jones, *Trans Electrochem Soc*, 43, p. 215, (1923).
- [123] H.H. Kellogg, *Trans. AIME*, 188, p. 862, (1950).
- [124] M. Nagamori *et al*, *Metal. Review MMIJ*, 4, no. 1, p.8 and no. 2, p.34, (1987).
- [125] *Handbook of Chemistry and Physics*, D. R. Lide, 77th Edition, CRC Press Inc.,

(1996-1997).

- [126] E. Klar, and W.M. Shafer, "High Pressure Atomization of Metals, in Powder Metallurgy for High-Performance Applications, Bruke, J.J. and Weiss, V., Ed., Syracuse University Press. P. 57-68, (1972).
- [127] C. Moreau and P. Gougeon, M. Lamontagne, V. Lacasse, G. Vaudreuil, and P. Cielo, "Thermal Spray Industrial Applications", Proc. Nat. Thermal Spray Conf., Boston, ASM International, Materials Park, OH, P. 431, (1994).
- [128] G.A Rozak, J.J. Lewandowski, J.F. Wallace, and A. Altmisoglu, "Effects of Casting Conditions and Deformation Processing on A356 Aluminum and A356-20 Vol. % SiC Composites", Journal of Composite Materials, Vol. 26, No. 14, P. 2076, (1992).
- [129] S. Zhang, J. P. Nic, W. W. Milligan, and D. E. Mikkola, "Temperature Dependence of the Compressive Strength of Cubic Phases Formed by Alloying Al_3Ti with Mn and Cr", Scripta Metallurgica et Materialia, Vol. 24, pp. 1441-1446, (1990).
- [130] D.A. Porter and K.E. Easterling, "Phase transformation in Metals and Alloys", Chapman & Hall, London, New York, (1992).
- [131] H. Jones, "Aluminum", 54, p. 274, (1978).
- [132] C. Suryanarayana, "Material Science and Technology", ed. R.W. Cahn, P. Haasen, and E.J. Kramer, New York, VCH Publishers Inc., (1991).
- [133] Metals Handbook, Vol 2, Tenth Edition, American Society for Materials International, (1992).

- [134] P. Tsantrizos, "The REFORM Synthesis of Ti Products", Final Report, NORANDA Technology, September (1991).
- [135] P.J. Andersen, P.C. Eloff, "Development of Higher Performance Blended Elemental Powder Metallurgy Ti Alloys", Powder Metallurgy of Titanium Alloys, Eds. F.H. Froes and J.E. Smugeresky, The Metallurgical Society of AIME, Warrendale, Pa. U.S.A. p. 175, (1980).

APPENDIX 1

```
100 PRINT "TSANT6 SIMULATION OF TiCl4-AL REACTIONS          1994-06-22"
101 PRINT "INITIAL G.ATOM OF ALUMINIUM: ";
102 INPUT NOAL
103 PRINT "TOTAL PRESSURE (ATM): ";
104 INPUT P
105 PRINT "MOLE OF INPUT ARGON GAS: ";
106 INPUT NAR
107 PRINT "TEMPERATURE IN KELVIN: ";
108 INPUT T
190 PRINT "      THREE STEPS FOR INITIAL GUESS : 4th(NR) is the final results."
200 PRINT " "
210 PRINT "N0TiCl4 = 1 MOLE (FIXED) : N0AL="; NOAL; "MOLES  : N0AR="; NAR;
"MOLES"
220 PRINT "TEMPERATURE(K)="; T; " : PRESSURE(ATM)="; P
230 PRINT " "
240 PRINT "APPROX.  NTi  NAl X=TiCl2 Z=TiCl3 V=AlCl Y=AlCl2 iter."
250 PRECIS = .001
260 R = 1.986: RT = R * T
270 K1 = EXP((74900! - 43.17 * T + 4.57 * T * LOG(T) / LOG(10)) / -RT)
280 K2 = EXP((106090! - 40.52 * T + 3.02 * T * LOG(T) / LOG(10)) / -RT)
290 K3 = EXP((-12930 - 35.95 * T + 5.9 * T * LOG(T) / LOG(10)) / -RT)
300 K4 = EXP((-80730! - 2.27 * T) / -RT)
310 K5 = EXP((-140400! + 7.05 * T + 2.5 * T * LOG(T) / LOG(10)) / -RT)
320 K6 = EXP((30840 - 20.84 * T) / -RT)
330 K7 = EXP((-73400! - 1.54 * T) / -RT)
340 K8 = EXP((-132400! + 13.36 * T) / -RT)
```

```
350 K9 = EXP((-184200! + 36.45 * T - 1.8 * T * LOG(T) / LOG(10)) / -RT)
360 K10 = EXP((58200! - 25.63 * T) / -RT)
370 K11 = EXP((-7330 - .73 * T) / -RT): K12 = EXP((44600! - 31.34 * T) / -RT)
380 K13 = EXP((54870! - 69.63 * T + 11.8 * T * LOG(T) / LOG(10)) / -RT)
390 Y0AL = EXP(-27084 / RT)
400 I = 1: DIV1 = .01
410 XAL = DIV1 * I: XTI = 1 - XAL
420 YAL = EXP(2 * XAL * XTI ^ 2 * -47916! / RT + (1 - 2 * XAL) * XTI ^ 2 * -27084 / RT)
430 YTI = EXP(2 * XTI * XAL ^ 2 * -27084 / RT + (1 - 2 * XTI) * XAL ^ 2 * -47916! / RT)
440 ALF = -47916! / RT: BET = -27083 / RT
450 A = K11 * YAL - YTI: B = K11 * YAL * (N0AL - 2) + 3 * YTI: C = -2 * YTI
460 DISCRI = B * B - 4 * A * C
470 X = (-B + SQR(DISCRI)) / 2 / A
480 NTI = 1 - X: NAL = N0AL - 2 + X: Y = 2 - X: NT = NAR + X + Y
490 X1AL = NAL / (NAL + NTI): X1TI = 1 - X1AL: ACTTI = YTI * X1TI: ACTAL = YAL * X1AL
500 DIFXAL = XAL - X1AL
510 IF (I < 1.5) THEN GOTO 520 ELSE GOTO 530
520 DIFOLD = DIFXAL
530 RATDIF = DIFXAL / DIFOLD
540 IF (RATDIF > 0) THEN GOTO 550 ELSE GOTO 560
550 I = I + 1: GOTO 410
560 V = 0: Z = 0
570 XAL = XAL - DIV1: XTI = 1 - XAL
580 YAL = EXP(2 * XAL * XTI ^ 2 * -47916! / RT + (1 - 2 * XAL) * XTI ^ 2 * -27084 / RT)
590 YTI = EXP(2 * XTI * XAL ^ 2 * -27084 / RT + (1 - 2 * XTI) * XAL ^ 2 * -47916! /
```

```
RT)
600 A = K11 * YAL - YTI: B = K11 * YAL * (N0AL - 2) + 3 * YTI: C = -2 * YTI
610 DISCRI = B * B - 4 * A * C
620 X = (-B + SQR(DISCRI)) / 2 / A
630 NTI = 1 - X: NAL = N0AL - 2 + X: Y = 2 - X: NT = NAR + X + Y
640 NALLOY = NTI + NAL
650 PRINT "1st  "; USING "###.####"; NTI; NAL; X; Z; V; Y
660 DIV2 = .02: VBEGIN = 0!: II = 1: Z = 0
670 V = DIV2 * II + VBEGIN: NT = NAR + 2 + .5 * V: Q1 = K13 * YAL * NT
680 Q2 = K13 * YAL * NT * (N0AL - V): Q3 = ((N0AL - V) * K13 * YAL * NT) ^ 2
690 Q4 = 4 * K13 * YAL * NT * P * V * V * (N0AL - 1 - .5 * V): Q5 = 2 * Q1
700 Q3Q4 = Q3 - Q4
710 IF (Q3Q4 < 0) THEN Q3Q4 = 0
720 DISCR2 = SQR(Q3Q4): Y1 = (Q2 + DISCR2) / Q5: Y2 = (Q2 - DISCR2) / Q5
730 X1 = 2 - .5 * V - Y1: NAL1 = N0AL - V - Y1: NTI1 = -1 + .5 * V + Y1
740 F1A = K11 * YAL * X1 * NAL1 - YTI * Y1 * NTI1
750 F1B = K11 * YAL * X2 * NAL2 - YTI * Y2 * NTI2
760 IF (II < 1.5) THEN GOTO 770 ELSE GOTO 780
770 F1AOLD = F1A
780 RATF1A = F1A / F1AOLD
790 IF (RATF1A > 0) THEN GOTO 800 ELSE GOTO 810
800 II = II + 1: GOTO 670
810 X = X1: Y = Y1: NAL = NAL1: NTI = NTI1
820 XAL = NAL1 / (NAL1 + NTI1): XTI = 1 - XAL
830 YAL = EXP(2 * XAL * XTI ^ 2 * -47916! / RT + (1 - 2 * XAL) * XTI ^ 2 * -27084
/ RT)
840 YTI = EXP(2 * XTI * XAL ^ 2 * -27084 / RT + (1 - 2 * XTI) * XAL ^ 2 * -47916! /
RT)
850 PRINT "2nd  "; USING "###.####"; NTI; NAL; X1; Z; V; Y1
```

```
860 X = X1: Y = Y1: NAL = NAL1: NTI = NTI1: NT = NAR + 2 + .5 * V: NALLOY =
NAL + NTI
870 DDD = 0
880 DDD = DDD + 1
890 DPDV = (NAL * (NAL - 2 * NALLOY) / NALLOY ^ 2) * (2 * (BET - ALF) * NTI /
NALLOY + ALF) + NAL ^ 2 * (BET - ALF) * (NTI + NALLOY) / NALLOY ^ 4
900 DPDY = (-2 * NAL / NALLOY ^ 2) * (2 * (BET - ALF) * NTI / NALLOY + ALF) +
2 * (BET - ALF) * NAL ^ 2 / NALLOY ^ 3
910 DQDV = (NTI * (NTI + NALLOY) / NALLOY ^ 3) * (2 * (ALF - BET) * NAL /
NALLOY + BET) + NTI ^ 2 * (ALF - BET) * (NAL - 2 * NALLOY) / NALLOY ^ 4
920 DQDY = (2 * NTI / NALLOY ^ 2) * (2 * (ALF - BET) * NAL / NALLOY + BET) -
2 * NTI ^ 2 * (ALF - BET) / NALLOY ^ 3
930 F1 = K11 * YAL * X * NAL - YTI * Y * NTI
940 F2 = K13 * YAL * Y * NAL * NT - P * V * V * NALLOY
950 A1 = K11 * YAL * (DQDV * X * NAL - .5 * NAL - X) - YTI * Y * (.5 + DPDV *
NTI)
960 B1 = K11 * YAL * (DQDY * X * NAL - NAL - X) - YTI * (DPDY * Y * NTI + NTI
+ Y)
970 A2 = K13 * YAL * (DQDV * Y * NAL * NT - Y * NT + .5 * Y * NAL) - P * V * (2
* NALLOY - .5 * V)
980 B2 = K13 * YAL * (DQDY * Y * NAL * NT + NAL * NT - Y * NT)
990 E1 = A1 * V + B1 * Y - F1: E2 = A2 * V + B2 * Y - F2
1000 D = A1 * B2 - A2 * B1
1010 VB = (E1 * B2 - B1 * E2) / D: YB = (A1 * E2 - A2 * E1) / D
1020 IF (DDD < 13) THEN GOTO 1030 ELSE GOTO 1140
1030 DDIF = ABS((ABS(V) - ABS(VB)) / ABS(VB))
1040 IF (DDIF < PRECIS) THEN GOTO 1130 ELSE GOTO 1050
1050 V = VB: Y = YB: X = 2 - .5 * V - Y: NTI = -1 + .5 * V + Y: NAL = N0AL - V - Y
1060 IF (X < 0) THEN X = .01
```

```
1070 IF (NTI > 1) THEN NTI = .8
1080 NALLOY = NTI + NAL: NT = NAR + 2 + .5 * V
1090 XTI = NTI / (NTI + NAL): XAL = 1 - XTI
1100 YAL = EXP(2 * XAL * XTI ^ 2 * -47916! / RT + (1 - 2 * XAL) * XTI ^ 2 * -27084
/ RT)
1110 YTI = EXP(2 * XTI * XAL ^ 2 * -27084 / RT + (1 - 2 * XTI) * XAL ^ 2 * -47916!
/ RT)
1120 GOTO 880
1130 PPP = LLK: GOTO 1150
1140 PRINT "LOOP LIMIT FOR 2ND APPROX, DDD="; DDD
1150 V = VB: Y = YB: X = 2 - .5 * V - Y: NTI = -1 + .5 * V + Y: NAL = N0AL - V - Y:
NALLOY = N0AL - 1 - .5 * V
1160 NT = NAR + 2 + .5 * V
1170 XTI = NTI / (NTI + NAL): XAL = 1 - XTI
1180 YAL = EXP(2 * XAL * XTI ^ 2 * -47916! / RT + (1 - 2 * XAL) * XTI ^ 2 * -27084
/ RT)
1190 YTI = EXP(2 * XTI * XAL ^ 2 * -27084 / RT + (1 - 2 * XTI) * XAL ^ 2 * -47916!
/ RT)
1200 PRINT "3rd(NR) "; USING "###.####": NTI; NAL; X; Z; V; Y; DDD
1210 JKK = 0
1220 JKK = JKK + 1
1230 NPTI = -1 + V - X + 2 * Y: NAL = N0AL - V - Y: NPALLOY = 3 * N0AL - 1 - 2 *
V - X - Y
1240 NPT = 3 * NAR + 4 + 2 * V + X + Y: ZP = 4 - V - 2 * X - 2 * Y
1250 XAL = NAL / (NAL + NPTI / 3): XTI = 1 - XAL
1260 YAL = EXP(2 * XAL * XTI ^ 2 * -47916! / RT + (1 - 2 * XAL) * XTI ^ 2 * -27084
/ RT)
1270 YTI = EXP(2 * XTI * XAL ^ 2 * -27084 / RT + (1 - 2 * XTI) * XAL ^ 2 * -47916!
/ RT)
```

1280 IF (ZP < .0001) THEN ZP = SQR(P * X * X * X / K12 / ACTTI / NPT)
 1290 F1 = 3 * K11 * YAL * X * NAL - YTI * Y * NPTI
 1300 F2 = K12 * YTI * ZP * ZP * NPTI * NPT - 27 * P * X * X * X * NPALLOY
 1310 F3 = K13 * YAL * Y * NAL * NPT - P * V * V * NPALLOY
 1320 BET0 = BET + 2 * (ALF - BET) * 3 * NAL / NPALLOY
 1330 ALF0 = ALF + 2 * (BET - ALF) * NPTI / NPALLOY
 1340 DQDV = 2 * NPTI * (NPALLOY + 2 * NPTI) * BET0 / NPALLOY ^ 3 + 6 * (ALF - BET) * NPTI * NPTI * (-NPALLOY + 2 * NAL) / NPALLOY ^ 4
 1350 DQDX = 2 * NPTI * (-NPALLOY + NPTI) * BET0 / NPALLOY ^ 3 + 6 * (ALF - BET) * NPTI * NPTI * NAL / NPALLOY ^ 4
 1360 DQDY = 2 * NPTI * (2 * NPALLOY + NPTI) * BET0 / NPALLOY ^ 3 + 6 * (ALF - BET) * NPTI * NPTI * (-NPALLOY + NAL) / NPALLOY ^ 4
 1370 DPDV = 18 * NAL * (-NPALLOY + 2 * NAL) * ALF0 / NPALLOY ^ 3 + 18 * NAL * NAL * (BET - ALF) * (NPALLOY + 2 * NPTI) / NPALLOY ^ 4
 1380 DPDX = 18 * NAL * NAL * NAL * ALF0 / NPALLOY ^ 3 + 18 * NAL * NAL * (BET - ALF) * (-NPALLOY + NPTI) / NPALLOY ^ 4
 1390 DPDY = 18 * NAL * (-NPALLOY + NAL) * ALF0 / NPALLOY ^ 3 + 18 * NAL * NAL * (BET - ALF) * (2 * NPALLOY + NPTI) / NPALLOY ^ 4
 1400 A1 = 3 * K11 * (YAL * DQDV * X * NAL - YAL * X) - Y * (YTI * DPDV * NPTI + YTI)
 1410 B1 = 3 * K11 * NAL * (YAL * DQDX * X + YAL) - Y * (YTI * DPDX * NPTI - YTI)
 1420 C1 = 3 * K11 * X * (YAL * DQDY * NAL - YAL) - YTI * DPDY * Y * NPTI - YTI * NPTI - 2 * YTI * Y
 1430 A2 = K12 * YTI * (DPDV * ZP * ZP * NPTI * NPT - 2 * ZP * NPTI * NPT + ZP * ZP * NPT + 2 * ZP * ZP * NPTI) + 2 * 27 * P * X * X * X
 1440 B2 = K12 * YTI * (DPDX * ZP * ZP * NPTI * NPT - 4 * ZP * NPTI * NPT - ZP * ZP * NPT + ZP * ZP * NPTI) - 3 * 27 * P * X * X * NPALLOY + 27 * P * X * X * X
 1450 C2 = K12 * YTI * (DPDY * ZP * ZP * NPTI * NPT - 4 * ZP * NPTI * NPT + 2 * ZP

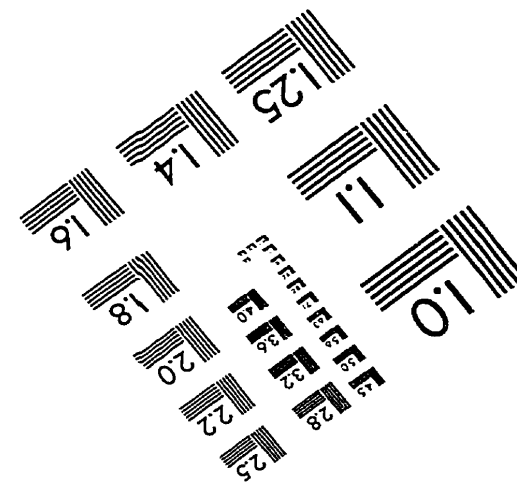
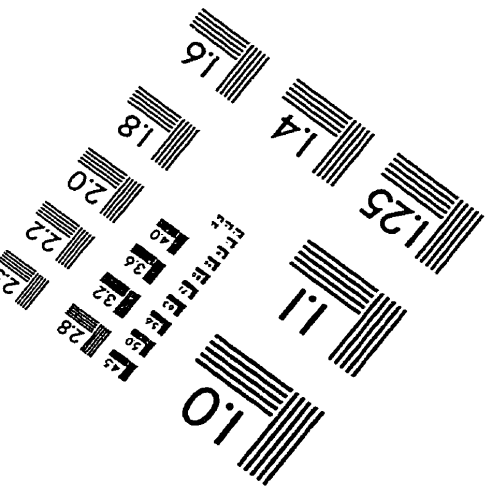
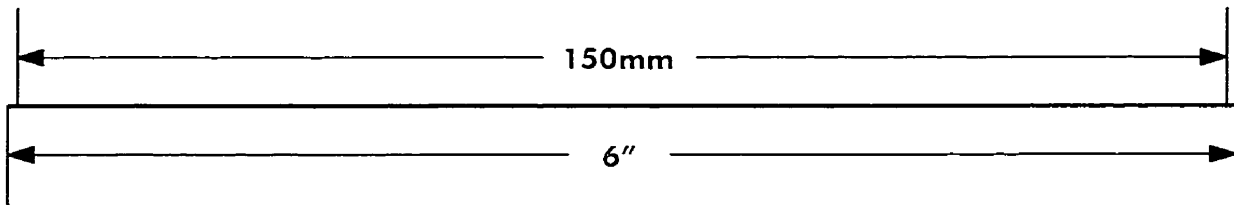
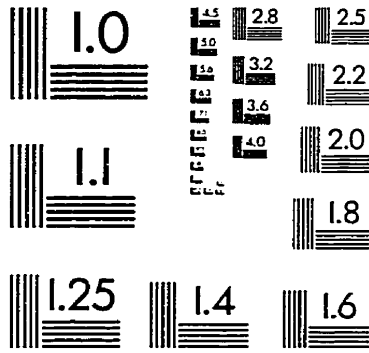
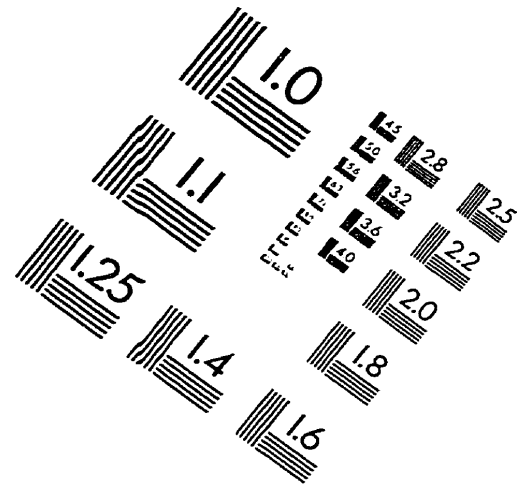
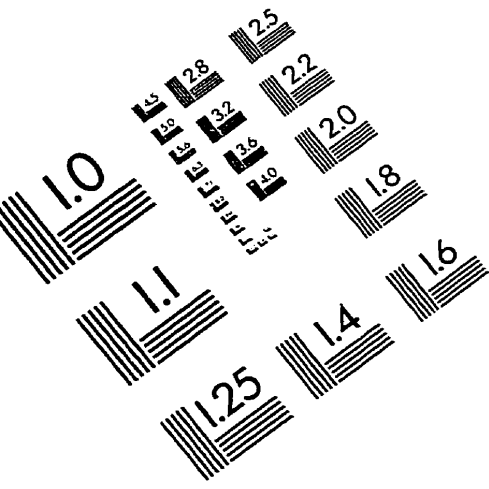
```

* ZP * NPT + ZP * ZP * NPTI) + 27 * P * X * X * X
1460 A3 = K13 * YAL * Y * (DQDV * NAL * NPT - NPT + 2 * NAL) - 2 * P * V *
NPALLOY + 2 * P * V * V
1470 B3 = K13 * Y * NAL * YAL * (DQDX * NPT + 1) + P * V * V
1480 C3 = K13 * YAL * (DQDY * Y * NAL * NPT + NAL * NPT - Y * NPT + Y * NAL)
+ P * V * V
1490 E1 = A1 * V + B1 * X + C1 * Y - F1
1500 E2 = A2 * V + B2 * X + C2 * Y - F2
1510 E3 = A3 * V + B3 * X + C3 * Y - F3
1520 D = A1 * B2 * C3 + A3 * B1 * C2 + A2 * B3 * C1 - A3 * B2 * C1 - A1 * B3 * C2 -
A2 * B1 * C3
1530 VB = (E1 * B2 * C3 + E3 * B1 * C2 + E2 * B3 * C1 - E3 * B2 * C1 - E1 * B3 * C2
- E2 * B1 * C3) / D
1540 XB = (A1 * E2 * C3 + A3 * E1 * C2 + A2 * E3 * C1 - A3 * E2 * C1 - A1 * E3 * C2
- A2 * E1 * C3) / D
1550 YB = (A1 * B2 * E3 + A3 * B1 * E2 + A2 * B3 * E1 - A3 * B2 * E1 - A1 * B3 * E2
- A2 * B1 * E3) / D
1560 IF (JKK < 10) THEN GOTO 1570 ELSE GOTO 1800
1570 DIF = ABS((ABS(X) - ABS(XB)) / ABS(XB))
1580 IF (DIF < PRECIS) THEN GOTO 1600 ELSE GOTO 1590
1590 V = VB: X = XB: Y = YB: GOTO 1220
1600 V = VB: X = XB: Y = YB
1610 NAL = N0AL - V - Y: NTI = (-1 + V - X + 2 * Y) / 3: NALLOY = (3 * N0AL - 1 +
V - X + 2 * Y) / 3
1620 NT = (3 * NAR + 4 + 2 * V + X + Y) / 3: Z = (4 - V - 2 * X - 2 * Y) / 3
1630 PRINT "4th(NR) "; USING "###.#####"; NTI; NAL; X; Z; V; Y; JKK
1640 GRAMTI = NTI * 47.9: GRAMAL = 26.98 * NAL: WPTI = 100 * GRAMTI /
(GRAMTI + GRAMAL)
1650 RECTI = 100 * NTI

```

```
1660 ACTTI = YTI * XTI: ACTAL = YAL * XAL
1670 PAL = P * K1 * ACTAL: PTI = P * K2 * ACTTI
1680 PTICL2 = P * X / NT: PTICL3 = P * Z / NT: PALCL = P * V / NT: PALCL2 = P *
Y / NT: PAR = P * NAR / NT
1690 PCL2 = PALCL2 / ACTAL / K4: PCL = SQR(K10 * PCL2)
1700 PALCL3 = P * K5 * ACTAL * PCL2 ^ 1.5
1710 PTICL = P * K6 * ACTTI * PCL2 ^ .5: PTICL4 = P * K9 * ACTTI * PCL2 ^ 2
1720 PRINT "PRES.ATM": USING "####.#####"; PTI; PAL; PTICL2; PTICL3; PALCL;
PALCL2
1730 PRINT " "
1740 PRINT "PRES.ATM  TiCl ="; PTICL; "  TiCl4="; PTICL4
1750 PRINT "PRES.ATM  AlCl3="; PALCL3; "  Argon="; PAR
1755 PRINT "PRES.ATM  Cl  ="; PCL; "  Cl2  ="; PCL2
1760 PRINT " "
1770 PRINT "Weight % Ti in Alloy ="; WTPTI; " : Ti Recovery ="; RECTI; "(%)"
1780 PRINT " "
1790 GOTO 1810
1800 PRINT "END OF LOOP DUE TO MAX JKK="; JKK
1810 END
```

IMAGE EVALUATION TEST TARGET (QA-3)



APPLIED IMAGE, Inc
1653 East Main Street
Rochester, NY 14609 USA
Phone: 716/482-0300
Fax: 716/288-5989

© 1993, Applied Image, Inc., All Rights Reserved